

DEVELOPMENT OF SIGNAL PROCESSING TECHNIQUES FOR ENHANCEMENT OF ENERGY CONCENTRATION IN TIME-FREQUENCY REPRESENTATION OF S-TRANSFORM

Ph.D. THESIS

by

NEHA SINGH



**DEPARTMENT OF ELECTRONICS AND COMMUNICATION ENGINEERING
INDIAN INSTITUTE OF TECHNOLOGY ROORKEE
ROORKEE, INDIA (247667)
SEPTEMBER, 2019**

DEVELOPMENT OF SIGNAL PROCESSING TECHNIQUES FOR ENHANCEMENT OF ENERGY CONCENTRATION IN TIME-FREQUENCY REPRESENTATION OF S-TRANSFORM

A THESIS

*Submitted in partial fulfilment of the
requirements for the award of the degree*

of

DOCTOR OF PHILOSOPHY

in

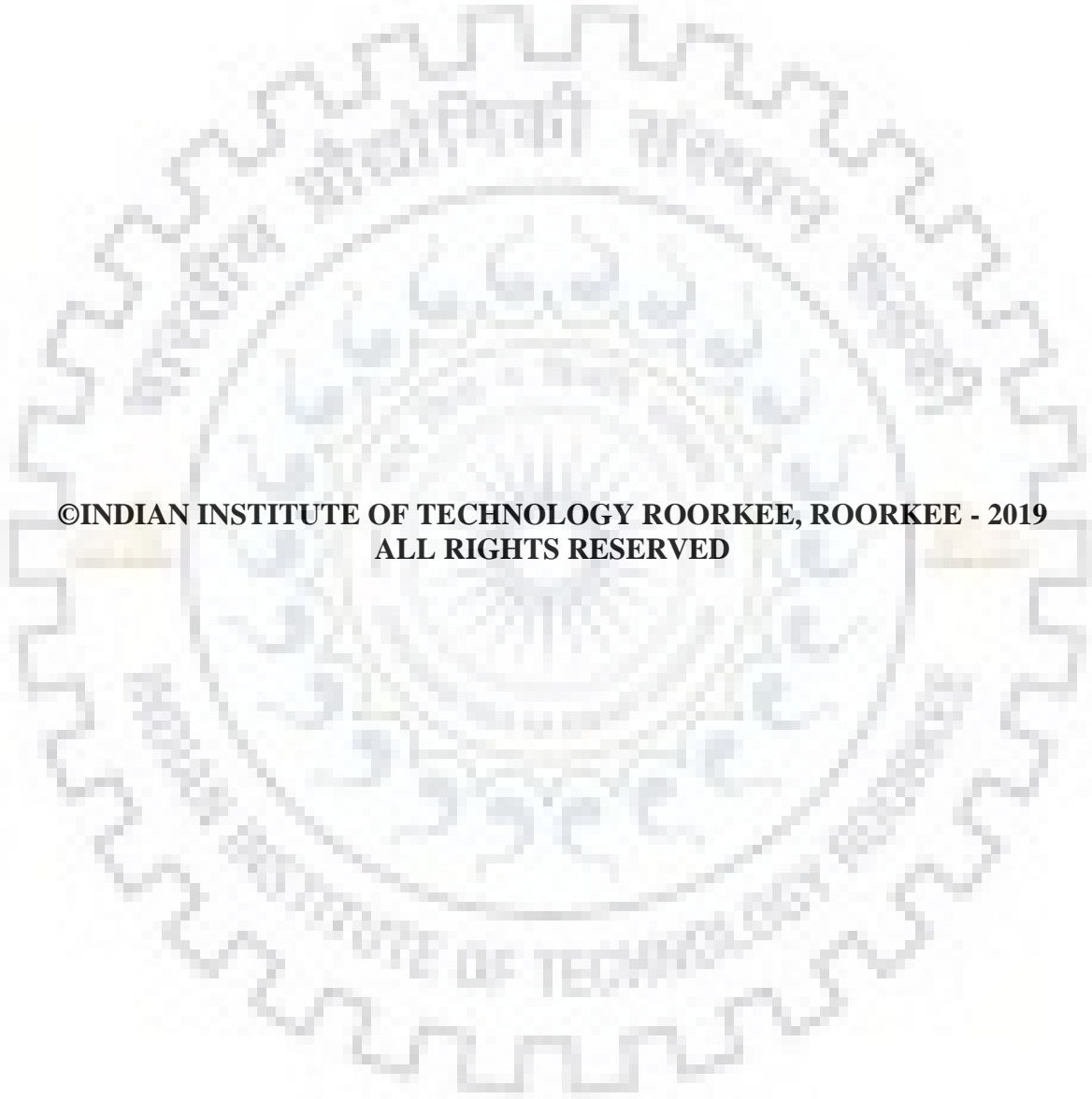
ELECTRONICS & COMMUNICATION ENGINEERING

by

NEHA SINGH



**DEPARTMENT OF ELECTRONICS AND COMMUNICATION ENGINEERING
INDIAN INSTITUTE OF TECHNOLOGY ROORKEE
ROORKEE, INDIA (247667)
SEPTEMBER, 2019**



**©INDIAN INSTITUTE OF TECHNOLOGY ROORKEE, ROORKEE - 2019
ALL RIGHTS RESERVED**



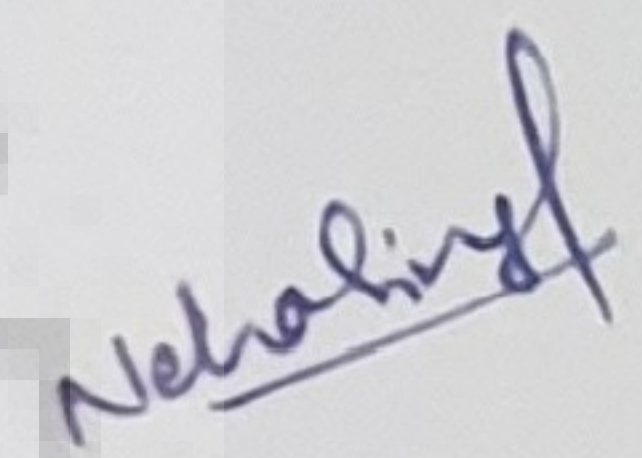
INDIAN INSTITUTE OF TECHNOLOGY ROORKEE ROORKEE

STUDENT'S DECLARATION

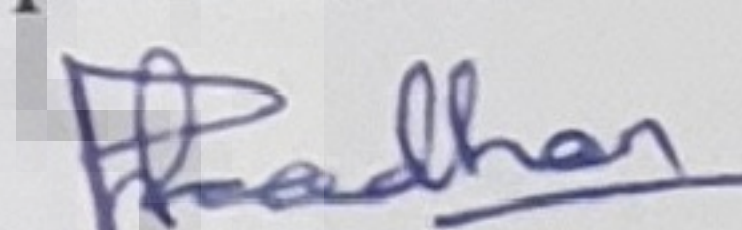
I hereby certify that the work presented in the thesis entitled “**DEVELOPMENT OF SIGNAL PROCESSING TECHNIQUES FOR ENHANCEMENT OF ENERGY CONCENTRATION IN TIME-FREQUENCY REPRESENTATION OF S-TRANSFORM**” is my own work carried out during a period from December, 2014 to September, 2019 under the supervision of Dr. P. M. Pradhan, Assistant Professor, Department of Electronics and Communication Engineering, Indian Institute of Technology Roorkee, Roorkee, India.

The matter presented in the thesis has not been submitted for the award of any other degree of this or any other Institute.

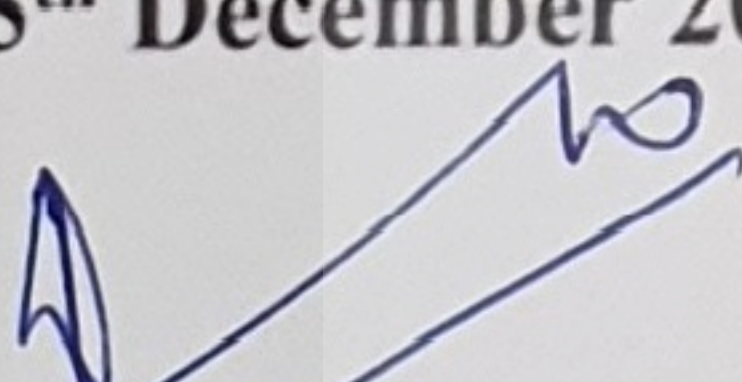
Dated: 5th September 2019

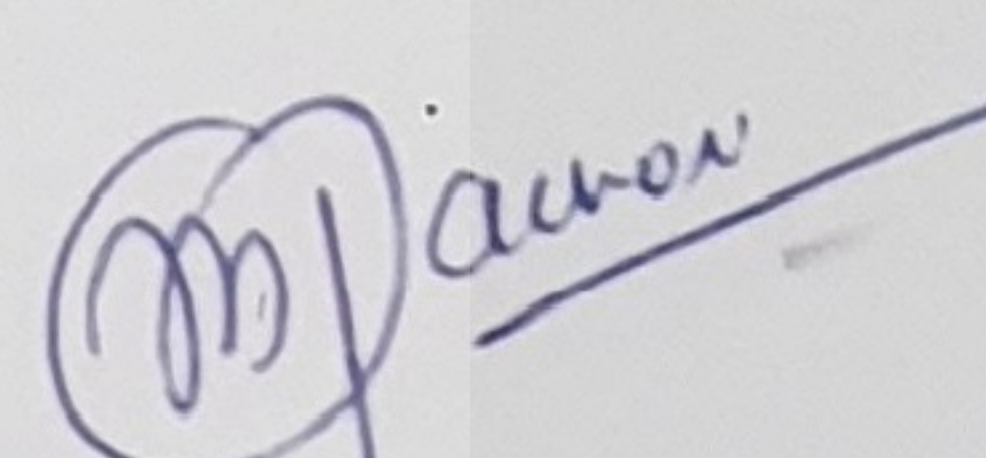

(Neha Singh)

This is to certify that the above mentioned work is carried out under my supervision.

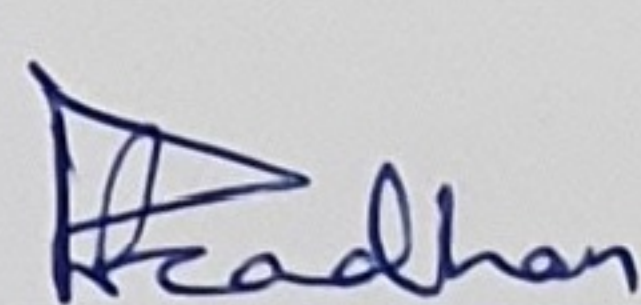

(P. M. Pradhan)
Supervisor

The Ph. D. Viva-Voce Examination of **NEHA SINGH**, Research Scholar, has been held on 5th December 2019

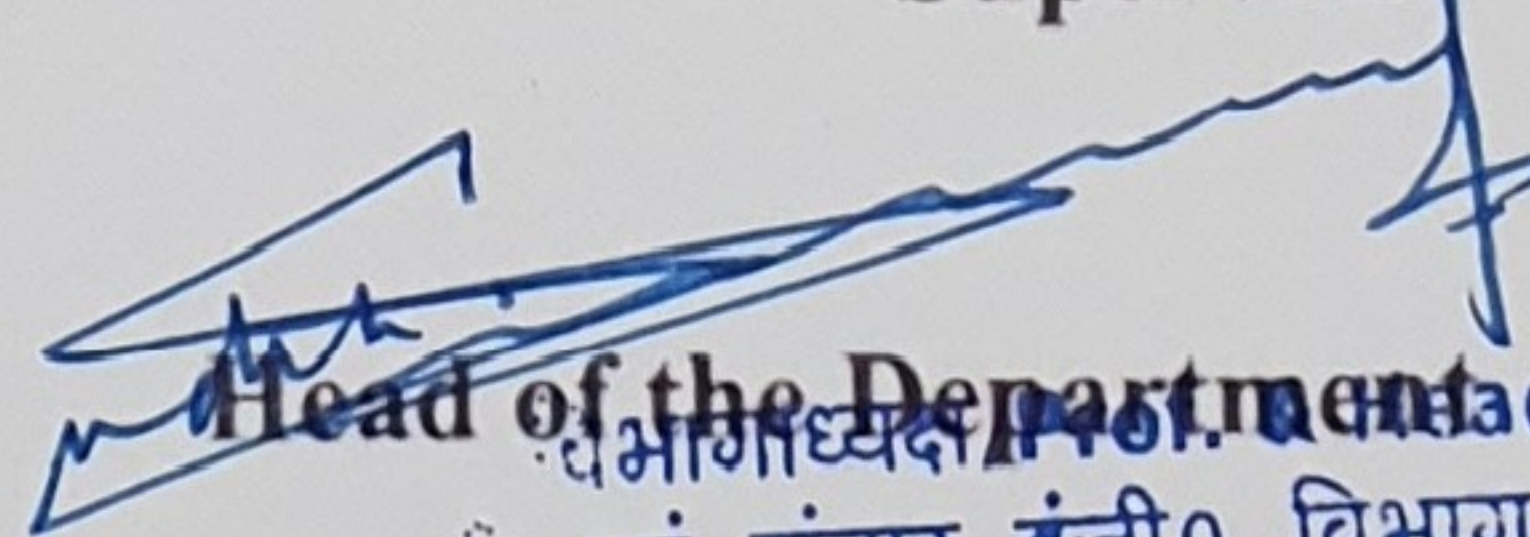

Chairman, SRC


External Examiner

This is to certify that the student has made all the corrections in the thesis.


(P. M. Pradhan)
Supervisor

Dated: 5th December 2019


Head of the Department
विभाग अध्यक्ष, एल. ई. ई. विभाग
Electronics & Communication Engg.
प्रौद्योगिकी संस्थान, रुड़की
Indian Institute of Technology, Roorkee



*To
my beloved parents and husband Vikash,
my dearest friend Ravinder,
and my respected Ph.D supervisor*



ACKNOWLEDGEMENTS

First and foremost, I would like to thank Almighty for giving me strength and opportunity to carry out this research and complete it satisfactorily.

I would like to express my sincere gratitude to my advisor **Dr. P. M. Pradhan** for the continuous support in my Ph.D study and related research, and for his patience and motivation. His guidance helped me all the time, not only in research and writing manuscripts and thesis, but also in leading a better life. I could not have imagined having a better advisor and mentor for my Ph.D study.

Besides my advisor, I would like to earnestly thank the rest of my research committee: **Prof. D. Singh, Prof. D. Ghosh** and **Prof. R. Balasubramanian**, for their insightful comments and encouragement.

My sincere thanks also goes to **Dr. M. Rawat** and **Dr. V. Pankajakshan** for their lectures and discussion on Digital Signal Processing and Adaptive Signal Processing which helped me a lot to understand these fields.

I would like to give my deepest gratitude to my friend **Dr. R. K. Randhawa** for his all time support, insightful comments and constructive suggestions in technical discussions related to Ph.D work. His intellect, and zeal and zest towards research work inspired me a lot during my entire Ph.D study. I will never forget the 5 A.M. yoga classes (thanks to Randhawa), and the never ending discussions on Swami Vivekananda's work in soothing campus of IITR, which I will cherish for a lifetime.

I would like to thank my friends and labmates **Dr. Sasmita, Dr. Shitala, Sonal, Girish, Anchal, Dr. Anjali, Priyanka, Akashay, Akanksha, Sainul, Dr. Manoranjan, Shekhar, Priya, Radhika, Sunil, Chothmal, Navneet** and **Mallika** for making these five years memorable and easy.

I would also like to thank **Gopinath, Puneesh Devora, Dr. P. Sumathi** and **Neha Kumari** for their valuable support during different stages of my research work.

Last but not the least, I would like to thank my father **Mr. A. B. Singh** for shaping my career towards higher studies and being an helping hand throughout my life. I would like to thank my mother **Mrs. Shakuntala Singh** for supporting me emotionally, spiritually throughout writing this thesis and my life in general. I would like to give my sincere thanks to my husband **Mr. Vikash Singh** for all his efforts and encouragements which gave me mental strength during my entire Ph.D work. I would also like to thank my brothers **Sudheer** and **Sujeet**, and cousins **Mandhatya** and **Naina** who have always helped me in life.

(Neha Singh)



ABSTRACT

The motivation behind the time-frequency analysis (TFA) is rooted in classical Fourier analysis. In contrast to Fourier transform (FT), time-frequency transforms analyze signals in both time and frequency domain simultaneously and provide time-frequency representation (TFR). The conventional methods for TFA can be categorized into two groups. The first group includes linear time-frequency transforms which attempt to make FT time dependent. The second group includes quadratic TFA techniques. Short time Fourier transform (STFT), wavelet transform (WT) and S-transform (ST) are some well-known transforms listed under the first category whereas Wigner-Ville distribution and Cohen class of distribution are listed under the later.

ST is an advancement of the STFT and CWT. It has direct relationship with FT, and retains the absolutely referenced phase property of STFT. It provides frequency invariant amplitude response along with multi-resolution analysis. These properties of ST have led to its wide usage in various fields such as geophysics, power system engineering, biomedical engineering, biometric, etc. The conventional ST uses a Gaussian window whose width varies as inversely proportional to the frequency. The long taper of the Gaussian window and the scaling criterion provide very large window width for lower frequencies, and very short window width for higher frequencies, and hence leads to unnecessary deterioration in time and frequency resolution at lower and higher frequencies, respectively.

In the first objective of this dissertation, two variants of ST, namely time-limited ST (TST) and band-limited ST (BST) are proposed. TST and BST are based on optimally concentrated discrete time-limited and band-limited windows of finite length. The proposed TST has ability to precisely localize the signals in time domain while maximizing the energy concentration in frequency domain. The proposed BST has ability to precisely localize the signals in given band while maximizing the energy concentration in time domain.

The second objective focuses on maximally achievable trade-off between time and frequency domain energy concentrations for discrete time finite length sequences. The problem of simultaneous maximization of time and frequency domain energy concentrations is formulated as the maximization of weighted linear combination of desired concentration measures in time and frequency domains. A novel optimal window with finite support (OWFS) is proposed based on discrete time continuous frequency scenario. The proposed OWFS is extended to design an adaptive TFA method for reducing the instantaneous frequency (IF) estimation error in case of multi-component signals in noisy environment. For discrete time discrete frequency scenario, a novel optimally concentrated discrete window (OCDW) is proposed. OCDW is designed by solving a constraint

optimization problem of maximization of the product of time and frequency domain energy concentrations in given time and frequency intervals. Further, it is extended to design an OCDW based ST (OST) for multi-resolution analysis. A new scaling criterion is also proposed for OST which prevents unnecessary deterioration in frequency resolution at higher frequencies, and time resolution at lower frequencies.

In the third objective, an asymmetrical modified Kaiser window (AMKW) based ST is proposed for sharp detection of event's onset. The multi-resolution analysis and frequency dependent asymmetry are obtained by modifying the β parameter of first order Bessel function of Kaiser window. The proposed scheme leads to sharp detection of events in front direction while having minimum degradation in backward direction. This scheme also results in minimum degradation in frequency resolution as compared to other existing TFA techniques for event detection.

In the fourth objective of this dissertation, the reassignment method (RM) and synchrosqueezing transform (SST) are deployed on the TFR of OST, and further investigated for detecting multiple power quality disturbances. It is found that the OST combined with RM and SST provides better visualization as compared to other counterparts of ST. Further, a product-ST is proposed for better visualization by multiplying the TFRs of TST and BST. The concepts of RM and SST are incorporated in the product-ST, and the resulting TFR is found to provide better visualization and frequency detection accuracy as compared to its OST counterpart.

In this dissertation, different techniques are proposed to enhance the energy concentration in the ST. The performances of these techniques are demonstrated using synthetic and real world examples from power system engineering, biomedical engineering and geoscience.

Contents

Acknowledgements	i
Abstract	iii
List of Figures	ix
List of Tables	xv
List of Abbreviations	xvii
1 Introduction	1
1.1 Background and Motivation	1
1.2 Research Objectives	3
1.3 Organization of Thesis	6
2 Literature Survey	9
2.1 Fourier Transform	9
2.2 Motivation for Time-Frequency Analysis	9
2.3 Short Time Fourier Transform (STFT)	10
2.3.1 Limitation of STFT	11
2.4 Hilbert-Huang Transform (HHT)	13
2.4.1 Empirical Mode Decomposition	13
2.4.2 Hilbert Transform	14
2.4.3 Hilbert Spectrum	14
2.4.4 Limitations of HHT	15
2.4.5 Ensemble Empirical Mode Decomposition	15
2.5 Continuous Wavelet Transform (CWT)	16
2.5.1 Limitations of CWT	17
2.5.2 Empirical Wavelet Transform	17
2.6 Chirplet Transform	18
2.7 S-transform (ST)	20
2.7.1 Derivation of ST from STFT	20
2.7.2 Computation of ST in Frequency Domain	21
2.7.3 Discrete ST	21

2.7.4	Limitations of ST	22
2.8	Existing Scaling Criteria for ST	22
2.8.1	Conventional Linear Scaling	22
2.8.2	Modified Linear Scaling	23
2.8.3	Power Scaling	24
2.8.4	Sigmoid Scaling	25
2.9	Existing Windows for ST	26
2.9.1	Symmetrical Windows	26
2.9.2	Asymmetrical Windows	27
2.10	Existing Post Processing Tools for ST	28
2.10.1	ST combined with SST	29
2.10.2	ST combined with RM	30
2.11	Concluding Remarks	31
3	ST based on Optimally Concentrated Time-limited and Band-limited Windows	33
3.1	Introduction	33
3.2	Time-limited and Band-limited Windows	34
3.2.1	Problem Formulation for Time-limited Window	34
3.2.2	Problem Formulation for Band-limited Window	35
3.3	Properties of Time-limited and Band-limited Windows	37
3.3.1	Characteristics of Time-limited window	37
3.3.2	Characteristics of Band-limited Window	39
3.3.3	Relationship Between Time-limited and Band-limited Windows	40
3.4	Time-limited Window based ST (TST)	41
3.4.1	Comparison Between Time-limited Window and Truncated Gaussian Window	42
3.4.2	Selection of Frequency Dependent Time and Frequency Intervals in TST	44
3.5	Band-limited Window based ST (BST)	45
3.5.1	Selection of Frequency Dependent Time and Frequency Intervals in BST	45
3.6	Simulation Results and Discussion	45
3.7	Conclusion	55
4	Simultaneous Time and Frequency Domain Energy Concentration for Finite Length Sequences	57
4.1	Introduction	57

4.2	Problem Formulation and Analysis	61
4.3	Properties of Time Domain (α^2) and Frequency Domain (β^2) Energy Concentrations	63
4.3.1	Property 1	63
4.3.2	Property 2	64
4.4	Upper Bound of Achievable α^2 and β^2 for Finite Length Sequences	66
4.5	Performance Analysis	69
4.5.1	Comparison with Truncated DPSS	69
4.5.2	Comparison with Existing Well-known Windows	71
4.6	Extension of Proposed Work to Discrete Frequency Domain	72
4.7	Application of Optimally Concentrated Window with Finite Support in Time-Frequency Analysis	74
4.8	Proposed Optimally Concentrated Discrete Window (OCDW)	77
4.8.1	Proposed OCDW based ST (OST)	80
4.8.2	Proposed Fair Scaling Criterion for OST	80
4.9	Conclusion	85
5	Sharp Detection of Event's Onset with Asymmetrical Modified Kaiser Window based ST	87
5.1	Introduction	87
5.2	Proposed Asymmetrical Modified Kaiser Window based ST	88
5.3	Simulation Results	91
5.4	Conclusion	97
6	Reassignment of Energy in the TFRs of OST and Product-ST	99
6.1	Introduction	99
6.2	OST Combined with RM and SST	100
6.3	Proposed Product-ST	100
6.3.1	Product-ST Combined with SST	101
6.3.2	Product-ST Combined with RM	102
6.4	Simulation Results	103
6.4.1	Case Study 1: Detection of Multiple Power Quality Disturbances	103
6.4.2	Case Study 2: Analysis of San Fernando Earthquake Data	104
6.4.3	Case Study 3: Analysis of Northridge Earthquake Data	106
6.5	Conclusion	108

7 Conclusions and Future Scope	109
7.1 Conclusions	109
7.2 Future Scope	110
Appendix	113
Bibliography	117
List of Publications	133



List of Figures

2.1	(a) A increasing chirp signal; (b) A decreasing chirp signal; (c) Amplitude spectrum of increasing chirp signal shown in (a); (d) Amplitude spectrum of decreasing chirp signal shown in (b); (e) Phase spectrum of increasing chirp signal shown in (a); Phase spectrum of decreasing chirp signal shown in (b)	10
2.2	Amplitude spectrum of the STFT of non-stationary signal: (a) The width of the window is 0.1; (b) The width of the window is 0.05	11
2.3	Illustration of the limitation of the STFT: (a) Synthetic test time series; (b) Amplitude spectrum of the STFT. Test time series of 1000 samples consists of a low frequency signal of 50 Hz for the first half of its duration, a high frequency signal of 150 Hz for the second half of the duration, and a high frequency burst from samples 20 to 30	12
2.4	Hilbert spectrum for the test time series shown in Fig. 2.3(a)	15
2.5	Amplitude spectrum of CWT for the test time series shown in Fig. 2.3(a) .	16
2.6	Amplitude spectrum of CT for the test time series shown in Fig. 2.3(a) . .	19
2.7	(a) Test time series; Amplitude spectrum of (b) STFT; (c) CWT; (d) CT .	19
2.8	Amplitude spectrum of the ST of sinusoidal time series as shown in Fig. 2.3(a)	22
2.9	Comparison between CLS and MLS: SD of GW for length $N = 512$ in (a) Time domain; (b) Frequency domain	24
2.10	Comparison between CLS and PS: SD of GW for length $N = 512$ in (a) Time domain; (b) Frequency domain	25
2.11	Comparison between CLS and SS: SD of GW for length $N = 512$ in (a) Time domain; (b) Frequency domain	26
3.1	Time-limited windows for $N = 128$, $M = 16$ and different values of L : (a) Time-limited windows in time domain; (b) The frequency domain spectra of time-limited windows	37

3.2	Time-limited windows for $N = 128$, $L = 8$ and different values of M : (a) Time-limited windows in time domain; (b) The frequency domain spectra of time-limited windows	38
3.3	Band-limited windows for $N = 128$, $L = 8$ and different values of M : (a) Band-limited windows in time domain; (b) The frequency domain spectra of band-limited windows	39
3.4	Band-limited windows for $N = 128$, $M = 8$ and different values of L : (a) Band-limited windows in time domain; (b) The frequency domain spectra of band-limited windows	40
3.5	Comparison of proposed time-limited (dashed lines) and truncated Gaussian window (solid lines) for $N = 128$, $M = 16$ and $L = 16$: (a) Windows in time domain; (b) Frequency-domain spectra	42
3.6	Achievable frequency domain energy concentrations of proposed time-limited windows (dashed lines) and truncated Gaussian windows (solid lines) of length $N = 128$ for different values of M	43
3.7	Performance evaluation of proposed TST and BST: (a) Synthetic time series; TFR of (b) conventional ST; (c) ST with MLS for $k = 0.7$; (d) ST with MLS for $k = 2$; (e) 3PST; (f) 4PST; Amplitude of CM of (g) TST by varying k_2 for different values of k_1 ; (h) BST by varying k_4 for different values of k_3 ; TFR of proposed TST for (i) $k_1 = 25$, $k_2 = 0.4454$; (j) $k_1 = 45$, $k_2 = 0.4364$; TFR of proposed TST with modified scaling with $L_{th} = 5$ for (k) $k_1 = 25$, $k_2 = 0.4454$; (l) $k_1 = 45$, $k_2 = 0.4364$; TFR of proposed BST for (m) $k_3 = 50$, $k_4 = 7$; (j) $k_3 = 100$, $k_4 = 6$; TFR of proposed BST with modified scaling with $M_{th} = 5$ for (o) $k_3 = 50$, $k_4 = 7$; (p) $k_3 = 100$, $k_4 = 6$	46
3.8	Performance evaluation of proposed TST: (a) Synthetic seismic reflection data; TFR of (b) conventional ST; (c) ST with MLS for $k = 0.4$; (d) 3PST; (e) 4PST; (f) Proposed TST for $k_1 = 2$, $k_2 = 0.8$ and $L_{th} = 8$	49
3.9	Field Data	50
3.10	Performance evaluation of proposed TST: (a) 100th trace of 2D field data; TFR of (b) conventional ST; (c) ST with MLS for $k = 0.7$; (d) 3PST; (e) 4PST; (f) Proposed TST for $k_1 = 2$, $k_2 = 0.4$ and $L_{th} = 5$	51
3.11	Performance evaluation of proposed BST: (a) EEG signal; TFR of (b) conventional ST; (c) ST with MLS for $k = 2.45$; (d) 3PST; (e) 4PST; (f) Proposed BST for $k_3 = 7$, $k_4 = 4$ and $M_{th} = 7$	52

3.12	Performance evaluation of proposed BST: (a) Signal having multiple power quality disturbances; TFR of (b) conventional ST; (c) ST with MLS for $k = 2$; (d) 3PST; (e) 4PST; (f) Proposed BST for $k_3 = 10$, $k_4 = 3$ and $M_{th} = 2$	54
4.1	Variation of α^2 , β^2 and $\alpha^2\beta^2$ with μ for (a) $B = 1/16$, $M = 4$ and $N = 16$ with $\mu_{opt} = 0.437$ and $\mu_{eq} = 0.365$; (b) $B = 1/16$, $M = 4$ and $N = 128$ with $\mu_{opt} = 0.499$ and $\mu_{eq} = 0.497$	66
4.2	Upper bound of achievable time and frequency domain energy concentration for finite length sequences for $M = 4$ and $N = 20$	68
4.3	Upper bound of achievable time and frequency domain energy concentration for finite length sequences for (a) $N = 20$ and different values of M and B ; (b) $M = 4$, $B = 1/16$, and different values of N	69
4.4	Comparison of trade-off between α^2 and β^2 obtained with proposed OWFS and truncated DPSS	70
4.5	Comparison of trade-off between α^2 and β^2 obtained with proposed OWFS and different windows for (a) $B = 1/16$; (b) $B = 1/8$	71
4.6	Trade-off between α^2 and β^2 obtained with OCDW for (a) $N = 20$ and different values of M and L ; (b) $M = 2$, $L = 2$, and different values of N	73
4.7	Comparison of TFRs: (a) Synthetic signal composed of two components with AWGN (SNR = 18 dB); TFR of (b) ASTFT-t; (c) ASTFT-f; (d) ASTFT-tf; (e) GSTFT-tf; (f) OASTFT-tf	76
4.8	Normalized mean square error in IF estimation based on different adaptive TFRs	76
4.9	Selection of time and frequency intervals (M , L) for different values of γ and $N = 512$	79
4.10	Proposed OCDW for $M = 15$ and different values of γ in (a) Time domain; (b) Frequency domain	79
4.11	Proposed scaling: Approach for selecting time and frequency domain SD (σ_T) and (σ_F), respectively	81
4.12	Proposed scaling: SD of GW for $N = 512$ in (a) Time domain; (b) Frequency domain	82
4.13	Comparison of scaling criteria: SD of GW for length $N = 512$ in (a) Time domain; (b) Frequency domain	82
4.14	Comparison of scaling criteria used in GW based ST and proposed OST for $N = 512$ and $\gamma = 0.9$	83

4.15 Comparison of amplitude spectra of TFRs: (a) ST using CLS; (b) Proposed OST using CLS for $\gamma = 0.9$ and $\kappa = 2.3262$; ST with (c) MLS for $k = 2$; (d) PS for $p = 0.85$; (e) SS for $a = 0.2$ and $b = 6$; (f) OST with proposed FS with $\gamma = 0.9$ and $k_5 = 10$ 84

5.1 Proposed window of length $N = 512$ for different frequencies: (a) Windows in time domain; (b) Corresponding frequency domain spectra 90

5.2 (a) Comparison of HW, BGW and proposed AMKW of length $N = 512$: (a) Windows in time domain; (b) Corresponding frequency domain spectra 91

5.3 Comparison of different symmetrical and asymmetrical window based STs: (a) Synthetic time series; Amplitude spectrum of (b) Conventional ST; (c) 3PST; (d) 4PST; (e) BGW based ST; (f) Variant of BGW based ST; (g) HW based ST; (h) Proposed AMKW based ST with $k = 1$; (i) Proposed AMKW based ST with $k = 1.5$. The horizontal and vertical lines show the cross-sections used for Fig. 5.4 92

5.4 Amplitude spectra of the TFRs for the cross sections shown in Fig. 5.3: (a) Along first horizontal cross-section; (b) Along second horizontal cross-section; (c) Along vertical cross-section 94

5.5 Amplitude spectrum of different symmetrical and asymmetrical window based STs: (a) Earthquake seismogram; Amplitude spectrum of (b) Conventional ST; (c) 3PST; (d) 4PST; (e) BGW based ST; (f) Variant of BGW based ST; (g) HW based ST; (h) Proposed AMKW based ST with $k = 1$; (i) Proposed AMKW based ST with $k = 1.5$ 96

6.1 Comparison of amplitude spectrum of TFRs: (a) OST (b) OST combined with SST; (c) OST combined with RM; (d) Proposed product-ST for $k_1 = 64, k_2 = 0.42, k_3 = 20, k_4 = 100, M_{th} = 5$ and $L_{th} = 5$; (e) Proposed product-ST combined with SST; (f) Proposed product-ST combined with RM 103

6.2 Comparison of different TFA tools for San Fernando earthquake data (a) San Fernando earthquake data: TFR of (b) Conventional ST; (c) 3PST; (d) OST; (e) OST combined with SST; (f) OST combined with RM; (g) Proposed product-ST; (h) Proposed product-ST combined with SST; (i) Proposed product-ST combined with SST 106

6.3 Comparison of different TFA tools for Northridge earthquake data; (a) Northridge earthquake data; TFR of (b) Conventional ST; (c) 3PST; (d) OST; (e) OST combined with SST; (f) OST combined with RM; (g) Proposed product-ST; (h) Proposed product-ST combined with SST; (i) Proposed product-ST combined with SST 107





List of Tables

3.1	Comparison of TFRs shown in Fig. 3.7 in terms of CM	48
3.2	Comparison of TFRs shown in Fig. 3.8 in terms of CM	50
3.3	Comparison of TFRs shown in Fig. 3.10 in terms of CM	52
3.4	Comparison of TFRs shown in Fig. 3.11 in terms of CM	53
3.5	Comparison of TFRs shown in Fig. 3.12 in terms of CM	55
4.1	Comparison of windows in terms of $\alpha^2\beta^2$	80
4.2	Comparison of TFRs shown in Fig. 4.15 in terms of CM	85
5.1	Comparison of TFRs in terms of accuracy (in seconds) in detecting event's onset	95
5.2	Comparison of TFRs in terms of accuracy in detecting event's onset	97



List of Abbreviations



FT	:	Fourier Transform
IFT	:	Inverse Fourier Transform
FFT	:	Fast Fourier Transform
IFFT	:	Inverse Fast Fourier Transform
DFT	:	Discrete Fourier Transform
IDFT	:	Inverse Discrete Fourier Transform
TFA	:	Time-Frequency Analysis
TFR	:	Time-Frequency Representation
TFD	:	Time-Frequency Distribution
STFT	:	Short Time Fourier Transform
ASTFT	:	Adaptive Short Time Fourier Transform
WVD	:	Wigner-Ville Distribution
CWT	:	Continuous Wavelet Transform
ST	:	S-transform
DST	:	Discrete S-transform
GST	:	Generalized S-transform
GW	:	Gaussian Window
SD	:	Standard Deviation
MRA	:	Multi-resolution Analysis
CM	:	Concentration Measure
CLS	:	Conventional Linear Scaling
MLS	:	Modified Linear Scaling
PS	:	Power Scaling
SS	:	Sigmoid Scaling
3PS	:	Three Parameters Scaling
4PS	:	Four Parameters Scaling
3PST	:	Three Parameters Scaling based ST
4PST	:	Four Parameters Scaling based ST
FS	:	Fair Scaling

SST	:	Synchrosqueezing Transform
RM	:	Reassignment Method
IF	:	Instantaneous Frequency
GD	:	Group Delay
PSWF	:	Prolate Spheroidal Wave Function
DPSS	:	Discrete Prolate Spheroidal Sequences
PDPSS	:	Periodic Discrete Prolate Spheroidal Sequences
OWFS	:	Optimally Concentrated Window with Finite Support
OCDW	:	Optimally Concentrated Discrete Window
OST	:	Optimally Concentrated Discrete Window based ST
IEEE	:	Institute of Electrical and Electronics Engineers
SNR	:	Signal to Noise Ratio

Notations

Vectors and matrices are represented by boldface lower-case and upper-case letters, respectively. The elements of matrix \mathbf{A} are denoted by $[\mathbf{A}]_{i,j}$ where i and j represent i^{th} row and j^{th} column. The i^{th} element of vector \mathbf{k} is denoted by $[\mathbf{k}]_i$. $(\cdot)^T$ and $(\cdot)^H$ represent the transpose and hermitian transpose operations, respectively. $(\cdot)^\dagger$ and $|\cdot|$ denote the pseudo-inverse and modulus operations, respectively. $\lceil x \rceil$ rounds the value of x to the nearest integer greater than or equal to x . $\lfloor x \rfloor$ rounds the value of x to the nearest integer less than or equal to x . $\text{Tr}(\cdot)$ represents the trace of a matrix.

Chapter 1

Introduction

1.1 Background and Motivation

The analysis of the components of a signal plays an important role in the field of signal processing and its applications. The analysis of signal components rely on time or frequency or time-frequency domain representation of the data. The energy or instantaneous power distribution of the signal is shown in time domain representation. Some examples under time domain analysis include analysis of electrocardiogram (ECG) signals, signals having a single sinusoid, etc. Frequency domain representation is obtained by computing the Fourier transform (FT) of the signal whose magnitude spectrum represents energy distribution of the signal over frequency. The information regarding how fast or slow the heart rate is changing in an ECG signal or the frequency of the sinusoid in an electrical signal can be obtained by frequency domain analysis [1]. The frequency domain representation is obtained by integrating the time variable and vice versa. The time and frequency domain representations of the signal are non-localized with respect to the excluded frequency and time variable, respectively. Therefore, the time and frequency domain representations are well suited for stationary signals having similar statistical properties throughout the time.

However, most of the time series (speech, music, geophysical, medical signals, etc.) are non-stationary in nature where information is retained in change in frequency with time, and not in frequency itself. Hence, it is suitable to analyze such signals in both time and frequency domain simultaneously [2–4]. For time-frequency representation (TFR) of a signal, FT is made time dependent [2]. In a TFR, instead of being mutually exclusive, both time and frequency variables are present together. Consequently, a TFR is localized in both time and frequency domain simultaneously.

The conventional methods for time-frequency analysis (TFA) can be categorized into two groups. The first group includes linear time-frequency transforms which attempt to

make FT time dependent. The second group includes quadratic TFA techniques. Short time Fourier transform (STFT) [5], Gabor transform, wavelet transform (WT) [5–8] and S-transform (ST) [9–11] are some well-known time-frequency transforms listed under the first category whereas Wigner-Ville distribution (WVD) [5, 12] and Cohen class of distribution are listed under the later. The STFT was the first attempt to make classical Fourier analysis time dependent. It uses a fixed length window to localize the signal in time. After windowing, FT of the windowed segment is calculated. It produces a time localized FT of the signal. Since, the STFT uses a fixed length window for analyzing all frequencies, it leads to fixed resolution in the TFR. The WT is carried out by windowing the signal using variable windows. Scaled versions of mother wavelet are translated along the entire length of the signal. The WT incorporates the multi-resolution property, and is well suited for analysis of signals having low frequency components for longer duration and high frequency components for shorter duration. However, it provides local phase information. WVD provides high energy concentration in the TFR. However, it suffers from the cross term problems. ST is an advancement of the STFT and WT. It has direct relationship with FT, and retains the absolutely referenced phase property of STFT. It provides frequency invariant amplitude response along with multi-resolution property. These properties of ST have led to its wide usage in various fields such as geophysics [13–16], power system engineering [17–25], biomedical engineering [26–31], biometric [32], etc.

In an ideal case, the TFR is expected to show the spectral information of the signal at correct time instants without cross-information about adjacent instants [33]. The main objective of TFA is to provide a highly concentrated TFR which can be as close as possible to an ideal TFR [34]. The conventional ST uses a Gaussian window (GW) whose width varies as inversely proportional to the frequency. This scaling criterion provides very large window width for lower frequencies, and very short window width for higher frequencies, and hence leads to unnecessary deterioration in time and frequency resolution at lower and higher frequencies, respectively. To improve the energy concentration, several variants of ST have been proposed in literature [35–38]. Frequency resolution of ST has been improved at the cost of degradation in time resolution by multiplying the window width by a constant scaling factor k [20]. Sejdíć and Djurović [39] have introduced a parameter p , ($p < 1$) as an exponent of analysis frequency. Unlike the linear increment, the window width increases exponentially in frequency domain, and provides better frequency resolution at higher frequencies as compared to modified linear scaling [20] while retaining similar time resolution at lower frequencies as that of conventional ST. The parameter p is chosen based on the concentration measure (CM) [40]. Multiple parameters [13, 19] have been introduced to improve the energy concentration in the TFR

of ST. The optimum value of these parameters are chosen so as to maximize the CM of the TFR. Three or more parameters based approaches are often very complex since there is no closed form dependence of energy concentration on introduced parameters. Hence, these approaches rely on brute force search over the parameter space. It results in evaluation of huge number of TFRs. Thus, adding more parameters and optimizing those using CMs or heuristic algorithms are very tedious and computationally complex tasks. Instead of using a GW as kernel of ST, other window functions are also proposed in literature for specific applications. The asymmetrical windows are used for accurate detection of arrival and termination time of certain events [41,42]. An adaptive Dolph Chebyshev window based ST has been proposed by Yao *et al.* to improve TFR characteristics for certain class of signals [43]. The aforementioned literature indicates that a suitable window needs to be chosen depending on the application. Moreover, practical implementation needs a discrete window with finite support. The existing approaches use sampled and truncated version of continuous window which may no longer hold the desired properties, and often lead to inconsistency in time and frequency domain computation of ST [44].

The classical TFA tools and their variants suffer from poor time-frequency resolution due to Heisenberg uncertainty principle or unwanted cross terms. It may lead to unreliable characterization of the nonlinear behavior of non-stationary signals. In order to achieve near ideal TFR, some advanced post processing methods have been proposed in literature such as reassignment method (RM) [45,46] and synchrosqueezing transform (SST) [47,48]. These tools have the ability to reassign or squeeze the time-frequency coefficients obtained by classical TFA methods into the instantaneous frequency (IF) trajectory [49,50]. Although the conventional linear TFRs along with RM and SST provide very narrow ridges as compared to the conventional TFRs, their ability to separate out two signal components still depend on the width of the window in time and frequency domains. For SST and RM to properly resolve two modes in frequency, these modes must be separated in frequency by at least the bandwidth of the used window. Similarly, to separate out two signal components in time, the time separation of these components must be more than the support of the window [51]. Resolving closely spaced signal components in both time and frequency domain simultaneously using SST and RM techniques remains a challenge.

1.2 Research Objectives

The above discussion provides motivation for carrying out more research work on window functions and scaling criterion to improve the energy concentration in the TFR of ST. Consequently, the main objective of this thesis is to enhance the energy concentration in the TFR of ST by using modified window and scaling criterion, and further by using post

processing methods. To be more specific, the contributions of this thesis are elaborated in the following research objectives.

ST based on Optimally Concentrated Time-limited and Band-limited Windows

In order to improve the energy concentration in the TFR for analyzing time-limited and band-limited signals, optimally concentrated time-limited and band-limited discrete windows are proposed. The motivation behind the usage of time-limited windows for TFA is to accurately localize a signal in a given time interval with minimum spreading in frequency. The desired discrete window is designed to provide maximum energy concentration in finite frequency interval while being strictly limited in finite time interval. This approach can be potentially useful in precise detection of event initiation and termination, and determination of total duration of signal such as duration of heart rate signals [52], p and s wave arrival and termination in seismology [41, 42, 53, 54], etc. Similarly, the idea behind the proposed band-limited window is to accurately localize a signal in a given band with minimum spreading in time. These band-limited windows have wide applications, such as analysis of band-limited electroencephalogram (EEG) signals [55], optimal basis design for band-limited signal, etc. Based on the time-limited and band-limited windows, two variants of ST are proposed, namely TST and BST. The efficacy of the proposed TST is examined using seismic earthquake and reflection data. Similarly, the efficacy of the proposed BST is examined using band-limited EEG data and signal having multiple power quality disturbances.

Simultaneous Time and Frequency Domain Energy Concentration for Finite Length Sequences

This objective deals with the achievable optimal trade-off between time and frequency domain energy concentration for finite length sequences. Slepian and Pollak have proposed optimal sequences to simultaneously maximize the time and frequency domain energy concentrations for a given time interval and a frequency band for continuous time continuous frequency [56] and discrete time continuous frequency [57] scenarios. However, these sequences are of infinite support.

For most of the practical applications where we often encounter with finite duration signals, it is desired to have simultaneously concentrated discrete window with finite support. To this extent, this objective focuses on maximally achievable trade-off between

time and frequency domain energy concentration in discrete time continuous frequency and discrete time discrete frequency scenarios for discrete time finite length sequences. A straight forward approach is to truncate the simultaneously concentrated discrete prolate spheroidal sequences (DPSS) [57] to desired finite length, but the resulting window will no longer guarantee to be optimal. Therefore, from practical standpoint and out of mathematical curiosity, this objective aims at designing an optimal compact window with finite support which can simultaneously maximize the energy concentration in finite time interval and finite frequency band. The problem of simultaneous maximization of time and frequency domain energy concentrations is formulated as the maximization of weighted linear combination of desired energy CMs in time and frequency domains. The problem is solved through eigenvalue decomposition to obtain Pareto-optimal solutions. Further, upper bounds of achievable time and frequency domain energy concentration for finite length sequences and associated properties are derived.

A novel optimally concentrated discrete window (OCDW) is designed by solving a constraint optimization problem of maximization of the product of time and frequency domain energy concentration in given time and frequency intervals. Further, it is extended to design an OCDW based ST (OST) for multi-resolution analysis. A new scaling criterion is also proposed for OST which prevents unnecessary deterioration in frequency resolution at higher frequencies, and time resolution at lower frequencies. The efficacy of the proposed approach is examined using a synthetic signal having multiple power quality disturbances.

Sharp Detection of Event's Onset with Asymmetrical Kaiser Window based ST

In various fields such as seismology, biomedical engineering, audio and speech signal processing, etc. the main motivation behind signal analysis is event recognition [42, 58, 59]. Reliable detection and identification of seismic events are extremely important for accurate estimation of magnitude and location of these events. Different time or frequency domain methods for onset detection of events are discussed in literature [60–64]. These time or frequency domain methods are suitable for analyzing signals having less noise and randomness as these analyze the seismic traces either in time or in frequency domain. However, the seismic traces are non-stationary in nature and mostly severely contaminated with noise. It is well suited to analyze these kind of signals in both time and frequency domain simultaneously [65].

Many variants of ST have been proposed in literature using asymmetrical windows for sharp detection of event's onset. A bi-Gaussian window (BGW) based ST has been

proposed in literature for detection of various seismic events [53,59,66,67]. Similarly, an asymmetrical hyperbolic window (HW) based ST has also been proposed in literature to determine different events in noisy seismograph [42,54] and power quality disturbances [68,69]. However to provide asymmetry, welding of two functions leads to discontinuities.

In this objective, an asymmetrical modified Kaiser window (AMKW) based ST is proposed for analyzing the time-frequency content of a broadband earthquake seismogram. The multi-resolution analysis and frequency dependent asymmetry are obtained by modifying the β parameter of first order Bessel function. The proposed method is tested by using synthetic seismic trace and real earthquake data.

Reassignment of Energy in the TFRs of OST and product-ST

In order to exploit the sparsity in the signal as well as provide better visualization in the TFR, post processing techniques are deployed to reassign the energy in the TFR closer to prominent frequencies. In recent years, the post processing methods such as RM and SST are widely used in various disciplines such as, earth sciences [70–72], biomedical engineering [73], mechanical engineering [74], civil engineering [75–77], etc. However, the efficiency of these post processing methods depends on separability of modes in time and frequency domains. To counter this shortcoming, the SST and RM are deployed on the TFR of OST, and further investigated for detecting multiple power quality disturbances. It is found that the OST combined with RM and SST provides better visualization as compared to other counterparts of ST.

Further, a product-ST is proposed for better visualization by multiplying the TFRs of TST and BST. The concepts of RM and SST are incorporated in the product-ST. It is found that the product-ST combined with RM and SST provides better visualization and frequency detection accuracy as compared to its OST counterpart.

1.3 Organization of Thesis

The entire work is carried out to accomplish aforementioned four objectives, and systematically presented in this thesis through seven different chapters including this chapter. A brief summary of remaining six chapters are presented below.

Chapter 2: This chapter begins with a detailed literature review of the work done by various researchers in the field of maximization of energy concentration in time and

frequency domain simultaneously. This chapter also describes the mathematical concepts and basic fundamentals of the relevant methodologies of simultaneously concentrated sequences, the generalized ST with different windows and different scaling criteria. The working principle and the performance analysis of various TFA techniques are discussed. The chapter is concluded with a brief summary of technical gaps which are addressed in the thesis.

Chapter 3: This chapter presents optimally concentrated time-limited and band-limited windows for the purpose of enhancing the energy concentration in the TFR of ST. In the first part of this chapter, two optimally concentrated windows and their associated properties are presented and discussed. In the second part of this chapter, two variants of ST, namely TST and BST are proposed. In addition, a modified scaling criterion is proposed for TST and BST. The accuracy of the proposed approach is tested through simulations.

Chapter 4: This chapter discusses the maximum achievable energy concentration in both time and frequency domain simultaneously. A novel OCDW is proposed, and further extended to design OST. A new scaling criterion is also proposed for OST to prevent unnecessary deterioration in frequency resolution at higher frequencies, and time resolution at lower frequencies. The efficacy of the proposed approach is examined for detection of multiple disturbances in a synthetic power quality signal.

Chapter 5: This chapter proposes an AMKW based ST for sharp detection of event's onset. In first part, conventional Kaiser window is modified to provide frequency dependent asymmetry. Further, the proposed window is extended to design AMKW based ST. The efficacy of the proposed approach is examined for detection of various events in synthetic seismic and real earthquake data.

Chapter 6: In this chapter, to provide better visualization in the TFR of OST, the energy in the TFR is reassigned using RM and SST. The performance of the resulting TFR is investigated for detecting multiple power quality disturbances. Further, a product-ST is proposed for better visualization by multiplying the TFRs of TST and BST. The concept of RM and SST is generalized for product-ST.

Chapter 7: This chapter concludes the present study, and summarizes the contributions discussed in chapters 3 to 6. Further, this chapter lays down the possible research directions for future work.



Chapter 2

Literature Survey

2.1 Fourier Transform

The FT [78] of a continuous signal $x(t)$ can be defined as

$$X(f) = \int_{-\infty}^{\infty} x(t) e^{-i2\pi ft} dt \quad (2.1)$$

and conversely, the time domain signal can be reconstructed from $X(f)$ by taking inverse FT (IFT) as

$$x(t) = \int_{-\infty}^{\infty} X(f) e^{i2\pi ft} df \quad (2.2)$$

The FT provides information about all frequency components of a time series.

The discrete FT (DFT) of a N -point time series with sampling time interval T is defined as,

$$X\left[\frac{k}{NT}\right] = \frac{1}{N} \sum_{n=0}^{N-1} x[nT] e^{-\frac{i2\pi kn}{N}} \quad (2.3)$$

where $k, n = 0, 1, 2, \dots, N - 1$. The inverse DFT of $X[k/NT]$ can be defined as,

$$x[nT] = \sum_{k=0}^{N-1} X\left[\frac{k}{NT}\right] e^{\frac{i2\pi kn}{N}} \quad (2.4)$$

2.2 Motivation for Time-Frequency Analysis

Time localization of frequencies is absent in Fourier amplitude spectrum. Therefore, the FT is only suitable for analyzing the stationary signals. Fig. 2.1 shows the amplitude and phase spectra of FT for increasing and decreasing chirp signals. The figure reveals that the information about spectral components is hidden in the phase spectrum. The amplitude

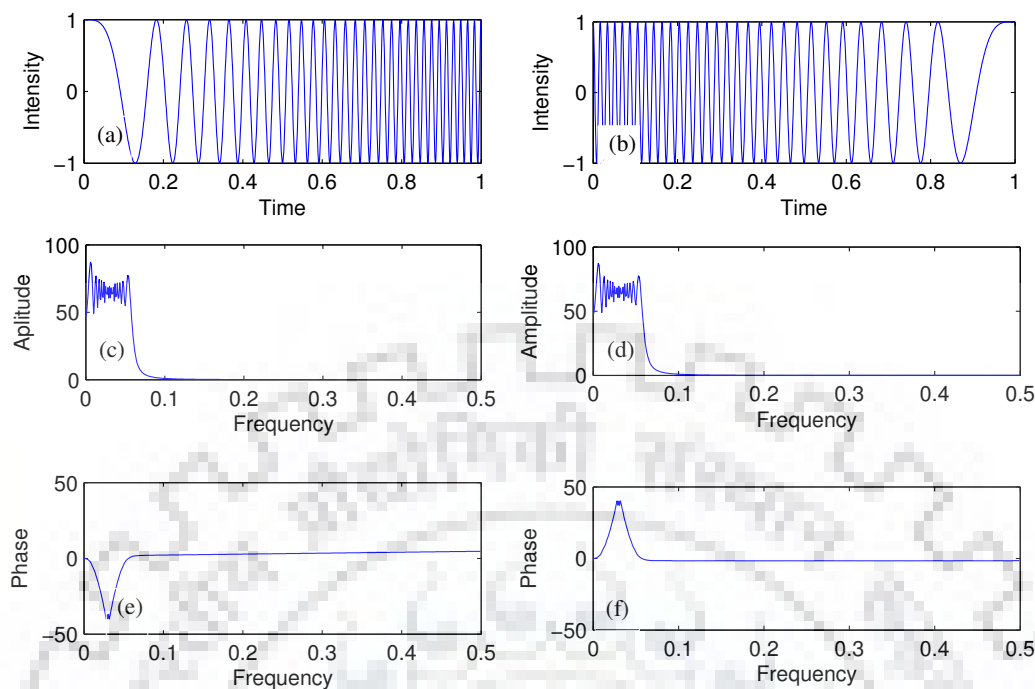


Fig. 2.1: (a) A increasing chirp signal; (b) A decreasing chirp signal; (c) Amplitude spectrum of increasing chirp signal shown in (a); (d) Amplitude spectrum of decreasing chirp signal shown in (b); (e) Phase spectrum of increasing chirp signal shown in (a); Phase spectrum of decreasing chirp signal shown in (b)

spectra for both increasing and decreasing chirps are same i.e. Fourier amplitude spectra can not differentiate the two chirps. However, their phase spectra are different which consist of the hidden information that these two signals are different. Therefore, the time localization of the spectral components is necessary in nonstationary signal analysis. Hence, joint TFA is a possible solution to the aforementioned problem.

TFA studies signals in both time and frequency domain simultaneously, and provides a TFR. TFA is extensively used in various applications because most of the signals in practice are non-stationary. TFR reveals which frequency components are present at each time instant in the signal. Some well known TFRs are STFT [5, 79–81], WVD [5, 82], WT [5, 83, 84] and ST [9].

2.3 Short Time Fourier Transform (STFT)

In STFT [85], a non-stationary signal is segmented into narrow time intervals (narrow enough) where it would be stationary. For example, the signal considered in Fig. 2.2(a) is stationary for every 250 time intervals. This segmentation of the signal into narrow intervals is carried out by performing windowing process. The width of the window is

chosen in such a way that the windowed segments of the signal are stationary. Further, FT of each windowed segment of the signal is computed. If a windowed segment is stationary for that width of the window, then the corresponding STFT spectrum provides correct representation of the frequency components in that segment. The whole process is repeated by translating the window along the entire length of the signal. STFT of a signal can be defined as

$$STFT(\tau, f) = \int_{-\infty}^{\infty} x(t) e^{-i2\pi ft} (w(t - \tau)) dt \quad (2.5)$$

where τ is used as a translation parameter. $w(t)$ represents the window function.

2.3.1 Limitation of STFT

The conventional STFT uses fixed length window function to analyze each frequency, and hence leads to fixed time and frequency resolution. The Heisenberg uncertainty principle states that it is not possible to know the exact spectral component at exact time instant. The limitations of STFT are attributed to shape and width of the window function. The window should be of appropriate size for getting good time and frequency resolutions. In conventional STFT, the window width is fixed. As the window width decreases, time resolution improves at a cost of degradation in frequency resolution.

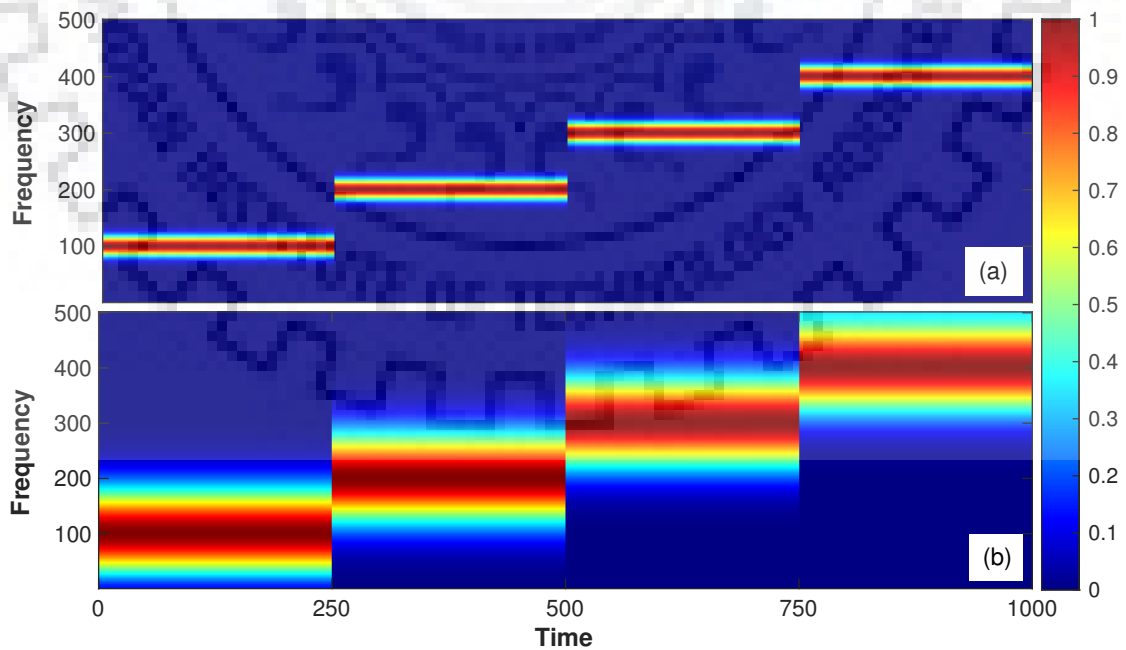


Fig. 2.2: Amplitude spectrum of the STFT of non-stationary signal: (a) The width of the window is 0.1; (b) The width of the window is 0.05

The signal considered in Fig. 2.2 is generate as

$$x(t) = \begin{cases} \sin(2\pi 100t) & 0 \leq t < 250 \\ \sin(2\pi 200t) & 250 \leq t < 500 \\ \sin(2\pi 300t) & 500 \leq t < 750 \\ \sin(2\pi 400t) & 750 \leq t < 1000 \end{cases} \quad (2.6)$$

The GW is used for windowing. It is clearly observed from Fig. 2.2(b) that if the window width decreases in time domain, it leads to degradation in the frequency resolution.

If the time domain signal has well separated spectral components (as the above example), then frequency resolution may be scarified upto certain extent for getting good time resolution. However, in practical scenario, the signals do not generally have well separated spectral components. Further, it is difficult to choose an appropriate window size to get satisfactory time and frequency resolution.

Fig. 2.3(a) shows a time series consisting of a high frequency component for very

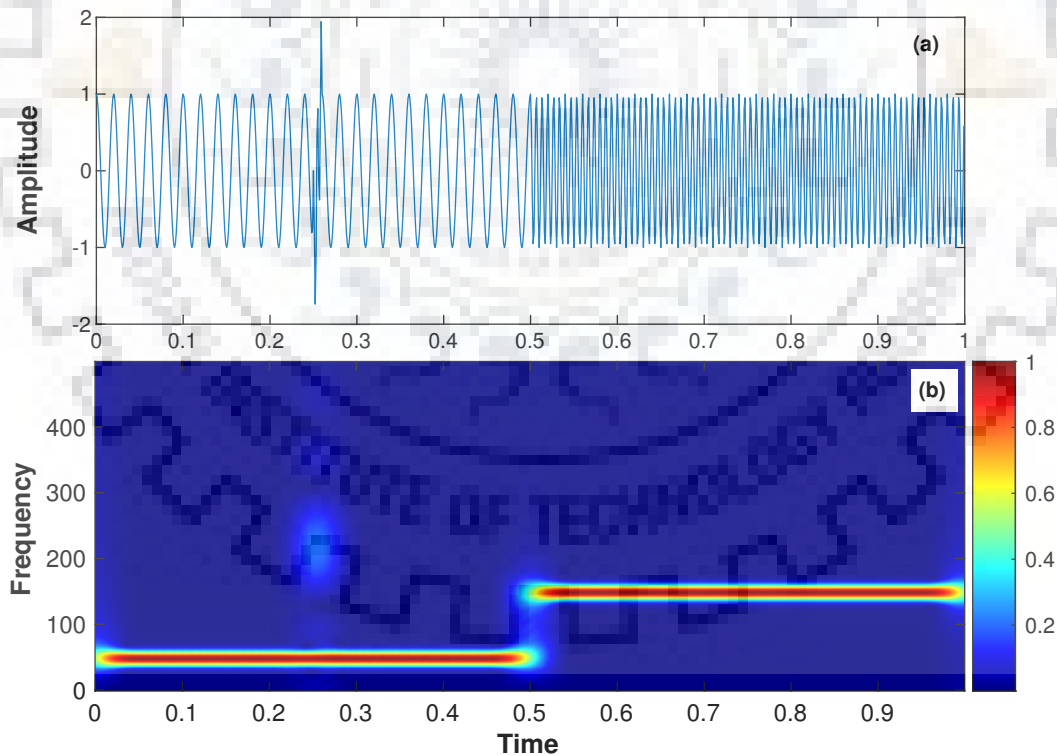


Fig. 2.3: Illustration of the limitation of the STFT: (a) Synthetic test time series; (b) Amplitude spectrum of the STFT. Test time series of 1000 samples consists of a low frequency signal of 50 Hz for the first half of its duration, a high frequency signal of 150 Hz for the second half of the duration, and a high frequency burst from samples 20 to 30

small duration along with low frequency components for long duration. The STFT can't resolve the high frequency component correctly until the window width is same as that of the duration of the high frequency component. The frequency resolution of low frequency components will be poor if the width of the window is too small. The GW having standard deviation (SD) of 0.01, is used for windowing. It can be observed in Fig. 2.3(b) that the short duration high frequency burst is not resolved properly. The frequency resolution is same for all frequency components due to the fixed length window.

2.4 Hilbert-Huang Transform (HHT)

The Hilbert-Huang transform (HHT) [86] is used for analysis of nonlinear and nonstationary data. Instead of apriori selection of spectral components such as sinusoidal waves or wavelets as the basis, HHT provides adaptive modes derived from the data. A signal is decomposed into intrinsic mode functions (IMFs) using empirical mode decomposition (EMD) [87], and further finds IF using Hilbert transform (HT) [88]. The HHT is an empirical approach comprising of two steps, EMD followed by HT.

2.4.1 Empirical Mode Decomposition

The EMD [86] decomposes a signal into a set of IMFs using sifting process. The IMFs must satisfy the following two fundamental conditions:

- The number of extrema (maxima and minima) and the number of zero-crossings should not exceed one
- The local mean obtained from upper and lower envelopes should be equal to zero

The sifting process for a signal $x(t)$ can be described as follows:

1. All local extrema in the signal are found out and the envelope of extrema is approximated with suitable spline.
2. The mean value m_1 of the local extrema at each instance is calculated.
3. Difference of the mean m_1 from $x(t)$ is the first component, $h_1 = x(t) - m_1$
4. Ideally, h_1 should be an IMF. However, due to overshoots and undershoots in the signal, there are some redundant extrema. Therefore, the sifting process is repeated. In next step of sifting process, h_1 is considered as the signal, the mean of its local extrema is calculated and the difference between h_1 and its mean m_{11} is the new component, $h_{11} = h_1 - m_{11}$. After n sifts, the first IMF $c_1 = h_{1n} = h_{1(n-1)} - m_{1n}$ is obtained.

5. The first IMF c_1 contains the highest frequency component. After computing c_1 , the rest of the data is then separated from the original signal, $r_1 = x(t) - c_1$
6. The whole process (steps 1 to 5) is repeated to obtain other IMFs by considering residue r as the signal.

The sifting process is stopped when the component c_n or the residue r_n is very small or when r_n becomes monotonic. Therefore, the signal $x(t)$ can be represented as

$$x(t) = \sum_{i=1}^n c_i + r_n \quad (2.7)$$

2.4.2 Hilbert Transform

The Hilbert transform [88] of any signal $x(t)$ can be denoted as,

$$y(t) = H[x(t)] = \frac{1}{\pi} PV \int_{-\infty}^{\infty} \frac{x(\tau)}{t - \tau} d\tau \quad (2.8)$$

where PV indicates the principal value of the singular integral. The analytic version of $x(t)$ can be denoted as

$$z(t) = x(t) + iy(t) = a(t)exp(i\theta(t)); \quad (2.9)$$

where,

$$a(t) = \sqrt{x^2(t) + y^2(t)}, \quad \theta(t) = \arctan\left(\frac{y(t)}{x(t)}\right) \quad (2.10)$$

The instantaneous frequency is given as

$$f = \frac{1}{2\pi} \frac{d\theta(t)}{dt} \quad (2.11)$$

2.4.3 Hilbert Spectrum

In order to find the IF, the HT is applied to each IMF component obtained from EMD process. The different IMFs may have certain common frequencies. The amplitudes of same frequency components of different IMFs at a particular time are added to get the TFR of the signal which is known as Hilbert spectrum.

Fig. 2.4 shows the Hilbert Spectrum of the signal shown in Fig. 2.3(a). It can be observed that time and frequency resolution for both low and mid frequency components are good, and the high frequency burst is also clearly visible. However, at the transition instances, some extra frequencies are observed. This is due to the abrupt change in frequencies or mode mixing in IMFs.

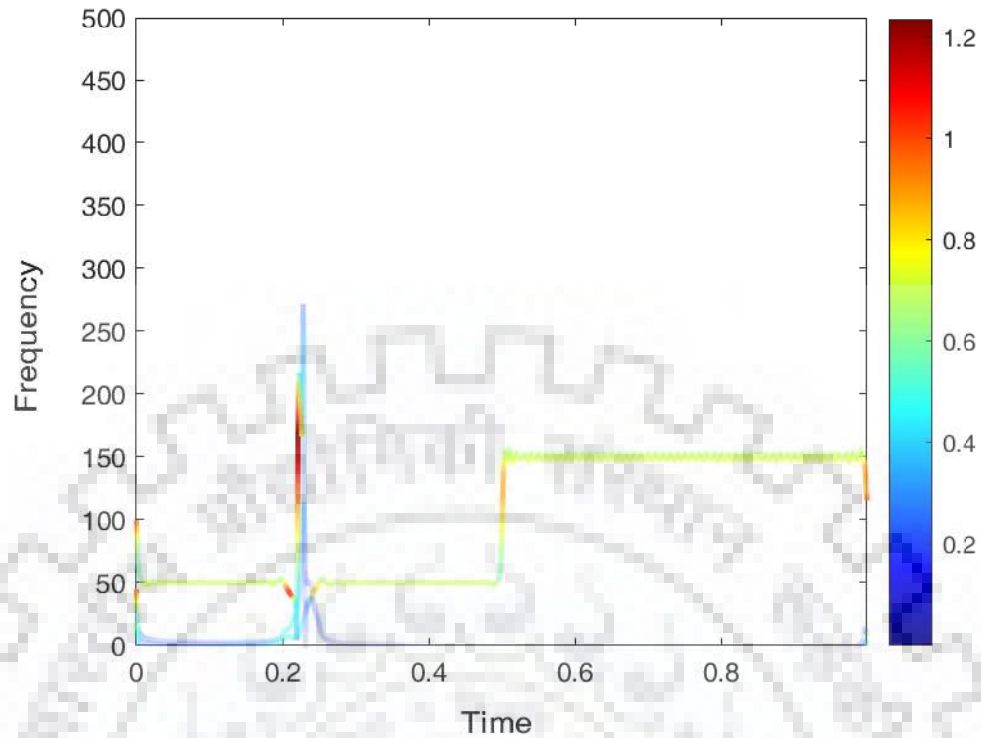


Fig. 2.4: Hilbert spectrum for the test time series shown in Fig. 2.3(a)

2.4.4 Limitations of HHT

The main limitation of HHT is mode mixing in EMD process where a single IMF contains multiple frequencies of different order or the same scale might be present in different IMFs. To avoid mode mixing, a new approach was proposed called the Ensemble Empirical Mode Decomposition (EEMD) [89]

2.4.5 Ensemble Empirical Mode Decomposition

The EEMD [89] uses white noise for analyzing the signal. The noise is added to the signal, and thereafter IMFs are calculated. This process is iterated several times. The ensemble of the IMF components obtained in several trials are considered as the final IMF components. White noise provides additional extrema in all frequency components. Therefore, an artificial scale is added that ensures that the frequencies in one IMF are within the same range, and are not mixed any more. Since the mean of white noise is zero, on taking the ensemble of IMFs of the same scale, the noise gets canceled out, and only the signal components remain.

A novel adaptive decomposition method is also reported in literature know as variational mode decomposition (VMD) [90]. The VMD determines the relevant bands for decomposition adaptively, and corresponding modes can be estimated concurrently. It

perfectly balances errors by solving variational problems to obtain relevant IMFs for separating the different components of signals.

2.5 Continuous Wavelet Transform (CWT)

CWT [91] analyzes the signal based on the concept of multi-resolution analysis (MRA). Unlike in STFT, where all spectral components are resolved equally, CWT analyses a signal at different frequencies with different resolutions. MRA in CWT provides good time resolution at high frequencies and good frequency resolution at lower frequencies. The CWT of a continuous signal $x(t)$ can be represented as

$$CWT_X^\psi(\tau, s) = \frac{1}{\sqrt{|s|}} \int_{-\infty}^{\infty} x(t) \psi^* \left(\frac{t - \tau}{s} \right) dt \quad (2.12)$$

where $\psi(t)$ represents the mother wavelet. The variables τ and s denote translation and scale parameters, respectively. The term ‘wavelet’ refers to the wave’s oscillatory property in compact form, and ‘mother’ implies that all the transforming window functions are derived from this function. Scaling operation either dilates or compresses the mother wavelet based on the value of the scale parameter. Larger scale value leads to dilation of the mother wavelet, and small scale value leads to compression of the mother wavelet.

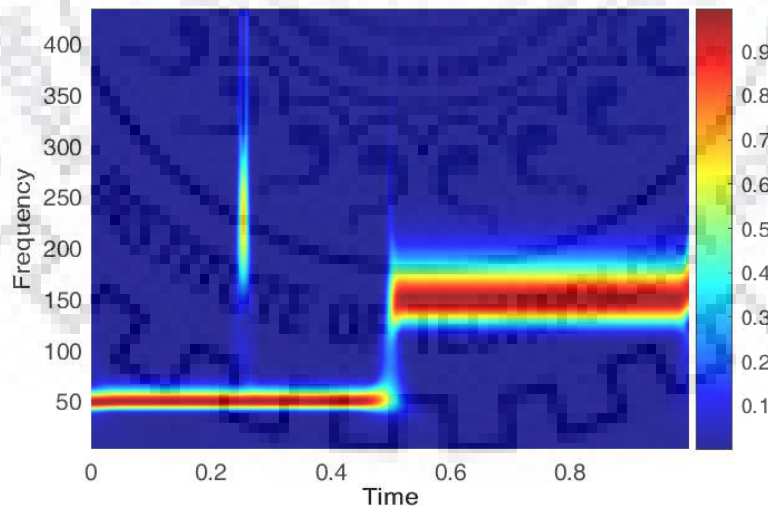


Fig. 2.5: Amplitude spectrum of CWT for the test time series shown in Fig. 2.3(a)

The TFR of CWT is shown in Fig. 2.5 for the signal considered in 2.3(a). The ‘morse’ wavelet is used as mother wavelet. Frequency resolution is better for lower frequencies, and time resolution is better for high frequencies.

2.5.1 Limitations of CWT

1. Frequency sampling in CWT: The discrete FT has uniform sampling of frequency space. CWT has octave scaling where scale is related to frequency as, $s = \frac{1}{\sqrt{|f|}}$. Hence, the lower frequencies are oversampled and higher frequencies are undersampled (relative to FT).

2. Local phase information: Wavelet transform provides locally referenced phase information. For a particular scale value, it has a varying phase profile for full range of phase $(-\pi, \pi)$ which is not similar to the phase of the signal.

3. Varying amplitude with varying frequency: Amplitude response of the CWT is scale dependent. At higher scales (lower frequencies), window is wider, and normalization factor $\frac{1}{\sqrt{|s|}} = \sqrt{f}$ normalizes the transformed signal in appropriate proportion. As scale decreases (frequency increases), width of window decreases, and normalization factor can't normalize the signal in appropriate proportion. Thus, amplitude spectrum of CWT shows higher values of lower frequencies, and the amplitude decreases as frequency increases.

2.5.2 Empirical Wavelet Transform

Empirical wavelet transform (EWT) [55] combines the merits of adaptive decomposition technique EMD and WT. Therefore, it is a signal dependent analysis technique that doesn't use predefined basis unlike WT. It uses wavelet filter banks which are adaptive according to signal. The steps involved in EWT can be summarized as follows:

- Fourier spectrum of the signal is obtained in the frequency range $[0, \pi]$ using FFT
- The Fourier spectrum is segmented into different modes using boundary selection methods. If the boundary frequencies are denoted as $\Omega_{i=0, \dots, N}$, the Fourier segments can be represented as $[0, \Omega_1], [\Omega_1, \Omega_2], \dots, [\Omega_{N-1}, \pi]$ where $\Omega_0 = 0$ and $\Omega_N = \pi$
- Based on the idea of Littlewood-Paley and Meyer's wavelets [92], empirical wavelet based filter is generated for each Fourier segment.

The FT of empirical scaling and wavelet functions can be represented as

$$\phi_i(\Omega) = \begin{cases} 1, & |\Omega| \leq (1 - \lambda)\Omega_i \\ \cos\left(\frac{\pi\beta(\lambda, \Omega_i)}{2}\right), & (1 - \lambda)\Omega_i \leq |\Omega| \leq (1 + \lambda)\Omega_i \\ 0, & \text{otherwise} \end{cases} \quad (2.13)$$

and

$$\psi_i(\Omega) = \begin{cases} 1, & (1 + \lambda)\Omega_i \leq |\Omega| \leq (1 - \lambda)\Omega_{i+1} \\ \cos\left(\frac{\pi\beta(\lambda, \Omega_{i+1})}{2}\right), & (1 - \lambda)\Omega_{i+1} \leq |\Omega| \leq (1 + \lambda)\Omega_{i+1} \\ \sin\left(\frac{\pi\beta(\lambda, \Omega_i)}{2}\right), & (1 - \lambda)\Omega_i \leq |\Omega| \leq (1 + \lambda)\Omega_i \end{cases} \quad (2.14)$$

where

$$\beta(\lambda, \Omega_i) = \alpha\left(\frac{|\Omega| - (1 - \lambda)\Omega_i}{2\lambda\Omega_i}\right) \quad (2.15)$$

The parameter λ is chosen such that the empirical scaling and wavelet function form a tight and can be represented as

$$\lambda \leq \min_i \left(\frac{\Omega_{i+1} - \Omega_i}{\Omega_{i+1} + \Omega_i} \right) \quad (2.16)$$

The function $\alpha(t)$ is an arbitrary function that can be represented as

$$\alpha(t) = \begin{cases} 0, & t \leq 0 \\ 1 - \alpha(1 - t), & \forall t \in [0, 1] \\ 1, & t \geq 1 \end{cases} \quad (2.17)$$

The HT is applied on filtered subband signal, and the Hilbert spectrum or TFR of EWT is obtained.

A novel Fourier–Bessel series expansion (FBSE) based EWT is also reported in literature [93] in which a scale space based method is applied on FBSE based spectrum of the signal for accurate estimation of boundary frequencies. FBSE based EWT provides improved frequency resolution as compared to EWT.

Tunable-Q WT [94] (TQWT) is another efficient variant of WT in which Q -factor (QF) can be tuned. By varying QF, number of oscillations in mother wavelet can be varied. Hence, a suitable mother wavelet can be selected by varying QF according to the signal. The TQWT is more computationally efficient, and has perfect reconstruction property.

2.6 Chirplet Transform

The chirplet transform (CT) [95] can be considered as an extension of the STFT and WT. In CT, the chirplet (piece of chirp) is used similarly as wavelet (piece of wave) is used in WT and a constant-size portions of a wave (sinusoid) is used in STFT. These chirplets are scaled, shifted, and their phase is also changed. The complex-valued chirplets are

generally used for avoiding the mirroring effect along zero frequency.

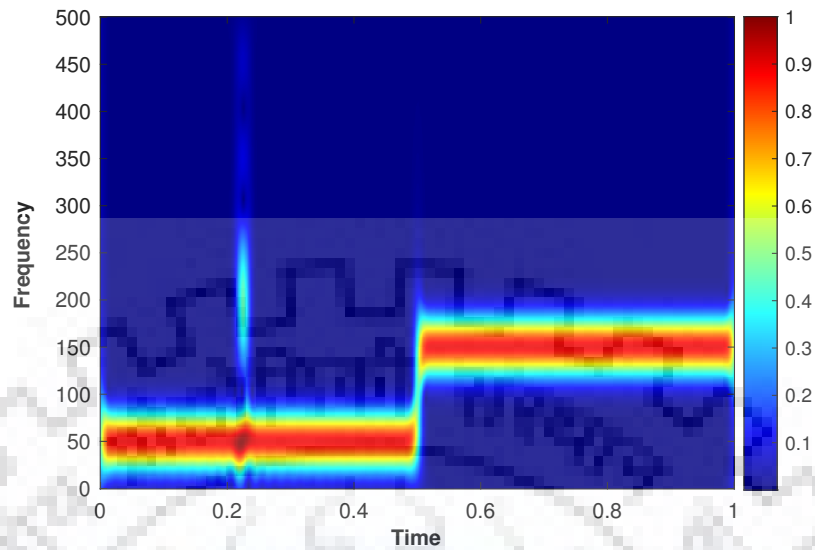


Fig. 2.6: Amplitude spectrum of CT for the test time series shown in Fig. 2.3(a)

It can be observed in Fig. 2.6 that all the three frequency components are clearly visible in chirplet transform. The frequency resolution for low frequency components is poorer than that of STFT and CWT. The time and frequency resolution for both mid and high frequency bursts are better than that of STFT and CWT.

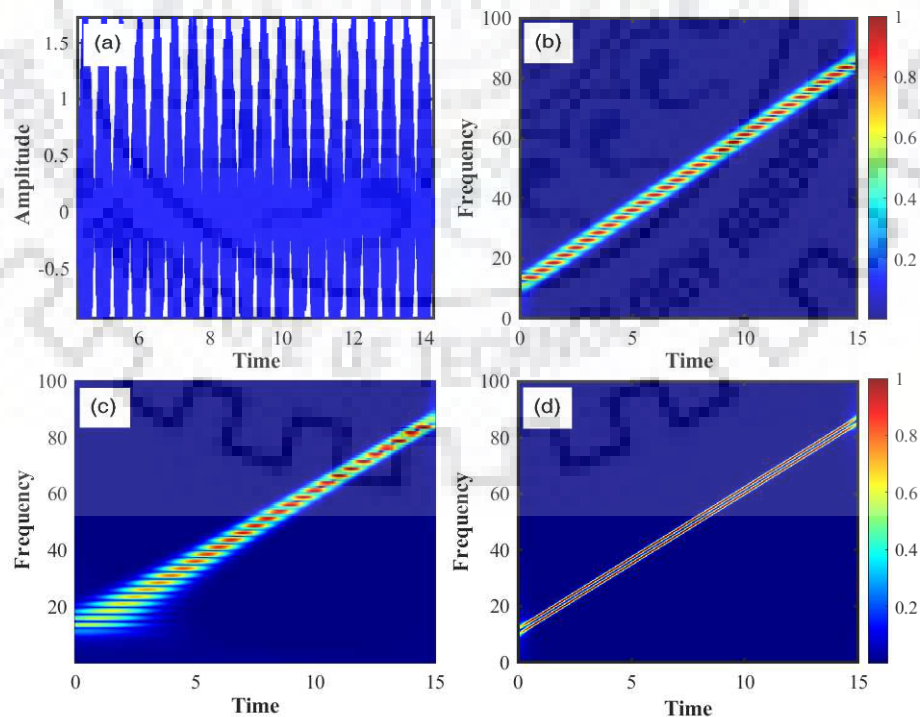


Fig. 2.7: (a) Test time series; Amplitude spectrum of (b) STFT; (c) CWT; (d) CT

The CT is more beneficial for analyzing the signals having chirps. A test signal having two linearly increasing chirps is considered and shown in Fig. 2.7(a). It can be observed in Figs. 2.7(b) and 2.7(c) that the TFRs of STFT and CWT, respectively are unable to resolve the two chirps. The chirps can be resolved using CT which is evident in Fig. 2.7(d).

The novel recent higher dimensional generalization of WT is also reported in literature which is known as Curvelet transform [96]. It is a multiscale directional transform that allows an almost optimal nonadaptive sparse representation of objects with edges. It represents images at different scales and different angles. It approximates the curved singularities non-adaptively using very few coefficients. It also maintains its coherency under the action of the wave equation in a smooth medium.

2.7 S-transform (ST)

ST [97] was developed by Stockwell in 1996. It retains the good features of STFT and CWT with additional important properties which can overcome their limitations. It has progressive resolution property which overcomes the resolution problem of the STFT. It provides absolutely referenced phase information. It also provides amplitude response which is not dependent on frequency, and hence overcomes the limitations of CWT. These properties of ST have led to its wide usage in various disciplines such as power system engineering [19, 98–101], biomedical engineering [102, 103], geophysics [13, 14], etc.

2.7.1 Derivation of ST from STFT

Consider a normalized GW

$$w(t) = \frac{1}{\sigma\sqrt{2\pi}} e^{-\frac{t^2}{2\sigma^2}} \quad (2.18)$$

Combining (2.5) and (2.18)

$$STFT(\tau, f, \sigma) = \frac{1}{\sigma\sqrt{2\pi}} \int_{-\infty}^{\infty} x(t) e^{-\frac{(t-\tau)^2}{2\sigma^2}} e^{-i2\pi ft} dt \quad (2.19)$$

In ST, a scalable (frequency dependent) GW is used, *i.e.* $\sigma = \frac{1}{|f|}$. The ST can be represented as follows

$$S(\tau, f) = \frac{|f|}{\sqrt{2\pi}} \int_{-\infty}^{\infty} x(t) e^{-\frac{(t-\tau)^2 f^2}{2}} e^{-i2\pi ft} dt \quad (2.20)$$

$S(\tau, f_0)$ is termed as a voice (a single row of the TFR of ST) corresponding to a particular frequency f_0 . It shows how amplitude and phase response are changing over time for that particular frequency. Similarly, $S(\tau_0, f)$ is termed as the local spectrum at time τ_0 .

2.7.2 Computation of ST in Frequency Domain

The ST can be considered as a convolution of two functions [104] as

$$S(\tau, f) = a(\tau, f) * b(\tau, f) \quad (2.21)$$

or,

$$S(\tau, f) = \int_{-\infty}^{\infty} b(\tau - t, f) a(t, f) dt \quad (2.22)$$

where,

$$a(\tau, f) = x(\tau) e^{(-i2\pi f\tau)} \quad (2.23)$$

and

$$b(\tau, f) = \frac{|f|}{\sqrt{2\pi}} e^{-\frac{\tau^2 f^2}{2}} \quad (2.24)$$

Therefore,

$$K(\alpha, f) = A(\alpha, f) B(\alpha, f) \quad (2.25)$$

where $K(\alpha, f)$, $A(\alpha, f)$ and $B(\alpha, f)$ are the FT ($\tau \rightarrow \alpha$) of $S(\tau, f)$, $a(\tau, f)$ and $b(\tau, f)$, respectively. $K(\alpha, f)$ can be represented as

$$K(\alpha, f) = X(\alpha + f) e^{-\frac{2\pi^2 \alpha^2}{f^2}} \quad (2.26)$$

S-transform can be derived by inverse FT of $K(\alpha, f)$ as

$$S(\tau, f) = \int_{-\infty}^{\infty} X(\alpha + f) e^{-\frac{2\pi^2 \alpha^2}{f^2}} e^{i2\pi \alpha \tau} d\alpha \quad (2.27)$$

2.7.3 Discrete ST

In frequency domain computation of discrete ST (DST), fast FT (FFT) and inverse FFT (IFFT) can be applied which facilitate the computation. The equivalent frequency domain definition of the DST (letting $\tau \rightarrow lT$ and $f \rightarrow \frac{n}{NT}$, T : sampling time, N : length of the discrete signal, $X[\frac{n}{NT}]$: FFT of time series $x[mT]$, $m = -N/2, \dots, N/2 - 1$) is

$$S[l, n] = \begin{cases} \sum_{k=-N/2}^{N/2-1} X[k+n] W[k, n] e^{\frac{i2\pi kl}{N}}, & n \neq 0 \\ \frac{1}{N} \sum_{m=-N/2}^{N/2-1} x[mT], & n = 0 \end{cases} \quad (2.28)$$

where $l, n = 0, \dots, N-1$. In DST, the window function is defined as $W[k, n] = e^{-\frac{2\pi^2 k^2}{n^2}}$, where $W[k, n]$ is the sampled and truncated version of FFT of $w(\tau, f)$ which leads to inconsistency in time and frequency domain computation of ST.

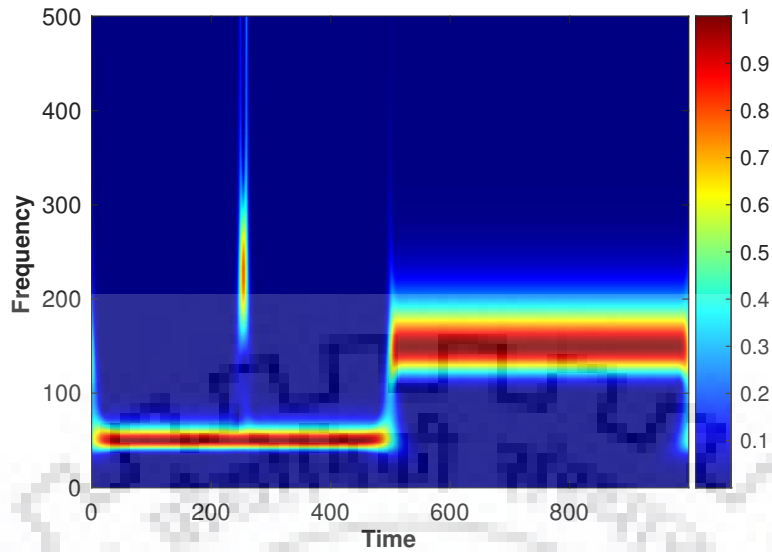


Fig. 2.8: Amplitude spectrum of the ST of sinusoidal time series as shown in Fig. 2.3(a)

Fig. 2.8 shows the amplitude spectrum of ST of the time series shown in Fig. 2.3(a). It can be easily observed that the high frequency bursts are properly resolved. Thus, the ST overcomes the drawbacks of STFT.

2.7.4 Limitations of ST

In an ideal case, the TFR should show the correct spectral information of a signal at correct time instants without cross-information about adjacent instants [33]. The main objective of TFA is to have a highly energy concentrated TFR as close as possible to an ideal TFR [34]. The conventional ST uses a GW whose width varies inversely proportional to frequency. This scaling criterion provides very large window width at lower frequencies and very short window width at higher frequencies, and thus leads to unnecessary deterioration in time and frequency resolution at lower and higher frequencies, respectively. To improve the energy concentration, several variants of ST have been proposed. The existing variants either modify the scaling criterion or use a window function other than a GW.

2.8 Existing Scaling Criteria for ST

2.8.1 Conventional Linear Scaling

To provide MRA in DST, a scalable GW is used. The width of the GW is scaled by varying the SD. For comparison purpose, the SD of the GW in time and frequency domains are denoted as σ_T and σ_f , respectively. In conventional DST [9], the SD of the GW in time

domain is inversely proportional to frequency as

$$\sigma_T = \frac{N}{n} \quad (2.29)$$

The time domain width (σ_T) of the GW decreases monotonically with increase in frequency (n). Thus, better time localization is obtained at higher frequencies, and better frequency localization at lower frequencies. The SD of the GW in frequency domain is directly proportional to frequency as

$$\sigma_F = \frac{n}{2\pi} \quad (2.30)$$

The window width affects the time and frequency domain resolution. Narrower the window in time domain, better will be the time resolution.

The drawback of the conventional linear scaling (CLS) [9] defined in (2.29) and (2.30) is that it provides an unfair trade-off between time and frequency domain width of the window, and thus leads to unfair time and frequency resolution in the TFR. The frequency domain window width linearly increases with increase in frequency, which leads to very large window width at higher frequencies. Inversely, the window width in time domain decreases hyperbolically, which leads to very wide windows at lower frequencies and very narrow windows at higher frequencies. Thus, it can be inferred that the CLS is highly biased, and leads to deterioration of frequency resolution for a broad range of frequencies, and has very poor time resolution at low frequencies.

2.8.2 Modified Linear Scaling

To overcome the aforementioned problems, the SD of the GW is scaled by a factor k [20]. For $k > 1$, the kernel of DST includes more than one modulated sine and cosine cycle, which leads to improved frequency resolution. In this scaling criterion, σ_T and σ_F are selected as

$$\sigma_T = \frac{kN}{n} \quad (2.31)$$

and

$$\sigma_F = \frac{n}{2\pi k} \quad (2.32)$$

For $k > 1$, the σ_F is divided by the factor k at each frequency, and hence frequency resolution improves as compared to CLS. However, σ_t is multiplied by the same factor k which leads to more degradation in time resolution at lower frequencies. Similar to CLS, the profile of σ_F in this approach is linear, but only divided by the factor k . Thus, for convenience, this scaling approach is referred as modified linear scaling (MLS). Fig. 2.9

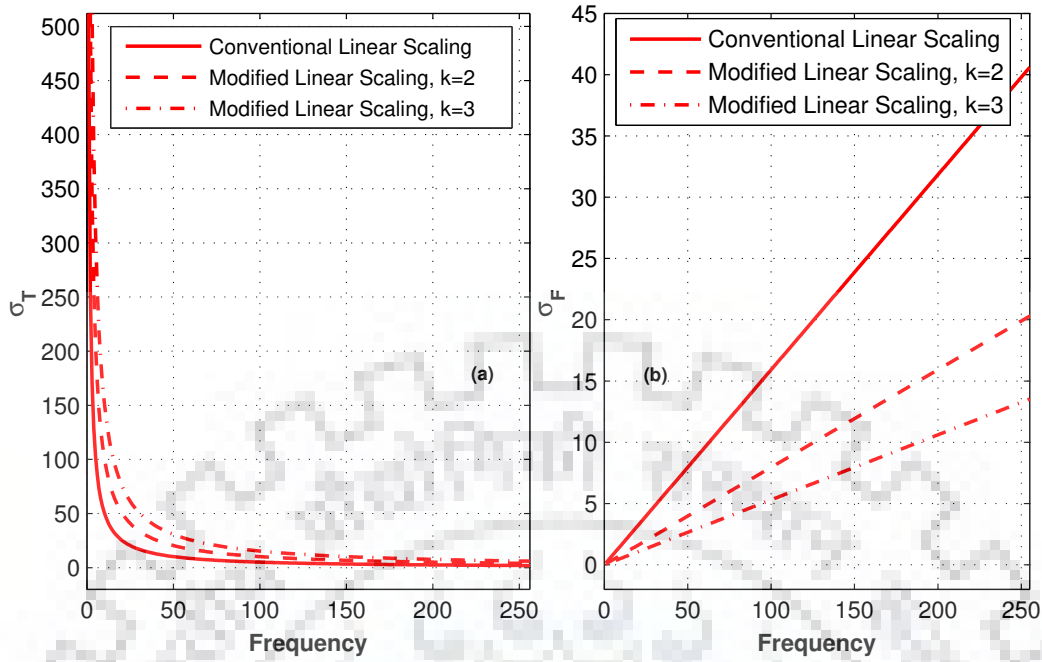


Fig. 2.9: Comparison between CLS and MLS: SD of GW for length $N = 512$ in (a) Time domain; (b) Frequency domain

shows the variation of σ_T and σ_F with frequency for CLS ($k = 1$) and MLS for $k = 2$ and $k = 3$. As compared to CLS, MLS improves frequency resolution but at the cost of degradation of the time domain resolution at lower frequencies.

2.8.3 Power Scaling

A scaling criterion presented in [39] varies the width of the window exponentially by introducing a parameter p , ($p < 1$) as an exponent of analysis frequency. σ_T and σ_F are chosen as

$$\sigma_T = N/n^p \quad (2.33)$$

and

$$\sigma_F = n^p / (2\pi) \quad (2.34)$$

For $p < 1$, the frequency resolution improves as compared to CLS. σ_T follows an exponential decay as compared to the hyperbolic decay in CLS. This leads to more deteriorated time resolution at lower frequencies as compared to CLS. Fig. 2.10 shows the variation of σ_T and σ_F for different values of p . In this scaling, the window width varies as a power function of frequency, and thus it is referred as power scaling (PS) hereafter. As compared to MLS, PS provides a small curvature in the σ_T profile as shown in Fig. 2.10. However, the deterioration in frequency resolution at higher frequencies and time resolution at lower frequencies is approximately similar as that of the MLS due to approximately

linear profile of σ_F and σ_T in these frequency regions, respectively.

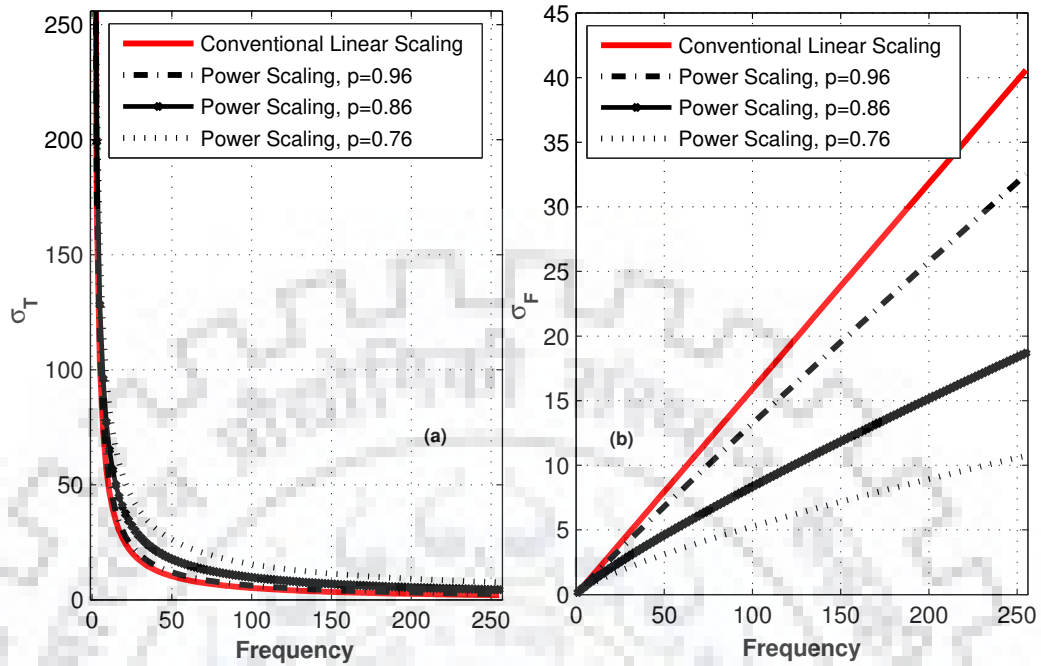


Fig. 2.10: Comparison between CLS and PS: SD of GW for length $N = 512$ in (a) Time domain; (b) Frequency domain

2.8.4 Sigmoid Scaling

In [105], the window width profile is changed by varying the window width with frequency as a sigmoid function. The sigmoid function causes saturation of the window width after a certain frequency. The improved frequency localization is obtained by avoiding unnecessary deterioration in frequency resolution at higher frequencies. However, saturation of the window width causes two major drawbacks as in STFT. If the width gets saturated to a large value, it provides poor frequency resolution for entire range of frequencies starting from saturation point. If it gets saturated to a lower value, a high-frequency burst can not be detected. The frequencies higher than the frequency at which the widths of the window get saturated, can never get detected. This scaling is referred as sigmoid scaling (SS). The window width in time and frequency domain are chosen as

$$\sigma_T = \frac{1}{a_1 \operatorname{erf}\left(\frac{b_1 r}{N}\right)}, \quad \sigma_F = \frac{N}{2\pi} a_1 \operatorname{erf}\left(\frac{b_1 r}{N}\right) \quad (2.35)$$

where $\operatorname{erf}(\cdot)$ represents the Gaussian error function, and a_1 and b_1 are window width parameters. The time and frequency domain window width profiles are shown in Fig.

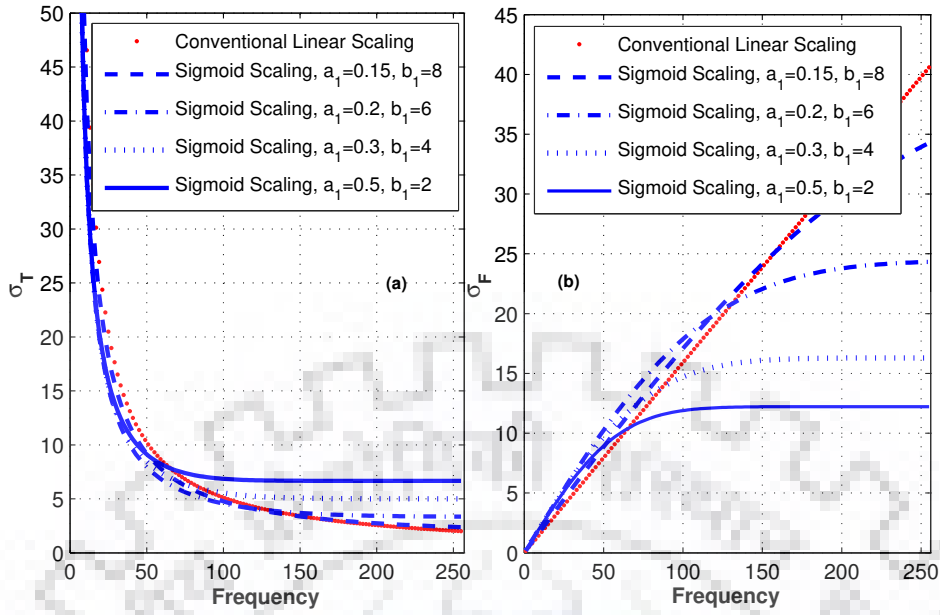


Fig. 2.11: Comparison between CLS and SS: SD of GW for length $N = 512$ in (a) Time domain; (b) Frequency domain

2.11(a) and 2.11(b), respectively. The window width tends towards a saturated profile for most of the frequencies with increasing value of a_1 and decreasing value of b_1 .

For improving the time-frequency resolution in TFR, various combinations of MLS and PS have also been introduced such as three parameter scaling (3PS) [106] and four parameters scaling (4PS) [13]. The optimum value of these parameters are chosen so as to maximize the over all CM of TFR. Three or more parameters based approaches are often very complex since there is no closed form dependence of the energy concentration of TFR on introduced parameters, hence rely on brute force search over parameter grid. It results in evaluation of huge number of TFRs. Thus adding more parameters and optimizing those using CM or heuristic algorithms are very tedious and computationally complex task.

2.9 Existing Windows for ST

2.9.1 Symmetrical Windows

Gaussian Window (GW)

The scalable GW used in conventional ST which can be represented as

$$w(t, f) = \frac{1}{\sqrt{2\pi}\sigma(f)} \exp\left(\frac{-t^2}{2\sigma^2(f)}\right) \quad (2.36)$$

where the scaling parameter $\sigma(f) = 1/f$.

Adaptive Dolph Chebyshev Window

Instead of using a GW as the kernel of ST, other window functions can also be used depending on the application. An adaptive Dolph Chebyshev window based ST has been proposed to improve TFR characteristics for certain class of signals [43]. The adaptive Dolph Chebyshev window can be represented as

$$w_{DC}(n, f) = \frac{1}{N} \left[2 \sum_{j=1}^{N/2} T_{N-1}(k_0 \cos(i\pi/N)) \cos(i2n\pi/N) + \frac{1}{r} \right] \quad (2.37)$$

where

$$k_0 = \cosh \left(\frac{1}{N} - \cosh^{-1}(1/r) \right) \quad (2.38)$$

The function $T_n(k)$ denotes Chebyshev polynomial of order k which can be represented as

$$T_n(l) = \begin{cases} \cos(n \cos^{-1}(l)), & |l| < 1 \\ \cosh(n \cos^{-1}(l)), & |l| \geq 1 \end{cases} \quad (2.39)$$

$r(f)$ denotes the frequency dependent ripple ratio which can be represented as

$$r(f) = \frac{kf^p + m}{\eta} \quad (2.40)$$

where the parameters k , p , m and η are chosen so as to maximize the overall CM. In adaptive Dolph Chebyshev window, the main lobe width can be decreased by increasing $r(f)$. This window has same height of the side lobes at each frequency.

2.9.2 Asymmetrical Windows

Bi-Gaussian Window (BGW)

The asymmetrical BGW is proposed for accurate detection of arrival and termination times of seismic events [59, 107]. The two half GWs with different SDs are welded to provide asymmetry. The asymmetrical BGW can be represented as

$$w_{BG}(t, f) = \frac{|f|}{\sqrt{2\pi}} \left(\frac{2}{\sigma_{BG}^B + \sigma_{BG}^F} \right) \exp \left(\frac{-f^2 t^2}{2(\tilde{\sigma}_{BG}(t))^2} \right) \quad (2.41)$$

where

$$\tilde{\sigma}_{BG}(t) = \begin{cases} \sigma_{BG}^B, & t \geq 0 \\ \sigma_{BG}^F, & t < 0 \end{cases}$$

σ_{BG}^B and σ_{BG}^F represent front and back taper parameters of front and back half GWs, respectively. If σ_{BG}^F is replaced by $\sigma_{BG}^F + (\sigma_{BG} - \sigma_{BG}^F)(f/f_L)$, the frequency dependent asymmetry can be achieved. σ_{BG} is analogous to total width parameter of BGW, and f_L represents the highest frequency being considered for computing the BGW based ST.

Hyperbolic Window (HW)

The HW is proposed for accurate identification of primary (p) and secondary (s) seismic wave arrival in noisy seismogram [42]. The HW can be represented as

$$w_{HY}(t, f) = \frac{|f|}{\sqrt{2\pi}} \left(\frac{2}{\sigma_{HY}^B + \sigma_{HY}^F} \right) \exp \left(\frac{-f^2 X^2(t, \sigma_{HY}^F, \sigma_{HY}^B, \lambda_{HY}^2)}{2} \right) \quad (2.42)$$

where

$$X(t, \sigma_{HY}^F, \sigma_{HY}^B, \lambda_{HY}^2) = \left(\frac{\sigma_{HY}^B + \sigma_{HY}^F}{2\sigma_{HY}^B \sigma_{HY}^F} \right) (t - \xi) + \left(\frac{\sigma_{HY}^B - \sigma_{HY}^F}{2\sigma_{HY}^B \sigma_{HY}^F} \right) \sqrt{(t - \xi)^2 + \lambda_{HY}^2} \quad (2.43)$$

where σ_{HY}^F ($0 < \sigma_{HY}^F < \sigma_{HY}^B$) denotes the forward taper parameter. The backward taper parameter is represented by σ_{HY}^B . λ_{HY} denotes the positive curvature parameter. ξ is introduced to shift the peak of w_{HY} at $t = 0$. The translation parameter ξ can be denoted as

$$\xi = \sqrt{\frac{(\sigma_{HY}^B - \sigma_{HY}^F)^2 \lambda_{HY}^2}{4\sigma_{HY}^B \sigma_{HY}^F}} \quad (2.44)$$

2.10 Existing Post Processing Tools for ST

The classical TFA tools and their variants suffer from low time-frequency resolution due to the Heisenberg uncertainty principle or unwanted cross terms. It may lead to unreliable characterization of the nonlinear behavior of nonstationary signals. In recent years, some advanced post processing methods have been proposed for TFA, such as the RM [45, 46] and SST [47, 48]. These tools have the ability to reassign or squeeze the TFR coefficients obtained by classical TFA methods into the IF and time trajectory [50].

2.10.1 ST combined with SST

The generalized form of ST (GST) of a continuous signal $x(t)$ can be represented as follows [9]

$$S^w(\tau, f) = \int_{-\infty}^{\infty} x(t)w(\tau - t, f)e^{-i2\pi ft} dt \quad (2.45)$$

The window satisfies a normalization condition

$$\int_{-\infty}^{\infty} w(t, f)dt = 1 \quad (2.46)$$

Using the convolution property, the computation of GST in frequency domain is as follows,

$$S^w(\tau, f) = \int_{-\infty}^{\infty} X(\alpha + f)W(\alpha, f)e^{i2\pi\alpha\tau} d\alpha \quad (2.47)$$

where $X(\alpha)$ and $W(\alpha, f)$ represent FT of $x(t)$ and $w(t, f)$ respectively. In conventional ST, $w(t, f)$ represents a GW defined in (2.36).

The SST reassigns the TFR coefficients into IF trajectory. To derive the IF, let's consider a monocomponent (\hat{f}) signal with fixed amplitude A as

$$x(t) = Ae^{i2\pi\hat{f}t} \quad (2.48)$$

The FT of the signal can be represented as

$$X(\alpha) = A\delta(\alpha - \hat{f}) \quad (2.49)$$

where $\delta(\cdot)$ represents dirac function. Using (2.49), (2.47) can be represented as

$$S^w(\tau, f) = AW(\hat{f} - f, f)e^{i2\pi(\hat{f}-f)\tau} \quad (2.50)$$

To obtain the IF, it is suggested to calculate the derivative of the TFR with respect to time. Let's take the derivative of ST as

$$\partial_{\tau}(S^w(\tau, f)) = i2\pi(\hat{f} - f)S^w(\tau, f) \quad (2.51)$$

where $\partial_t(x)$ represents partial derivative of x with respect to t . Therefore,

$$\hat{f} = f - i\frac{\partial_{\tau}(S^w(\tau, f))}{2\pi S^w(\tau, f)} \quad (2.52)$$

Using (2.45), $\partial_\tau(S^w(\tau, f))$ can be represented as

$$\begin{aligned}\partial_\tau(S^w(\tau, f)) &= \partial_\tau \left(\int_{-\infty}^{\infty} x(t)w(\tau - t, f)e^{-i2\pi ft} dt \right) \\ &= \int_{-\infty}^{\infty} x(t)\partial_\tau(w(\tau - t, f))e^{-i2\pi ft} dt \\ &= S^{w'}(\tau, f)\end{aligned}\tag{2.53}$$

where $S^{w'}(\tau, f)$ represents the ST obtained using derivative of $w(t, f)$. By using (2.53), the IF in (2.52) can be redefined as

$$\hat{f} = f - \Im \left(\frac{S^{w'}(\tau, f)}{2\pi S^w(\tau, f)} \right)\tag{2.54}$$

where $\Im(Z)$ represents the imaginary part of Z . The ST combined with SST at any frequency (f_0) can be represented as

$$SSST(\tau, f_0) = \int_{-\infty}^{\infty} S^w(\tau, f)\delta(f_0 - \hat{f})df\tag{2.55}$$

2.10.2 ST combined with RM

The RM reassigns the TFR coefficients to the IF trajectory in both time and frequency domain *i.e.* RM reassigns the TFR coefficients to the instantaneous time or group delay (GD) along with IF. To derive GD, let's consider a signal having one impulse as

$$x(t) = A \delta(t - \hat{\tau})\tag{2.56}$$

By considering time domain computation of ST (2.45), $S^w(\tau, f)$ for this signal can be represented as

$$S^w(\tau, f) = A w(\tau - \hat{\tau}, f)e^{-i2\pi f\hat{\tau}}\tag{2.57}$$

For GD, derivative of $S^w(\tau, f)$ with respect to frequency can be represented as

$$\begin{aligned}\partial_f(S^w(\tau, f)) &= Aw'(\tau - \hat{\tau}, f)e^{-i2\pi f\hat{\tau}} - (\hat{\tau}i2\pi)Aw(\tau - \hat{\tau}, f)e^{-i2\pi f\hat{\tau}} \\ &= S^{w'}(\tau, f) - (\hat{\tau}i2\pi)S^w(\tau, f)\end{aligned}\tag{2.58}$$

Therefore,

$$\hat{\tau} = \frac{S^{w'}(\tau, f)}{i2\pi S^w(\tau, f)} - \frac{\partial_f(S^w(\tau, f))}{i2\pi S^w(\tau, f)}\tag{2.59}$$

Using (2.45), $\partial_f(S(\tau, f))$ can be represented as

$$\begin{aligned}
 \partial_f(S^w(\tau, f)) &= \partial_f \left(\int_{-\infty}^{\infty} x(t) e^{-i2\pi ft} w(\tau - t, f) dt \right) \\
 &= \int_{-\infty}^{\infty} x(t) \partial_f e^{-i2\pi ft} (w(\tau - t, f)) dt \\
 &= \int_{-\infty}^{\infty} x(t) \partial_f (w(\tau - t, f)) e^{-i2\pi ft} dt - i2\pi \int_{-\infty}^{\infty} x(t) t w(\tau - t, f) e^{-i2\pi ft} dt \\
 &= S^{w'}(\tau, f) - i2\pi \int_{-\infty}^{\infty} x(t) (t - \tau) w(\tau - t, f) e^{-i2\pi ft} dt \\
 &\quad - i2\pi \tau \int_{-\infty}^{\infty} x(t) w(\tau - t, f) e^{-i2\pi ft} dt \\
 &= S^{w'}(\tau, f) - i2\pi S^{(tw)}(\tau, f) - i2\pi \tau S^w(\tau, f)
 \end{aligned} \tag{2.60}$$

By using (2.60), GD in (2.59) can be redefined as

$$\hat{\tau} = \tau + \Re \left(\frac{S^{tw}(\tau, f)}{S^w(\tau, f)} \right) \tag{2.61}$$

RM reassigns the TFR coefficients to coordinate $(\hat{\tau}, \hat{f})$ rather than to the point (τ, f) where it is computed. The value of the ST combined with RM at any point (τ_0, f_0) can be represented as

$$RST(\tau_0, f_0) = \int_{-\infty}^{\infty} \int_{-\infty}^{\infty} S^w(\tau, f) \delta(\tau_0 - \hat{\tau}) \delta(f_0 - \hat{f}) d\tau df \tag{2.62}$$

2.11 Concluding Remarks

This chapter provided an insight into the commonly used linear TFA tools. A brief introduction on conventional ST followed by a description on its variants improving the energy concentration in TFR has been presented. The ability of post processing tools, namely RM and SST to squeeze the spread energy in TFR of ST and reassign it to IF trajectory has been discussed.



Chapter 3

ST based on Optimally Concentrated Time-limited and Band-limited Windows

3.1 Introduction

Improving the energy concentration in time-frequency domain remains a major challenge in ST. Choosing a time-limited narrow window is beneficial for precisely resolving spectral components in time. Similarly, a band-limited window can provide improved resolvability in frequency domain. However, limiting an arbitrary window in one domain results in unwanted spreading in other domain. To this extent, two discrete time-limited and band-limited optimal windows with minimum spreading in other respective domain are designed in this chapter. By extending the concept of optimal windows, two variants of ST, namely TST and BST are proposed. The proposed variants of ST are particularly beneficial for the applications where a very precise resolution is desired in either time or frequency domain. TST can potentially be helpful in precise detection of event initiation and termination, and total duration of event such as duration of heart rate signals [52], p and s wave arrival and termination in seismology [41, 42, 53, 54], etc. Similarly, BST can also have wide applicability in many applications, such as optimal window design for analysis of band-limited EEG signals [55], optimal basis design for band-limited signal [108], etc.

Time-limited and band-limited windows with optimal concentration in other respective domain are well-studied under the family of prolate spheroidal wave functions (PSWFs) [56, 109]. In particular, the zeroth order time-limited PSWF offers maximum frequency domain energy concentration. The zeroth order band-limited PSWF provides maximum time domain energy concentration [109]. Their discrete counterparts are addressed as

time-limited and band-limited DPSSs [57] in discrete time continuous frequency domain, and time-limited and band-limited periodic DPSS (PDPSS) in discrete time discrete frequency domain [110,111]. In this chapter, for ease of understanding, zeroth order PDPSS is derived using an optimization approach, and some of the associated properties are discussed.

3.2 Time-limited and Band-limited Windows

3.2.1 Problem Formulation for Time-limited Window

The aim is to design a window which is limited in time interval M , and maximizes the energy concentration in frequency interval L . Consider a time-limited window \mathbf{w} of length M as

$$\mathbf{w} = \left(w[-\lfloor M/2 \rfloor], w[-\lfloor M/2 \rfloor + 1], \dots, w[\lfloor M/2 \rfloor - 1] \right)^T \quad (3.1)$$

The N -point FFT of \mathbf{w} can be represented in matrix form as

$$W[k] = \frac{1}{\sqrt{N}} \mathbf{w}^T \mathbf{d}[k] \quad (3.2)$$

where

$$\mathbf{d}[k] = \left(e^{-\frac{i2\pi k[-\lfloor M/2 \rfloor]}{N}}, e^{-\frac{i2\pi k[-\lfloor M/2 \rfloor + 1]}{N}}, \dots, e^{-\frac{i2\pi k[\lfloor M/2 \rfloor - 1]}{N}} \right)^T \quad (3.3)$$

The energy concentration in frequency domain (β^2) in a given normalized frequency interval L , where $L < N$, can be defined as

$$\beta^2 = \frac{\sum_{k=-\lfloor L/2 \rfloor}^{\lfloor L/2 \rfloor - 1} |W[k]|^2}{\sum_{k=-\lfloor N/2 \rfloor}^{\lfloor N/2 \rfloor - 1} |W[k]|^2} \quad (3.4)$$

By using (3.2), the numerator in RHS of (3.4) can be rephrased as

$$\begin{aligned} \sum_{k=-\lfloor L/2 \rfloor}^{\lfloor L/2 \rfloor - 1} |W[k]|^2 &= \frac{1}{N} \sum_{k=-\lfloor L/2 \rfloor}^{\lfloor L/2 \rfloor - 1} |\mathbf{w}^T \mathbf{d}[k]|^2 \\ &= \frac{1}{N} \mathbf{w}^H \mathbf{F}^{(M,L)} \mathbf{w} \end{aligned} \quad (3.5)$$

where $\mathbf{F}^{(M,L)} = \sum_{k=-\lfloor L/2 \rfloor}^{\lfloor L/2 \rfloor - 1} \mathbf{d}^*[k] \mathbf{d}^T[k]$ is an $M \times M$ positive semi-definite matrix. The superscript in \mathbf{d}^* represents complex conjugate of \mathbf{d} . The $(m, n)^{th}$ element of the matrix

$\mathbf{F}^{(M,L)}$ is given by

$$\begin{aligned} [\mathbf{F}^{(M,L)}]_{m,n} &= \sum_{k=-\lfloor L/2 \rfloor}^{\lfloor L/2 \rfloor - 1} e^{-i2\pi k(-\lfloor M/2 \rfloor + m - 1)/N} e^{i2\pi k(-\lfloor M/2 \rfloor + n - 1)/N} \\ &= \begin{cases} \frac{1}{N} \left(e^{i2\pi(m-n)/N} \left(\frac{L}{2} - \lfloor \frac{L}{2} \rfloor - \frac{1}{2} \right) \frac{\sin((m-n)(L\pi/N))}{\sin((m-n)(\pi/N))} \right), & m \neq n \\ \frac{L}{N}, & m = n \end{cases} \end{aligned} \quad (3.6)$$

At $L = N$, $\mathbf{F}^{(M,L)}$ becomes an identity matrix of dimension $M \times M$. The frequency concentration β^2 can be represented as

$$\beta^2 = \frac{\mathbf{w}^H \mathbf{F}^{(M,L)} \mathbf{w}}{\mathbf{w}^H \mathbf{w}} \quad (3.7)$$

The problem of maximization of β^2 can be defined as

$$\begin{aligned} \max_{\mathbf{w}} \quad & \mathbf{w}^H \mathbf{F}^{(M,L)} \mathbf{w} \\ \text{subject to} \quad & \mathbf{w}^H \mathbf{w} = 1 \end{aligned} \quad (3.8)$$

The solution to the problem defined in (3.8) is the eigenvector of matrix $\mathbf{F}^{(M,L)}$ corresponding to highest eigenvalue. Thus, eigenvalue equation can be defined as

$$\mathbf{F}^{(M,L)} \mathbf{w}_{\text{TL}}^{(M,L)} = \lambda_{\text{TL}} \mathbf{w}_{\text{TL}}^{(M,L)} \quad (3.9)$$

where $\mathbf{w}_{\text{TL}}^{(M,L)}$ is the eigenvector corresponding to highest eigenvalue λ_{TL} . The eigenvector, $\mathbf{w}_{\text{TL}}^{(M,L)}$, is the desired time-limited window which is limited to M samples, and maximizes the frequency domain energy concentration in L samples in frequency domain.

3.2.2 Problem Formulation for Band-limited Window

The aim is to design a window which is limited in frequency interval L , and maximizes the energy concentration in time interval M . Consider a band-limited window of length L as

$$\mathbf{W} = \left(W[-\lfloor L/2 \rfloor], W[-\lfloor L/2 \rfloor + 1], \dots, W[\lfloor L/2 \rfloor - 1] \right)^T \quad (3.10)$$

The N -point IFFT of \mathbf{W} can be represented in matrix form as

$$w[m] = \frac{1}{\sqrt{N}} \mathbf{W}^T \mathbf{b}[m] \quad (3.11)$$

where

$$\mathbf{b}[m] = \left(e^{\frac{i2\pi m \lfloor -L/2 \rfloor}{N}}, e^{\frac{i2\pi m \lfloor -L/2 \rfloor + 1}{N}}, \dots, e^{\frac{i2\pi m \lfloor L/2 \rfloor - 1}{N}} \right)^T \quad (3.12)$$

The time domain energy concentration (α^2) in a given time interval M , where $M < N$, can be defined as

$$\alpha^2 = \frac{\sum_{m=\lfloor -M/2 \rfloor}^{\lfloor M/2 \rfloor - 1} |w[m]|^2}{\sum_{m=\lfloor -N/2 \rfloor}^{\lfloor N/2 \rfloor - 1} |w[m]|^2} \quad (3.13)$$

By using (3.11), the numerator in RHS of (3.13) can be rephrased as

$$\begin{aligned} \sum_{m=\lfloor -M/2 \rfloor}^{\lfloor M/2 \rfloor - 1} |w[m]|^2 &= \frac{1}{N} \sum_{m=\lfloor -M/2 \rfloor}^{\lfloor M/2 \rfloor - 1} |\mathbf{W}^T \mathbf{b}[m]|^2 \\ &= \frac{1}{N} \mathbf{W}^H \mathbf{Q}^{(M,L)} \mathbf{W} \end{aligned} \quad (3.14)$$

where $\mathbf{Q}^{(M,L)} = \sum_{m=\lfloor -M/2 \rfloor}^{\lfloor M/2 \rfloor - 1} \mathbf{b}^*[m] \mathbf{b}^T[m]$ is an $L \times L$ positive semi-definite matrix. The $(k, l)^{th}$ element of the matrix $\mathbf{Q}^{(M,L)}$ is given by

$$\begin{aligned} [\mathbf{Q}^{(M,L)}]_{k,l} &= \sum_{m=\lfloor -M/2 \rfloor}^{\lfloor M/2 \rfloor - 1} e^{\frac{i2\pi m \lfloor -L/2 \rfloor + k - 1}{N}} e^{-\frac{i2\pi m \lfloor -L/2 \rfloor + l - 1}{N}} \\ &= \begin{cases} \frac{1}{N} \left(e^{\frac{i2\pi(k-l)}{N} \left(\frac{M}{2} - \lfloor \frac{M}{2} \rfloor - \frac{1}{2} \right)} \frac{\sin((k-l)(M\pi/N))}{\sin((k-l)(\pi/N))} \right), & k \neq l \\ \frac{M}{N}, & k = l \end{cases} \end{aligned} \quad (3.15)$$

At $M = N$, $\mathbf{B}^{(M,L)}$ becomes an identity matrix of dimension $L \times L$. The time domain energy concentration α^2 can be represented as

$$\alpha^2 = \frac{\mathbf{W}^H \mathbf{Q}^{(M,L)} \mathbf{W}}{\mathbf{W}^H \mathbf{W}} \quad (3.16)$$

The problem of maximization of α^2 can be defined as

$$\begin{aligned} \max_{\mathbf{W}} \quad & \mathbf{W}^H \mathbf{Q}^{(M,L)} \mathbf{W} \\ \text{subject to} \quad & \mathbf{W}^H \mathbf{W} = 1 \end{aligned} \quad (3.17)$$

The solution to the problem defined in (3.17) is the eigenvector of matrix $\mathbf{Q}^{(M,L)}$ corresponding to highest eigenvalue. Thus, eigenvalue equation can be defined as

$$\mathbf{Q}^{(M,L)} \mathbf{W}_{BL}^{(M,L)} = \lambda_{BL} \mathbf{W}_{BL}^{(M,L)} \quad (3.18)$$

where $\mathbf{W}_{BL}^{(M,L)}$ is the eigenvector corresponding to highest eigenvalue λ_{BL} . The eigenvector, $\mathbf{W}_{BL}^{(M,L)}$, is the desired band-limited window which is limited to L samples in frequency domain, and maximizes the time domain energy concentration in M samples in time domain.

3.3 Properties of Time-limited and Band-limited Windows

In this section, some characteristics of time-limited and band-limited windows are illustrated and discussed.

3.3.1 Characteristics of Time-limited window

Fig. 3.1 illustrates time-limited windows for different values of L and fixed $M = 16$. In Fig. 3.1(a), windows are shown in time domain. The corresponding frequency domain spectra are illustrated in Fig. 3.1(b). In Fig. 3.1(a), the windows are strictly limited to

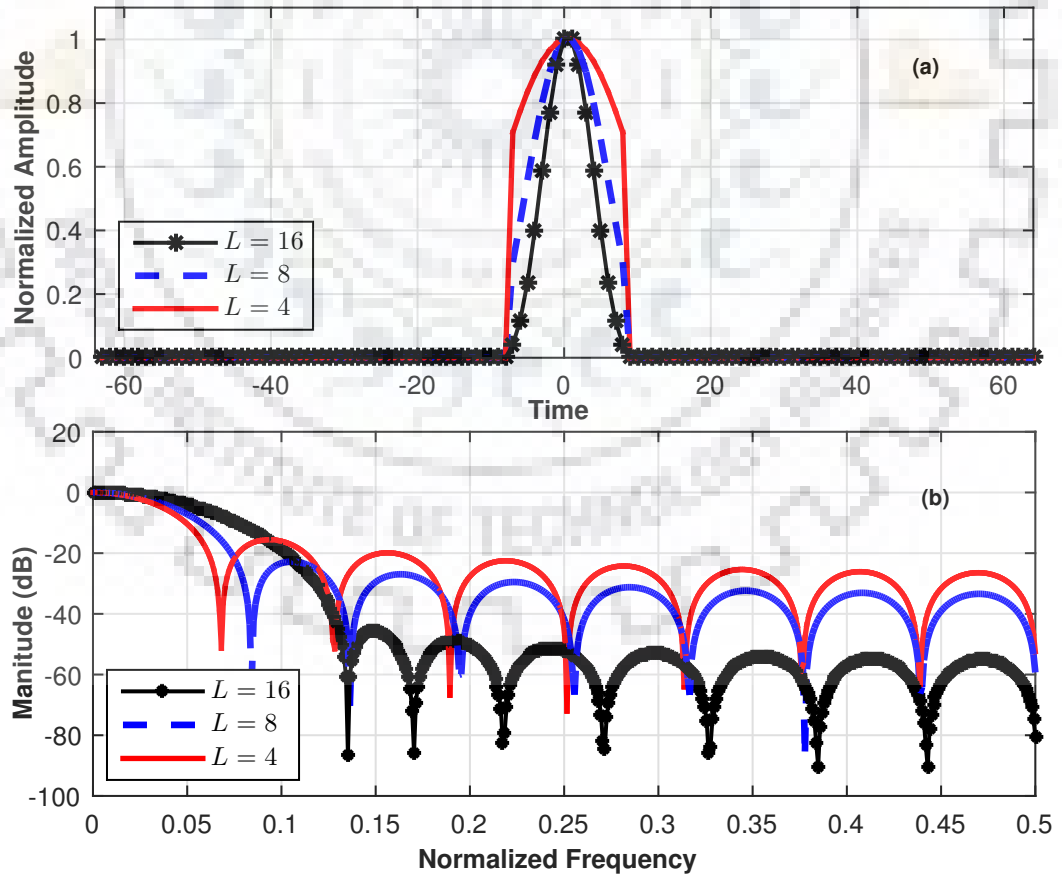


Fig. 3.1: Time-limited windows for $N = 128$, $M = 16$ and different values of L : (a) Time-limited windows in time domain; (b) The frequency domain spectra of time-limited windows

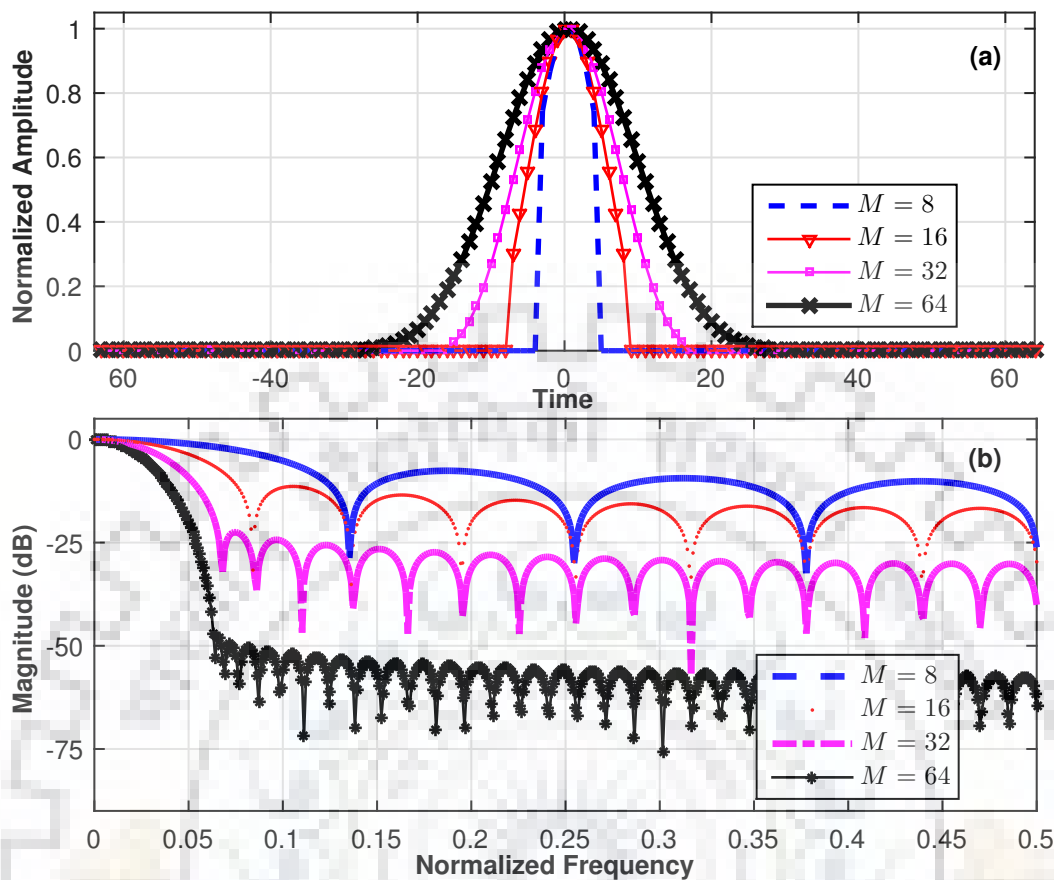


Fig. 3.2: Time-limited windows for $N = 128$, $L = 8$ and different values of M : (a) Time-limited windows in time domain; (b) The frequency domain spectra of time-limited windows

M samples, and change shape according to L . It can be observed in Fig. 3.1(b) that as L decreases, the main lobe becomes narrower at the cost of higher side lobes. Therefore, higher energy concentration in a narrow frequency interval can be achieved by either increasing M or decreasing L . The former approach results in wider window in time domain which in turn affects the time resolution in TFR. The later approach leads to higher side-lobes.

Fig. 3.2 shows time-limited windows of length $N = 128$ which are strictly confined to time interval M . Windows are plotted for different values of M and fixed $L = 8$. Windows in time domain and their corresponding frequency domain spectra are shown in Fig. 3.2(a) and Fig. 3.2(b), respectively. It can be observed that as M increases, the windows become wider in time domain, and correspondingly the energy concentration increases in normalized frequency interval L .

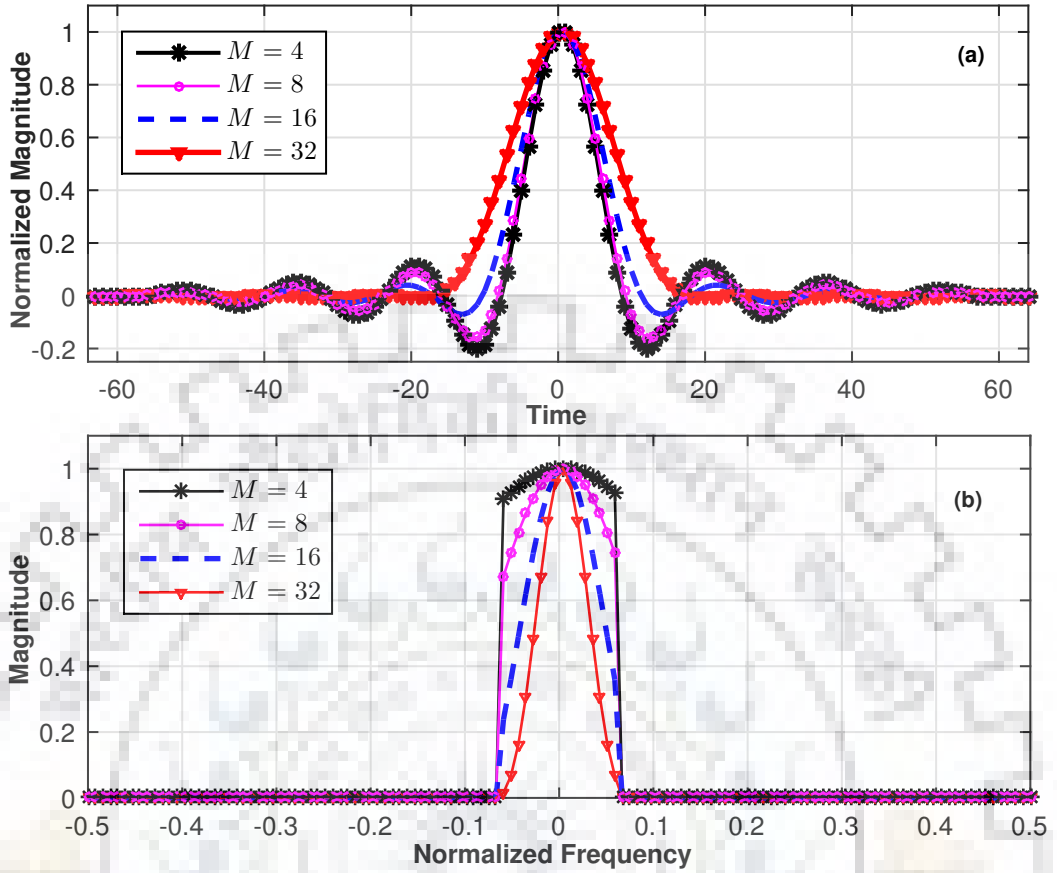


Fig. 3.3: Band-limited windows for $N = 128$, $L = 8$ and different values of M : (a) Band-limited windows in time domain; (b) The frequency domain spectra of band-limited windows

3.3.2 Characteristics of Band-limited Window

Fig. 3.3 illustrates the band-limited windows for different values of M and fixed $L = 8$. In Fig. 3.3(a), windows are shown in time domain. The corresponding frequency domain spectra are illustrated in Fig. 3.3(b). It can be observed in Fig. 3.3(b) that windows are strictly limited to $L = 8$ samples, and change shape with change in the value of M . As M increases, windows become narrower in frequency domain at the cost of higher side-lobes in time domain which is evident in Fig. 3.3(a).

In Fig. 3.4, the band-limited windows are shown for $M = 8$ and different values of L . In Fig. 3.4(a), windows are shown in time domain. The corresponding frequency domain spectra are illustrated in Fig. 3.4(b). It can be observed in Fig. 3.4(b) that the spectrum is strictly limited to L frequency samples. As L decreases, windows become narrower in frequency domain at the cost of spreading in time domain.

It can be seen that limiting the window in one domain results in spreading in other domain, and the shape of the window is characterized by L and M . Therefore, a desired

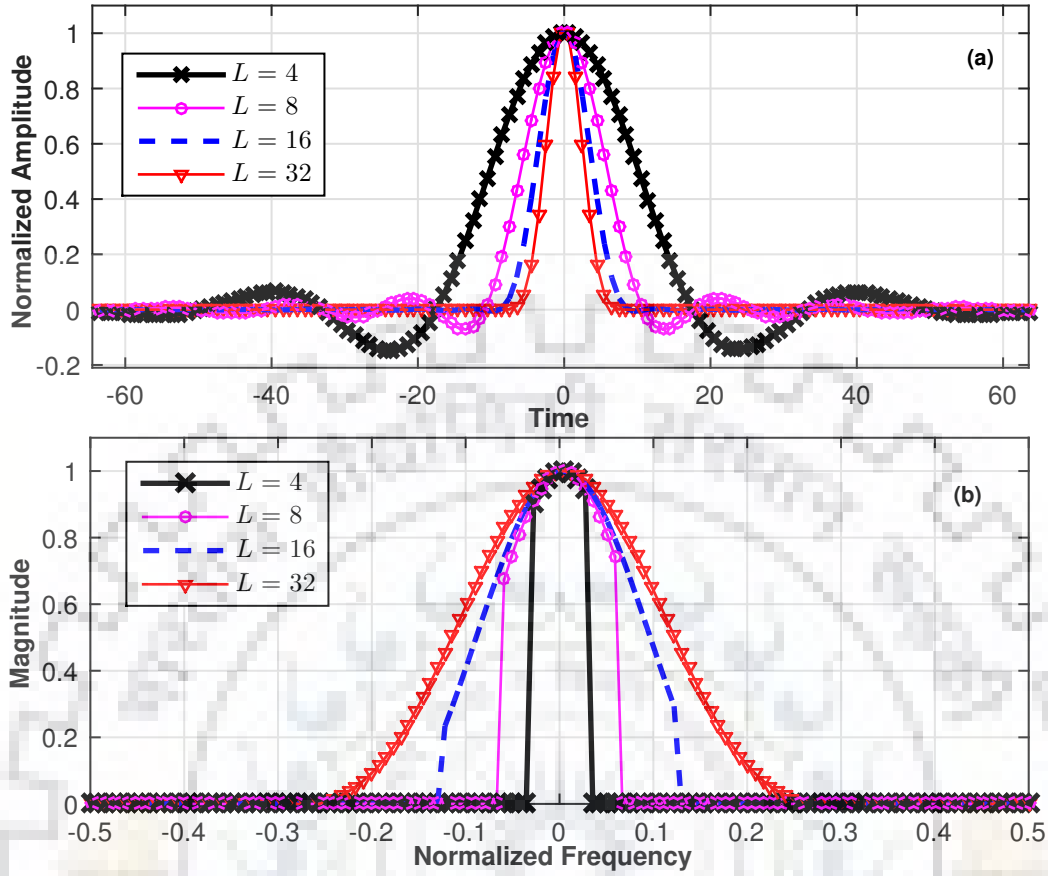


Fig. 3.4: Band-limited windows for $N = 128$, $M = 8$ and different values of L : (a) Band-limited windows in time domain; (b) The frequency domain spectra of band-limited windows

window can be chosen depending on the application by selecting appropriate values of M and L .

3.3.3 Relationship Between Time-limited and Band-limited Windows

$\mathbf{W}_{\text{BL}}^{(M,L)}$ can be obtained as the center L elements of N -point FFT of $\mathbf{w}_{\text{TL}}^{(M,L)}$, and similarly $\mathbf{w}_{\text{TL}}^{(M,L)}$ can be considered as the center M elements of N -point IFFT of $\mathbf{W}_{\text{BL}}^{(M,L)}$.

Proof: The matrix $\mathbf{F}^{(M,L)}$ in (3.5) can also be written as

$$\mathbf{F}^{(M,L)} = \mathbf{E}\mathbf{Y}^H\mathbf{Z}^T\mathbf{Z}\mathbf{Y}\mathbf{E}^T \quad (3.19)$$

where $\mathbf{E} = [\mathbf{0}_{M \times (N-M)/2} \quad \mathbf{I}_{M \times M} \quad \mathbf{0}_{M \times (N-M)/2}]$ is a matrix of dimension $M \times N$ having elements as zero for all M rows and first and last $(N - M)/2$ columns, and an identity matrix for all M rows and middle M columns. $\mathbf{0}_{p \times q}$ denotes a $p \times q$ matrix having all zero elements. \mathbf{I} denotes the identity matrix. Similarly, matrix $\mathbf{Z} = [\mathbf{0}_{L \times (N-L)/2} \quad \mathbf{I}_{L \times L} \quad \mathbf{0}_{L \times (N-L)/2}]$ is a matrix of dimension $L \times N$ having elements as

zero for all L rows and first and last $(N - L)/2$ columns, and an identity matrix for all L rows and middle L columns. The matrix \mathbf{Y} is an $(N \times N)$ Fourier matrix. The $(m, n)^{th}$ element of \mathbf{Y} can be defined as $\mathbf{Y} = (e^{-i2\pi mn/N})_{(m,n)=-N/2}^{N/2-1}$. Using the matrix \mathbf{E} , \mathbf{Y} and \mathbf{Z} , the matrix $\mathbf{Q}^{(M,L)}$ defined in (3.14) can also be written as

$$\mathbf{Q}^{(M,L)} = \mathbf{Z}\mathbf{Y}\mathbf{E}^T\mathbf{E}\mathbf{Y}^H\mathbf{Z}^T \quad (3.20)$$

Using (3.19) and (3.20), (3.9) and (3.18) can be rewritten as, respectively

$$\mathbf{G}\mathbf{G}^T\mathbf{w}_{\text{TL}}^{(M,L)} = \lambda_{\text{TL}}\mathbf{w}_{\text{TL}}^{(M,L)} \quad (3.21)$$

$$\mathbf{G}^T\mathbf{G}\mathbf{w}_{\text{BL}}^{(M,L)} = \lambda_{\text{BL}}\mathbf{w}_{\text{BL}}^{(M,L)} \quad (3.22)$$

where $\mathbf{G} = \mathbf{E}\mathbf{Y}^H\mathbf{Z}^T$. Since $\mathbf{G}\mathbf{G}^T$ and $\mathbf{G}^T\mathbf{G}$ are having same eigenvalues, therefore

$$\lambda_{\text{TL}} = \lambda_{\text{BL}} \quad (3.23)$$

Pre-multiplying (3.21) by \mathbf{G}^T leads to

$$\mathbf{G}^T\mathbf{G}\mathbf{G}^T\mathbf{w}_{\text{TL}}^{(M,L)} = \lambda_{\text{TL}}\mathbf{G}^T\mathbf{w}_{\text{TL}}^{(M,L)} \quad (3.24)$$

Equating (3.22) and (3.24) and using (3.23) leads to

$$\mathbf{w}_{\text{BL}}^{(M,L)} = \mathbf{G}^T\mathbf{w}_{\text{TL}}^{(M,L)} = \mathbf{Q}\mathbf{Y}\mathbf{E}^T\mathbf{w}_{\text{TL}}^{(M,L)} \quad (3.25)$$

Eq. (3.25) illustrates that $\mathbf{w}_{\text{BL}}^{(M,L)}$ is a band-limited version of $\mathbf{w}_{\text{TL}}^{(M,L)}$ i.e. $\mathbf{w}_{\text{BL}}^{(M,L)}$ can be obtained as the center L elements of N -point FFT of $\mathbf{w}_{\text{TL}}^{(M,L)}$. Similarly, pre-multiplying (3.22) by \mathbf{G} , and comparing with (3.22), leads to

$$\mathbf{w}_{\text{TL}}^{(M,L)} = \mathbf{G}\mathbf{w}_{\text{BL}}^{(M,L)} = \mathbf{E}\mathbf{Y}^H\mathbf{Z}^T\mathbf{w}_{\text{BL}}^{(M,L)} \quad (3.26)$$

Eq. (3.26) illustrates that $\mathbf{w}_{\text{TL}}^{(M,L)}$ is a time-limited version of $\mathbf{w}_{\text{BL}}^{(M,L)}$ i.e. $\mathbf{w}_{\text{TL}}^{(M,L)}$ can be obtained as the center M elements of N -point IFFT of $\mathbf{w}_{\text{BL}}^{(M,L)}$.

3.4 Time-limited Window based ST (TST)

ST utilizes Gaussian window which is the minimizer of the Heisenberg uncertainty principle. Therefore, one way to achieve the limited windows is to truncate the Gaussian window in the desired time or frequency domain. However, it does not guarantee optimal energy concentration in the other respective domain. In this section, fist the truncated

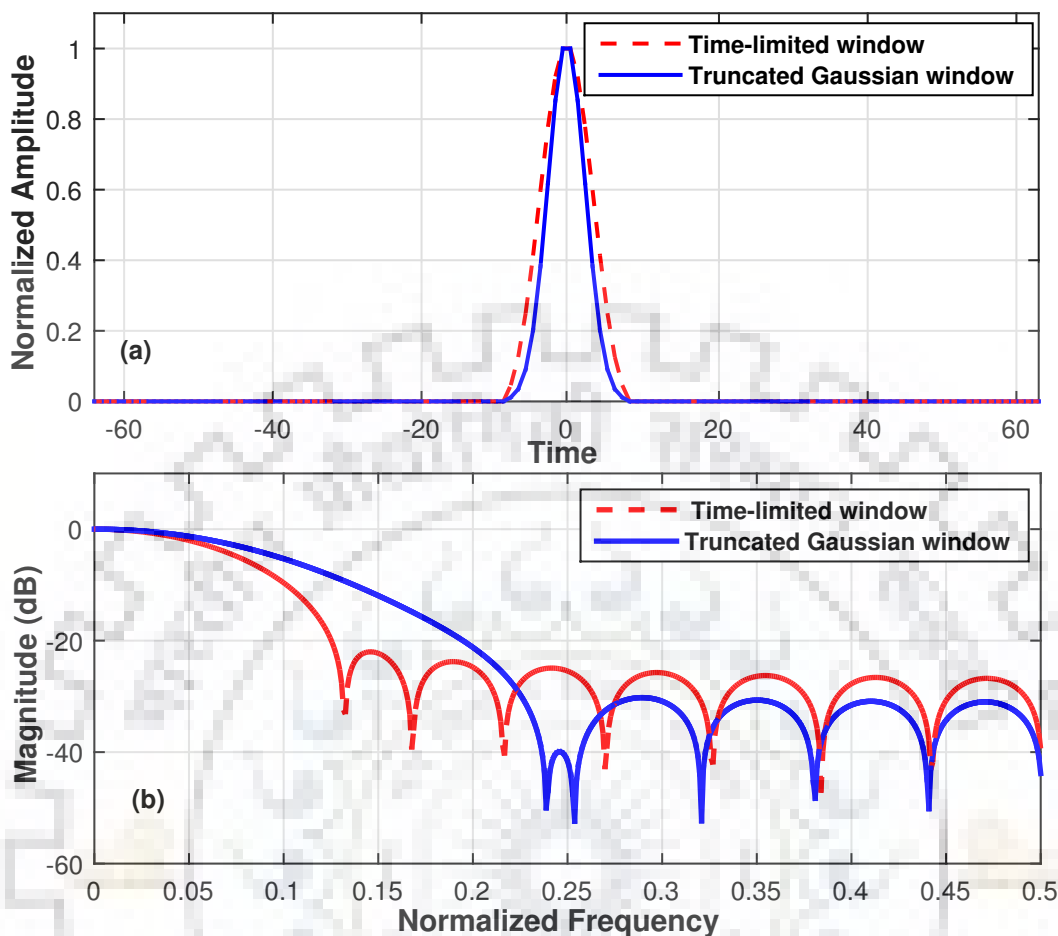


Fig. 3.5: Comparison of proposed time-limited (dashed lines) and truncated Gaussian window (solid lines) for $N = 128$, $M = 16$ and $L = 16$: (a) Windows in time domain; (b) Frequency-domain spectra

Gaussian window in time domain is compared with the presented optimal time-limited window. Afterwards, the optimal time-limited window based ST (TST) is proposed.

3.4.1 Comparison Between Time-limited Window and Truncated Gaussian Window

Fig. 3.5 compares the characteristics of time-limited and truncated Gaussian window for $M = 16$ and $L = 16$. The Gaussian window is truncated to M samples such that the support of the window is $[-2\sigma, 2\sigma]$. Windows are shown in time domain in Fig. 3.5(a), and corresponding frequency domain spectra are illustrated in Fig. 3.5(b). It can be observed that both the windows are limited to time interval of $M = 16$. However, the frequency domain characteristics indicate that the time-limited window has narrower main-lobe in frequency domain as compared to truncated Gaussian window. The time-limited window is designed to have maximum energy concentration in given normalized

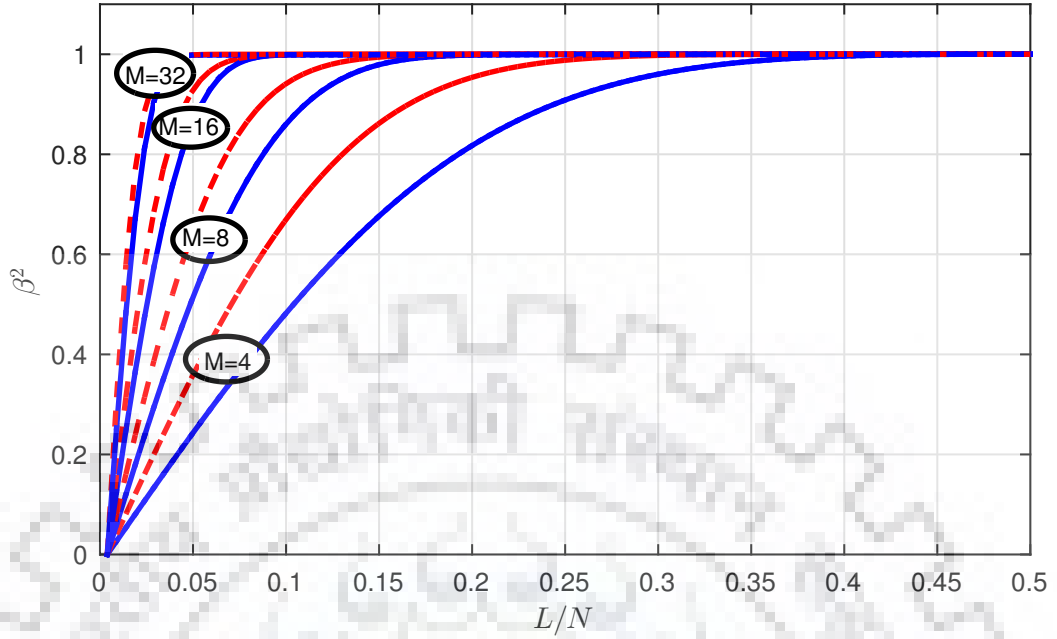


Fig. 3.6: Achievable frequency domain energy concentrations of proposed time-limited windows (dashed lines) and truncated Gaussian windows (solid lines) of length $N = 128$ for different values of M

frequency band L . However, the time-limited window has higher side-lobes as compared to truncated Gaussian window. This could be ignored in applications where maximal energy concentration in given time and frequency intervals is of primary concern.

In Fig. 3.6, the comparison between proposed time-limited window and truncated Gaussian window is drawn in terms of achievable frequency domain energy concentration (β^2). For a fixed value of M , β^2 increases with increase in L for both time-limited window and truncated Gaussian window. However, β^2 of truncated Gaussian window is lesser than that of the time-limited window, and the difference is greater for smaller time interval M . Therefore, the time window is particularly beneficial when it is desirable to confine the window in narrow time interval.

Further, to incorporate the optimal time-limited window in ST, frequency dependent normalized time-limited window is used. The time-limited window can be denoted as

$$\mathbf{w}_{\text{TL}}^{(M,L)} = (w_{\text{TL}}(-\lfloor M/2 \rfloor), w_{\text{TL}}(-\lfloor M/2 \rfloor + 1), \dots, w_{\text{TL}}(\lceil M/2 \rceil - 1))^T$$

The window is strictly limited to time interval of M samples, and maximizes the energy concentration in frequency interval of L samples. These intervals M and L are equivalent to window widths in time and frequency domains, respectively. To provide multi-resolution in TST, these intervals can be chosen as functions of frequency.

The frequency dependent normalized time-limited window can be represented as

$$v_{\text{TL}}[m, n] = \frac{\mathbf{w}_{\text{TL}}^{(M_n, L_n)}}{\sum_{m=-\lfloor M/2 \rfloor}^{\lfloor M/2 \rfloor - 1} w_{\text{TL}}[m]} \quad (3.27)$$

where subscript n in M_n and L_n represents the dependency of time and frequency intervals on frequency. The N -point FFT of (3.27) can be represented as

$$\zeta_{\text{TL}}[k, n] = \sum_{m=-\lfloor M/2 \rfloor}^{\lfloor M/2 \rfloor - 1} v_{\text{TL}}[m, n] e^{-\frac{i2\pi mk}{N}} \quad (3.28)$$

where $k = -\lfloor N/2 \rfloor, \dots, \lfloor N/2 \rfloor - 1$.

By using (3.28), the discrete TST can be represented as

$$S^{\text{vTL}}[l, n] = \begin{cases} \sum_{k=-\lfloor N/2 \rfloor}^{\lfloor N/2 \rfloor - 1} X[k+n] \zeta_{\text{TL}}[k, n] e^{i2\pi \frac{k}{N} l}, & n \neq 0 \\ \frac{1}{N} \sum_{m=-\lfloor N/2 \rfloor}^{\lfloor N/2 \rfloor - 1} x[mT], & n = 0 \end{cases} \quad (3.29)$$

where $l, n = 0, \dots, N-1$.

3.4.2 Selection of Frequency Dependent Time and Frequency Intervals in TST

The progressive resolution in the proposed TST can be obtained by either varying L_n proportional to n or varying M_n inversely proportional to n . The primary concern of TST is to provide precise resolution in time domain. Therefore, scaling in TST can be obtained by varying L_n with fixed M_n as

$$M_n = k_1, \quad L_n = k_2 n, \quad (3.30)$$

where k_1 determines the time resolution at each voice. Lesser the k_1 , better will be the time resolution. For a given k_1 , the proposed scaling in TST can precisely resolve two components separated by k_1 samples in time. The parameter k_2 defines the mode of the changing window width. For a voice n , the window maximizes the energy concentration in $k_2 n$ samples in frequency. The parameter k_1 can be chosen to satisfy the minimum desired time resolution depending on the application. The parameter k_2 is selected so as to maximize the overall concentration of TFR based on the CM [112].

3.5 Band-limited Window based ST (BST)

The band-limited window can be represented as

$$\mathbf{W}_{\text{BL}}^{(M,L)} = (W_{\text{BL}}(-\lfloor L/2 \rfloor), W_{\text{BL}}(-\lfloor L/2 \rfloor + 1), \dots, W_{\text{BL}}(\lfloor L/2 \rfloor - 1))^T$$

The band-limited window is strictly limited in frequency interval M , and maximizes the energy concentration in frequency interval L . Similar to TST, the time and frequency domain intervals can be chosen as functions of frequency to provide progressive resolution in BST. The frequency dependent band-limited normalized window can be represented as

$$\zeta_{\text{BL}}[k, n] = \frac{\mathbf{W}_{\text{BL}}^{(M_n, L_n)}}{\sum_{k=-\lfloor L/2 \rfloor}^{\lfloor L/2 \rfloor - 1} W_{\text{BL}}[k]} \quad (3.31)$$

By using (3.31), the discrete BST can be represented as

$$S^{\text{vBL}}[l, n] = \begin{cases} \sum_{k=-\lfloor N/2 \rfloor}^{\lfloor N/2 \rfloor - 1} X[k+n] \zeta_{\text{BL}}[k, n] e^{i2\pi \frac{k}{N} l}, & n \neq 0 \\ \frac{1}{N} \sum_{m=-\lfloor N/2 \rfloor}^{\lfloor N/2 \rfloor - 1} x[mT], & n = 0 \end{cases} \quad (3.32)$$

where $l, n = 0, \dots, N - 1$.

3.5.1 Selection of Frequency Dependent Time and Frequency Intervals in BST

The priority of BST is to precisely localize the signal components in frequency domain. Therefore, the scaling for BST is proposed as

$$L_n = k_3, \quad M_n = \frac{k_4 N}{n} \quad (3.33)$$

where the maximum spread in frequency is fixed for each voice and is limited to k_3 samples in frequency. The scaling is obtained by varying M_n inversely proportional to n . The value of k_3 is selected to limit the maximum spread in frequency which guarantees the resolution of two frequency components separated by k_3 samples. The optimum value of k_4 can be selected to maximize the overall CM of TFR.

3.6 Simulation Results and Discussion

In this section, the performances of proposed TST and BST are evaluated using synthetic and real signals, and compared with those of ST and its variants. ST is widely used for

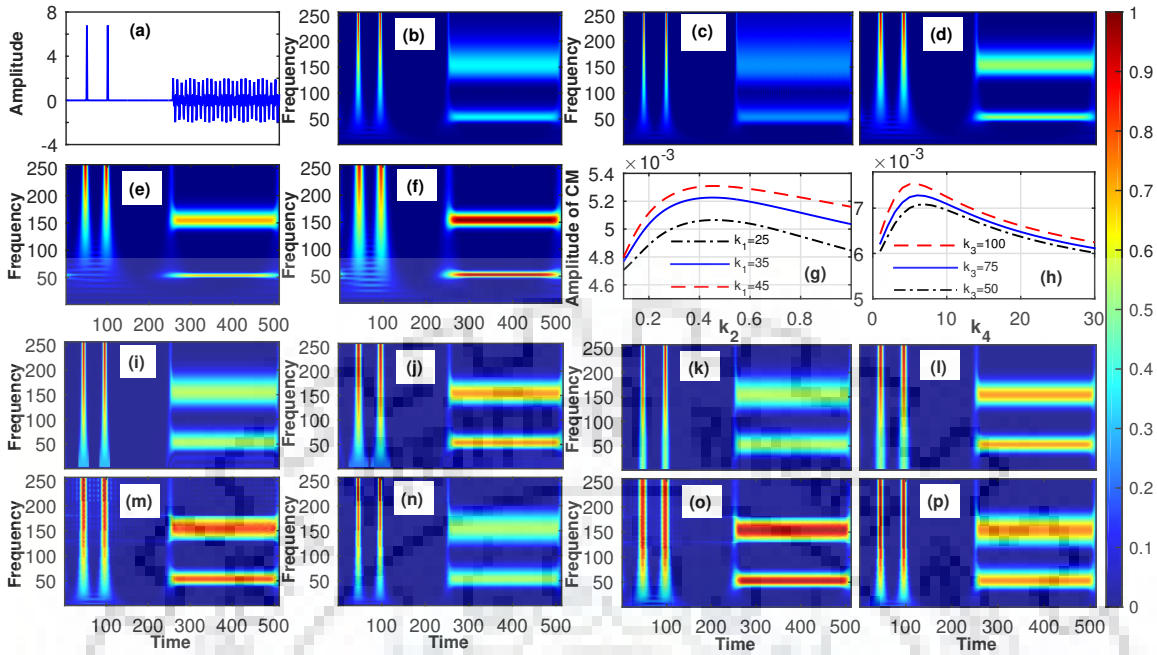


Fig. 3.7: Performance evaluation of proposed TST and BST: (a) Synthetic time series; TFR of (b) conventional ST; (c) ST with MLS for $k = 0.7$; (d) ST with MLS for $k = 2$; (e) 3PST [13]; (f) 4PST [19]; Amplitude of CM of (g) TST by varying k_2 for different values of k_1 ; (h) BST by varying k_4 for different values of k_3 ; TFR of proposed TST for (i) $k_1 = 25$, $k_2 = 0.4454$; (j) $k_1 = 45$, $k_2 = 0.4364$; TFR of proposed TST with modified scaling with $L_{th} = 5$ for (k) $k_1 = 25$, $k_2 = 0.4454$; (l) $k_1 = 45$, $k_2 = 0.4364$; TFR of proposed BST for (m) $k_3 = 50$, $k_4 = 7$; (n) $k_3 = 100$, $k_4 = 6$; TFR of proposed BST with modified scaling with $M_{th} = 5$ for (o) $k_3 = 50$, $k_4 = 7$; (p) $k_3 = 100$, $k_4 = 6$

TFA in seismology (seismic signal analysis), biomedical (ECG, EEG signal analysis) and electrical engineering (power quality disturbances analysis). The applicability of the proposed TST is investigated in seismic signal for identifying subsurface properties due to seismic wave propagation. The performance of the BST is evaluated using band-limited EEG signals for brain computer interface (BCI) applications, and also by analyzing multiple power quality disturbances.

Case Study 1: TFA of Synthetic Example

In Fig. 3.7, the normalized amplitude spectrum of proposed TST and BST are illustrated, and compared with normalized amplitude spectrum of ST and its variants using a test time series of length $N = 512$ samples. The synthetic signal, shown in Fig. 3.7(a), consists of two frequency components, 50 Hz and 150 Hz from samples 256 to 512 and two impulses at 50 and 100 time instance. It can be observed in Fig. 3.7(b) that due to its poor time resolution at lower frequencies, the conventional ST is unable to resolve the two impulses at lower frequencies. Also, the frequency resolution is very poor for

150 Hz frequency component. The time resolution in ST can be improved with MLS by decreasing k as shown in Fig. 3.7(c) for $k = 0.7$. However, it leads to more degradation in frequency resolution. The frequency resolution can be improved by increasing k at the cost of degraded time resolution as shown in Fig. 3.7(d) for $k = 2$. Fig. 3.7(e) represents the TFR of three parameters based ST (3PST) [13]. It can be observed in Fig. 3.7(e) that the frequency resolution of TFR has improved than that of ST and ST with MLS. However, the time resolution for lower frequencies has degraded. The impulses get more smeared, and time resolution for 50 Hz component is also degraded. Fig. 3.7(f) shows four parameters based ST (4PST) [19]. Both the time and frequency resolutions are better than those of 3PST. However, the impulses are still not separable. In Fig. 3.7(g), the CM of proposed TST by varying k_2 for different values of k_1 are plotted. In Fig. 3.7(h), the CM of proposed BST by varying k_3 for different values of k_4 are plotted. Figs. 3.7(i)-(l) illustrate the TFRs of the proposed TST. The proposed TST can resolve two impulses for $k_1 < 50$. In Fig 3.7(i), the TFR of the proposed TST is plotted for $k_1 = 25$. In order to maximize the overall CM of the TFR, the optimal value for parameter k_2 is found to be 0.4454. The proposed TST also provides good frequency domain energy concentration as compared to ST and ST with MLS ($k = 0.7$). Side-lobe artefacts of time-limited windows can also be observed at lower frequencies. These artefacts arise due to unnecessary shortening of frequency intervals at lower frequencies. This can be overcome by sacrificing time resolution (increasing k_1). The TFR of the proposed TST is shown in Fig. 3.7(j) for $k_1 = 45$. The corresponding optimum value of the parameter k_2 is found to be 0.4364. It provides better energy concentration in frequency domain, and resolves the two impulses precisely in time. However, in applications like event initiation and termination identification, it may not be desirable for the proposed TST to lose time resolution. Therefore, the frequency interval L_n can be saturated at lower frequencies to avoid very short frequency intervals. The modified scaling in TST is defined as follows

$$M_n = k_1, L_n = \begin{cases} k_2 n & \text{for } n > L_{th}/k_2 \\ L_{th} & \text{for } n \leq L_{th}/k_2 \end{cases} \quad (3.34)$$

where L_{th} determines the minimum desired frequency interval. Choice of suitable value of L_{th} can effectively eliminate side-lobe artefacts at lower frequencies. In Figs. 3.7(k) and 3.7(l), the TFRs of the proposed TST are shown with modified scaling for $L_{th} = 5$ while keeping k_1 and k_2 unchanged as used in Figs. 3.7(i) and (j), respectively.

The TFRs of the proposed BST are illustrated in Figs. 3.7(m)-(p). In order to precisely resolve the two frequency components, 50 Hz and 150 Hz, the value of k_3 must be less than 100. It can be observed in Fig. 3.7(m) that the two frequency components are clearly resolved using BST for $k_3 = 50$. In order to maximize the overall CM of the TFR, the

optimal value for parameter k_4 is found to be 7. Moreover, the proposed BST provides better time resolution as compared to conventional ST and ST with MLS for $k = 2$. Side-lobe spreading in time can also be observed at higher frequencies. This is due to the fact that, at higher frequencies, the time interval becomes very narrow due to progressive scaling which leads to side-lobe artefacts. These artefacts can be reduced by increasing the value of k_3 . The TFR of the proposed BST is shown in Fig. 3.7(n) for $k_3 = 100$ and $k_4 = 6$. It provides better time resolution, and resolves the two frequency components precisely. The side-lobe artefacts are also reduced. The time interval M_n can be saturated at higher frequencies to avoid selection of very short time intervals. The modified scaling in the proposed BST is defined as follows

$$L_n = k_3, \quad M_n = \begin{cases} \frac{k_4 N}{n} & \text{for } n < k_4 N / M_{th} \\ M_{th} & \text{for } n \geq k_4 N / M_{th} \end{cases} \quad (3.35)$$

where M_{th} denotes the desired minimum time interval. The suitable value of M_{th} can be chosen to effectively eliminate side-lobe artefacts at higher frequencies. In Figs. 3.7(n) and 3.7(o), the TFRs of the proposed BST are shown for $M_{th} = 5$ while keeping k_3 and k_4 unchanged as considered in Figs. 3.7(m) and 3.7(n), respectively.

Table 3.1: Comparison of TFRs shown in Fig. 3.7 in terms of CM

	ST	ST (MLS, k=2)	3PST [13]	4PST
CM	0.048	0.063	0.08	0.077
	TST	TST	TST	TST
	Fig. 3.7(i)	Fig. 3.7(j)	Fig. 3.7(k)	Fig. 3.7(l)
CM	0.089	0.093	0.095	0.132
	BST	BST	BST	BST
	Fig. 3.7(m)	Fig. 3.7(n)	Fig. 3.7(o)	Fig. 3.7(p)
CM	0.11	0.094	0.121	0.131

The CM for each TFR shown in Fig. 3.7 is listed in Table 3.1. The ST with MLS ($k = 2$), 3PST and 4PST concentrate more energy as compared to conventional ST, and correspondingly show more CM than that of conventional ST. The proposed TST and BST are able to concentrate more energy in given time and frequency intervals, respectively and have higher values of CM than that of other counterparts of ST. Table 3.1 shows the CM values obtained with proposed TST for different values of k_1 and k_2 , and also with modified scaling (MS). It can be observed in Table 3.1 that for larger values of k_1 and k_2 along with MS ($L_{th} = 5$), the TST can concentrate more energy and shows higher values of CM as compared to TST with lower values of k_1 and k_2 and with linear conventional scaling. The BST can also concentrate more energy for larger values of k_3 and k_4 along with MS ($M_{th} = 5$), and has higher value of CM as compared to BST with lower values

of k_3 and k_4 along with linear scaling.

Case Study 2: Applicability of TST in Multichannel Seismic Signals Analysis

ST and its modified variants are widely used for analyzing multichannel poststack seismic data to assist reservoir characterization [13], prediction of hydrocarbon reservoirs [53], and better understanding of the subsurface structural information [65, 113].

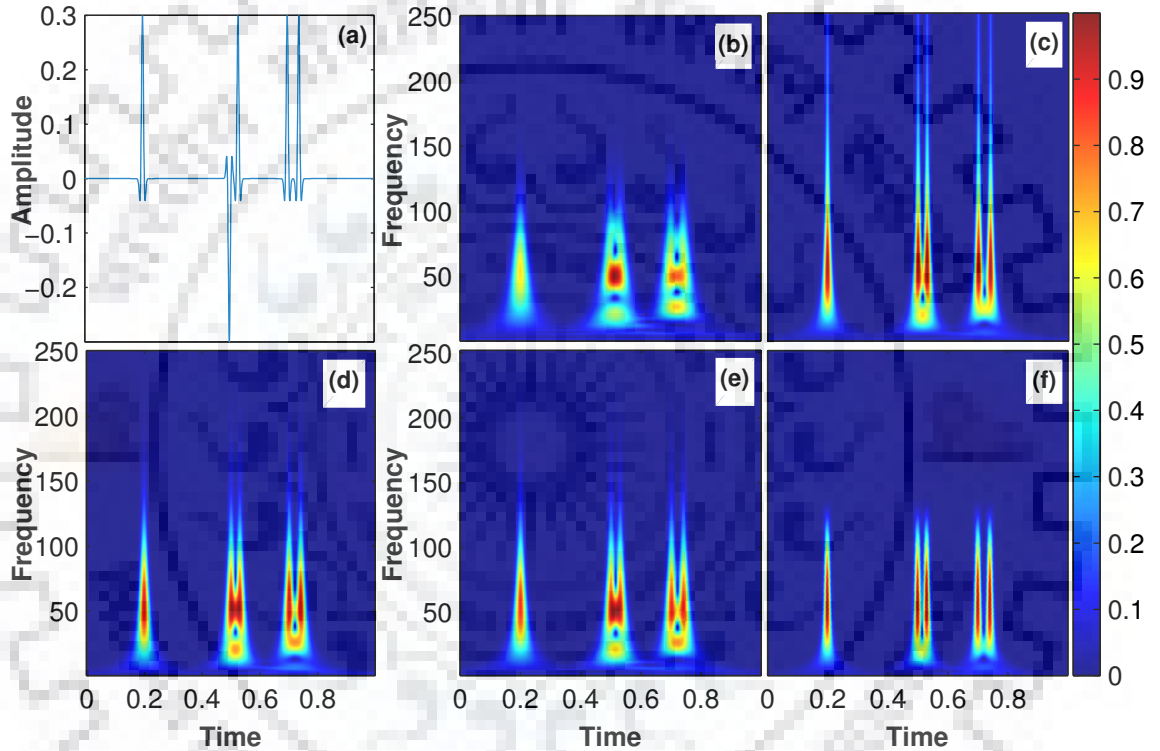


Fig. 3.8: Performance evaluation of proposed TST: (a) Synthetic seismic reflection data; TFR of (b) conventional ST; (c) ST with MLS for $k = 0.4$; (d) 3PST [13]; (e) 4PST [19]; (f) Proposed TST for $k_1 = 2, k_2 = 0.8$ and $L_{th} = 8$

To evaluate the performance of the proposed TST for analyzing multichannel seismic data, a synthetic seismic trace of length 1 second (s) is considered. The synthetic trace, shown in Fig. 3.8(a), is obtained through convolution between a three pair reflectivity and Ricker wavelet. The dominant frequency of the Ricker wavelet is 50 Hz. The first reflectivity in trace has only one positive reflectivity of magnitude 0.3. The second reflection set consists of two reflectivities of magnitude 0.3 of opposite sign. The third reflection set consists of two positive reflectivities of magnitude 0.3. The time duration of second and third reflectivity pairs are 0.003 s and 0.004 s, respectively. Figs. 3.8(b) and 3.8(c) show normalized amplitude spectrum of the TFRs obtained with conventional ST and ST

with MLS for $k = 0.4$, respectively. The TFR of ST is smeared in time and therefore, second and third reflection pairs are not distinguishable. TFR of ST with MLS improves the time resolution at the cost of degraded frequency resolution. The time resolution has improved in Fig. 3.8(c) compared to that in Fig. 3.8(b), and the second and third reflectivity pairs are almost distinguishable. However, reflectivities are smeared in frequency. It can be observed in Fig. 3.8(d) that both time and frequency resolution have improved in 3PST as compared to conventional ST. However, the second and third reflection sets are not distinguishable. The 4PST further improves the frequency resolution as shown in Fig. 3.8(e), however, it could not distinguish the second and third reflectivity pairs. The TFR obtained with the proposed TST is shown in Fig. 3.8(e) for $k_1 = 2, k_2 = 0.8$ and $L_{th} = 8$. The proposed TST clearly distinguishes the second and third reflectivity pairs with better frequency resolution than that of other shown variants of ST. The synthetic signal illustrates that the proposed TST is superior to the conventional and other shown variants of ST in detecting thin beds.

Table 3.2: Comparison of TFRs shown in Fig. 3.8 in terms of CM

	ST	ST with MLS	3PST [13]	4PST	Proposed TST
CM	0.091	0.094	0.11	0.125	0.16

The CM [112] for each TFR shown in Fig. 3.8 is listed in Table 3.2. It can be observed that the proposed TST outperforms other variants of ST. The ability of the proposed TST in concentrating the energy in given interval in time domain with minimum degradation in frequency domain can be qualitatively observed in Fig. 3.8(f).

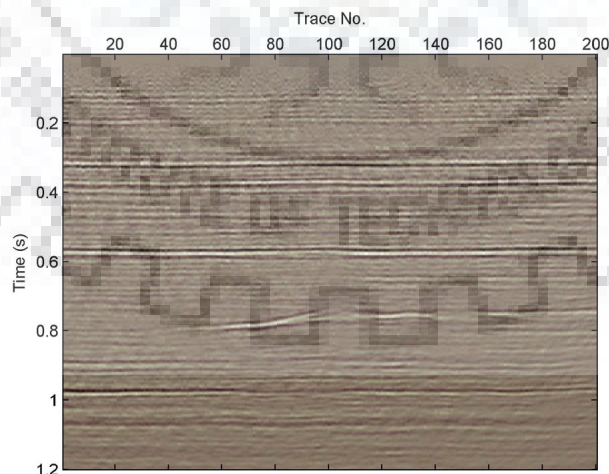


Fig. 3.9: Field Data [53]

The efficacy of the proposed TST is investigated further using a 2 dimensional (2D) field data. The field data consists of 200 traces as shown in Fig. 3.9. This data is used previously in [53, 65, 113–115]. The 100th trace of the 2D field data, shown in Fig.

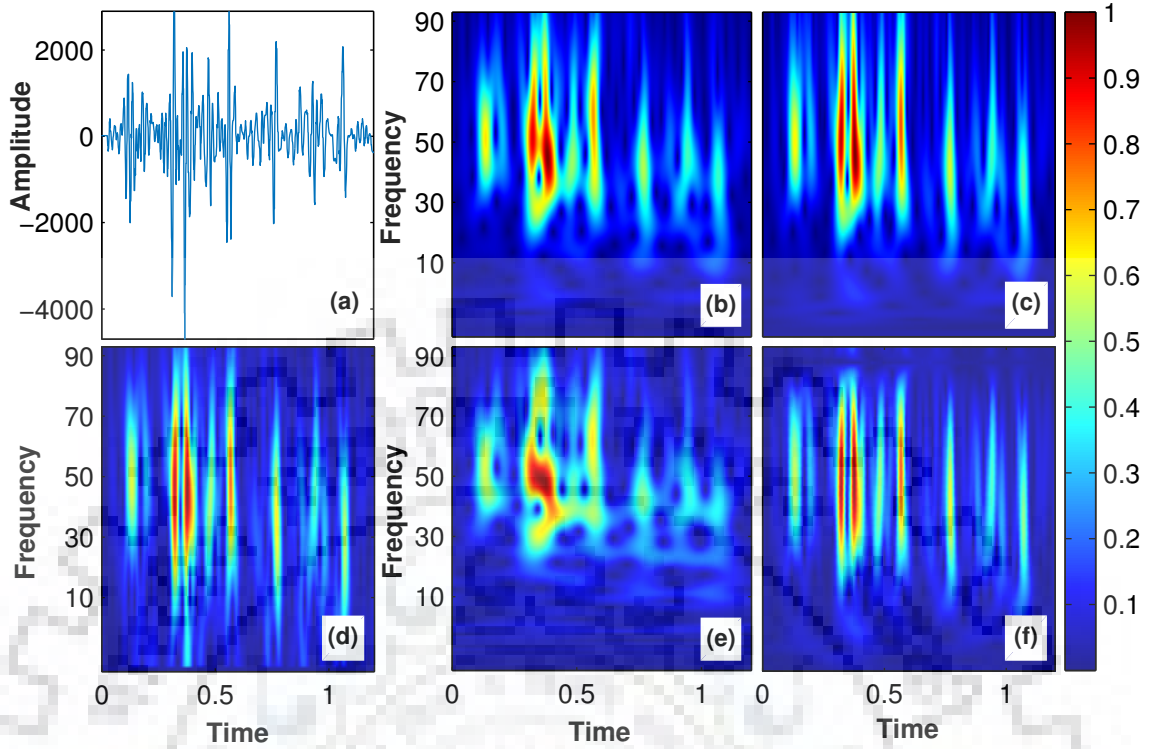


Fig. 3.10: Performance evaluation of proposed TST: (a) 100th trace of 2D field data; TFR of (b) conventional ST; (c) ST with MLS for $k = 0.7$; (d) 3PST [13]; (e) 4PST [19]; (f) Proposed TST for $k_1 = 2$, $k_2 = 0.4$ and $L_{th} = 5$

3.10(a), is analyzed. Figs. 3.10(b)-(f) show the TFR of ST, ST with MLS ($k = 0.7$), 3PST, 4PST and the proposed TST for $k_1 = 2$, $k_2 = 0.4$ and $L_{th} = 5$.

The strong anomalies of 45 Hz at 0.38 s and 52 Hz at 0.32 s can be observed in each TFR. Moreover, the decreasing amplitudes of frequency components with time can also be observed due to seismic attenuation during the seismic wave propagation. The TFR of the ST provides poor time resolution, and the 45 Hz anomaly has merged with 52 Hz anomaly. The MLS provides better time resolution than that of the conventional ST. However, the two anomalies are not clearly separable, and frequency resolution also gets poorer. The two anomalies are almost separable using 3PST, however, the frequency resolution is worst among all TFRs. The time resolution in 4PST is poorer than that of all TFRs. The two anomalies are clearly separable in the TFR obtained by the proposed TST. Moreover, the frequency resolution is also better than that of other shown variants of ST. It can be observed that the proposed TST is beneficial to identify hidden subsurface properties (mainly caused by the viscous elasticity beneath the ground) more precisely, and facilitate better understanding of subsurface lithology properties.

The CM for each TFR shown in Fig. 3.10 is listed in Table 3.3. The ability of the proposed TST in concentrating the energy in given intervals can be observed in Table 3.3.

The TFRs of 4PST and proposed TST provide better CM as compared to other TFRs. The CM of proposed TST is 61.44% larger than that of 4PST. Therefore, the proposed TST outperforms other shown variants of ST.

Table 3.3: Comparison of TFRs shown in Fig. 3.10 in terms of CM

	ST	ST with MLS	3PST	4PST	Proposed TST
CM	0.07	0.073	0.081	0.083	0.134

Case Study 3: Analysis of Band-limited EEG signals for BCI Applications using Proposed BST

EEG signals are non-stationary in nature. TFA of EEG signals is beneficial to analyze different states of brain during different mental tasks. The ST and its modified variants are widely used for EEG signal analysis [55,102,103]. Several brain computer interface (BCI) systems depend on event-related desynchronization (ERD) [116]. During both planning and execution of hand movements, the ERD can be detected for most of the subjects within the band of μ -rhythm (6-14 Hz) [116].

The performance of the proposed BST is evaluated using real EEG data from BCI Competition IV [117]. This work considers only hand movement imagery. Data is filtered to 6-14 Hz band using 5th order Butter-worth filter for analyzing the μ -band only. To

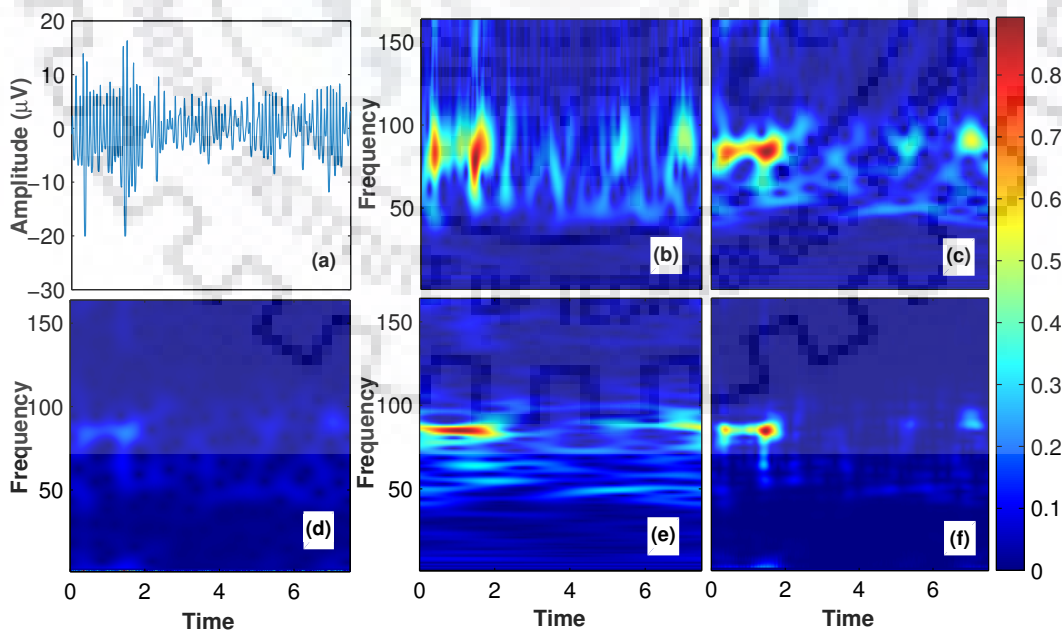


Fig. 3.11: Performance evaluation of proposed BST: (a) EEG signal [117]; TFR of (b) conventional ST; (c) ST with MLS for $k = 2.45$; (d) 3PST; (e) 4PST; (f) Proposed BST for $k_3 = 7$, $k_4 = 4$ and $M_{th} = 7$

evaluate the efficacy of the proposed BST, single trial ERD pattern of right hand imagery at C3 location of subject 3 is analyzed, which is also shown in Fig. 3.11(a). The single trial ERD pattern can be detected as an energy decreasing phenomenon after the onset of event as shown in Fig. 3.11. Since this ERD only exists before the movement onset, this phenomenon is extremely sensitive to time delay. The ERD can be observed in 10-12 Hz band in all TFRs shown in Fig. 3.11. Figs. 3.11(b)-(f) show the TFRs obtained with conventional ST with LS, ST with MLS, 3PST, 4PST and proposed BST, respectively. Frequency resolution has improved by using MLS, but at the cost of degradation in time resolution. It can be observed in Fig. 3.11(d) that the 3PST is unable to detect the real time motor sensory ERD. The 4PST provides good frequency resolution than that of other counterparts, however, the time resolution is worst. Since the detection is highly sensitive to time delay, the performance of 4PST is not desirable. The TFR of proposed BST provides better frequency resolution with least degradation in time resolution as shown in Fig. 3.11(f). Some side-lobe spreading is also observed in Fig. 3.11(f) which can be ignored for such applications.

Table 3.4: Comparison of TFRs shown in Fig. 3.11 in terms of CM

	ST	ST with MLS	3PST	4PST	Proposed BST
CM	0.077	0.92	0.061	0.102	0.133

The CM for each TFR shown in Fig. 3.11 is listed in Table 3.4. The Table 3.4 quantifies the performance of the proposed BST in concentrating the energy in given frequency intervals with minimum degradation in time. In this example, the CM of proposed BST is 30.39% larger than that of 4PST. Therefore, the proposed BST outperforms other shown variants of ST.

Case Study 4: Analysis of Power Quality Disturbances using Proposed BST

The ST and its modified variants are widely used in literature for analyzing different power quality disturbances [18, 19, 118, 119]. In this case study, the performance of the proposed BST is evaluated for analysis of voltage harmonics present in power signals. The considered synthetic signal contains odd harmonic components upto order 7 along with voltage interruption and transients. The signal has a fundamental frequency component of 50 Hz, and is sampled at a frequency of 3.2 KHz as per the institute of electrical and electronics engineers (IEEE) 1159 standards [120]. The magnitude of fundamental frequency component and third, fifth and seventh harmonic components are 1, 0.1, 0.1 and 0.099 pu, respectively. The duration of voltage interruption is from $t = 0.06$ s to t

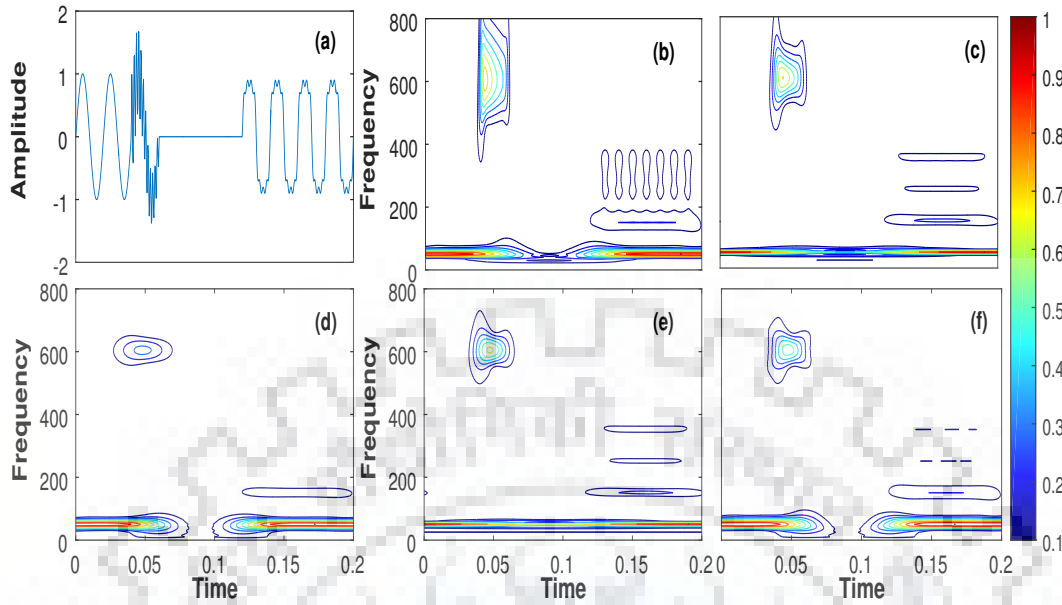


Fig. 3.12: Performance evaluation of proposed BST: (a) Signal having multiple power quality disturbances; TFR of (b) conventional ST; (c) ST with MLS for $k = 2$; (d) 3PST; (e) 4PST; (f) Proposed BST for $k_3 = 10$, $k_4 = 3$ and $M_{th} = 2$

$= 0.12$ s. The harmonics start just after the voltage interruption, and last for rest of the duration. The signal is shown in Fig. 3.12(a). In Fig. 3.12(b), the contour plot of TFR of conventional ST is shown. It can be observed that the fifth and seventh harmonics are not clearly distinguishable. Due to very poor time resolution at lower frequencies, the voltage interruption is not detectable. Moreover, due to very poor frequency resolution, the transient is completely smeared in frequency. The TFR of ST with MLS for $k = 2$ is shown in Fig. 3.12(c). The frequency resolution has improved with MLS, however, time resolution for voltage interruption has degraded. Fig. 3.12(d) and (e) show the TFRs using 3PST and 4PST. The 3PST provides better time resolution for voltage interruption. However, the 5th and 7th harmonic components are absent, and time resolution of transient has also degraded. All three harmonic components are detected, and frequency resolution of transient has also improved using 4PST. However, the time resolution of voltage interruption is worst. The efficacy of the proposed BST can be observed in Fig. 3.12(f). The TFR of the proposed BST for $k_3 = 10$, $k_4 = 3$ and $M_{th} = 2$, provides better time and frequency resolution for all disturbances. The voltage interruption and all three harmonic components are accurately detected and distinguishable. The frequency resolution for transient has also improved.

The CM for each TFR shown in Fig. 3.12 is listed in Table 3.5. In this case study, the CM of proposed BST is 26.64% larger than that of 4PST. Therefore, the proposed BST outperforms other shown variants of ST in case of detection of multiple power quality

Table 3.5: Comparison of TFRs shown in Fig. 3.12 in terms of CM

	ST	ST with MLS	3PST	4PST	Proposed BST
CM	0.098	0.104	0.1	0.1085	0.1374

disturbances.

3.7 Conclusion

In this chapter, the optimal time-limited and band-limited windows have been proposed to precisely resolve the time-limited and band-limited signals in time and frequency, respectively. The proposed time-limited window is strictly limited in a finite time interval, and has maximum energy concentration in desired frequency interval. Similarly, the proposed band-limited window is strictly limited in a given frequency interval while maximizing the energy concentration in desired interval in time. Based on these windows, two variants of ST namely, TST and BST have been proposed. For progressive resolution in the proposed TST and BST, the scaling criteria have also been suggested. The efficacy of the proposed TST and BST has been tested on a set of synthetic and real field data, and compared with conventional ST and its variants. Simulation results clearly illustrated that the proposed BST can precisely resolve two closely spaced frequency components, whereas the proposed TST can precisely localize a desired spectral component in time. Therefore, the proposed techniques can be used in numerous applications where a very precise resolution is desired in either time or frequency domain.



Chapter 4

Simultaneous Time and Frequency Domain Energy Concentration for Finite Length Sequences

4.1 Introduction

The compact kernels which are confined in both time and frequency domains, are highly desired for several applications in the field of signal processing [108] and communication [121] such as filter design [122, 123], spectral estimation [124, 125], time-frequency analysis [126–128], windowing at the transmitter and receiver in wireless communication system [129], windowed OFDM [129], etc. It is often required to design sharp spectral roll-off filters which are simultaneously compact in time domain [130]. Choice of kernels plays a crucial role in time-frequency analysis for localization of spectral contents in both time and frequency domains [131].

From the theory of Fourier transform (FT), it is a well known fact that a signal and its FT can not be simultaneously limited beyond certain extent. Therefore, there is a need to develop compact window functions which are optimal in some sense or other. In literature, compactness of a window is defined through different measures in literature such as notion of entropy [132, 133], notion of spread [134, 135], notion of energy concentration [109, 136], etc.

The most familiar Heisenberg uncertainty principle [137] related to this phenomenon states that, for any arbitrary signal $f(t)$, minimum achievable time-bandwidth product is $1/2$ i.e. $T\Omega \geq 1/2$ where T and Ω denote spread of signal in time and frequency domain,

respectively. T^2 and Ω^2 are defined as

$$T^2 = \frac{\int_{-\infty}^{\infty} (t - t_0)^2 |f(t)|^2 dt}{\int_{-\infty}^{\infty} |f(t)|^2 dt}, \quad \Omega^2 = \frac{\int_{-\infty}^{\infty} (w - w_0)^2 |F(w)|^2 dw}{\int_{-\infty}^{\infty} |F(w)|^2 dw} \quad (4.1)$$

where $F(w)$ represents the FT of $f(t)$. t_0 and w_0 denote mean of $f(t)$ and $F(w)$, respectively. The continuous Gaussian function is the minimizer of this principle. This phenomenon and related properties are well defined and extensively studied in literature for continuous signals [138, 139]. However, for discrete sequences, the Heisenberg uncertainty bound is not achievable [140, 141]. Parhizkar et al. [141] have introduced the uncertainty minimizers for discrete sequences and termed them as most compact sequences.

The seminal work of Slepian, Landau and Pollak [56, 109] define compactness based on notion of energy concentrations in finite time and frequency intervals. Energy concentrations in time and frequency domains in a given finite time interval $[-T, T]$ and finite frequency band $[-\Omega, \Omega]$ are defined as

$$\alpha^2 = \frac{\int_{-T/2}^{T/2} |f(t)|^2 dt}{\int_{-\infty}^{\infty} |f(t)|^2 dt}, \quad \beta^2 = \frac{\int_{-\Omega}^{\Omega} |F(w)|^2 dw}{\int_{-\infty}^{\infty} |F(w)|^2 dw} \quad (4.2)$$

Slepian and Pollak [56] have proposed optimal functions to simultaneously maximize α^2 and β^2 . A set of band limited functions limited in band $(-\Omega, \Omega)$, namely PSWFs are introduced [56], out of which the zero order PSWF [142–144] denoted by $\psi_0(t)$, possesses interesting optimality property of achieving maximum energy concentration in time interval $(-T/2, T/2)$. The maximum achievable concentration denoted by $\lambda_0(T\Omega)$ is the maximum eigenvalue of the following associated eigenfunction equation

$$\int_{-T/2}^{T/2} \frac{\sin(\Omega(t-s))}{\pi(t-s)} \psi_i(s) ds = \lambda_i \psi_i(t), \quad i = 0, 1, 2, \dots \quad (4.3)$$

$\psi_0(t)$ achieves $\alpha^2 = \lambda_0(T\Omega)$ for $\beta^2 = 1$. For given T and Ω , no other band limited function can achieve α^2 greater than $\lambda_0(T\Omega)$ [56]. The time limited counterpart denoted by $\bar{\psi}_0(t)$, can be obtained by limiting $\psi_0(t)$ in the time interval $(-T/2, T/2)$ [145, 146]. $\bar{\psi}_0(t)$ achieves the maximum concentration in the given band $(-\Omega, \Omega)$ i.e. $\beta^2 = \lambda_0(T\Omega)$ for $\alpha^2 = 1$.

The aforementioned functions are either time limited or band limited with maximum concentration in other respective domain. Therefore, the desired function is that which can maximize β^2 (or α^2) for a desired α^2 (or β^2) or simultaneously maximize α^2 and β^2 . The problem is addressed in [109, 147], and an optimal function is introduced which can be obtained by linear combination of $\psi_0(t)$ and $\bar{\psi}_0(t)$. For a fixed $T\Omega$, the maximum

achievable α^2 and β^2 fall on an elliptical arc formed by [56]

$$\alpha^2 - 2\alpha\beta\sqrt{\lambda_0(T\Omega)} + \beta^2 = 1 - \lambda_0(T\Omega) \quad (4.4)$$

Slepian [57] has proposed the optimal sequences to simultaneously maximize the time and frequency domain energy concentrations for a given time interval $(-M/2, M/2 - 1)$ and a normalized frequency band $(-B, B)$. The time and frequency domain concentrations for discrete sequence $x[n]$ can be defined as [57]

$$\alpha^2 = \frac{\sum_{-M/2}^{M/2-1} |x[n]|^2}{\sum_{-\infty}^{\infty} |x[n]|^2}, \quad \beta^2 = \frac{\int_{-B}^B |X(f)|^2 df}{\int_{-1/2}^{1/2} |X(f)|^2 df} \quad (4.5)$$

A set of band limited sequences limited in normalized frequency band $(-B, B)$, namely DPSSs are introduced in [57]. The usefulness of these sequences are discussed in [148–150].

The zero order band limited DPSS denoted by $\nu_\infty[n]$, achieves maximum energy concentration in time samples of length M . The maximum achievable time domain energy concentration is denoted by $\alpha^2 = \lambda_0(M, B)$ which is the maximum eigenvalue of the following associated eigenfunction equation [57]

$$\sum_{m=-M/2}^{M/2-1} \frac{\sin(2\pi B[n-m])}{\pi[n-m]} \nu_\infty[m] = \lambda_0(M, B) \nu_\infty[n] \quad (4.6)$$

where $n = 0, \pm 1, \pm 2, \dots, \pm\infty$. $\nu_\infty[n]$ is of infinite length in time domain. The time limited counterpart denoted by $\nu_M[n]$, is a M -length sequence *i.e.* which maximizes β^2 while $\alpha^2 = 1$ [57].

The minimizer of the uncertainty in this discrete time continuous frequency scenario can be obtained by linear combination of $\nu_\infty[n]$ and $\nu_M[n]$. The achievable α^2 and β^2 in this case fall on an elliptical arc formed by [57]

$$\alpha^2 - 2\alpha\beta\sqrt{\lambda_0(M, B)} + \beta^2 = 1 - \lambda_0(M, B) \quad (4.7)$$

for given values of M and B . For both simultaneously concentrated PSWF and DPSS, maxima of the product $\alpha^2\beta^2$ is obtained at $\alpha^2 = \beta^2$.

In [125, 151], the authors have introduced a counterpart of band-limited DPSSs in finite dimensional space and named it as P-DPSSs. These P-DPSSs are band limited in the interval $(-L, L)$ while maximally energy concentrated in the time interval $(-M/2, M/2 - 1)$. Similar to PSWFs and DPSSs, P-DPSSs can be obtained by finding the eigenvector of

associated eigenfunction equation [151]

$$\sum_{m=-M/2}^{M/2-1} \frac{\sin([n-m](2L+1)\pi/N)}{N\sin([n-m]\pi/N)} \phi_M[m] = \lambda(M, B)\phi_M[n]$$

The associated properties of these sequences are studied in [110, 111, 125, 152, 153].

For most of the practical applications of digital signal processing where we often encounter with finite duration signals, it is desired to have simultaneously concentrated discrete window with finite support. To this extent, this objective focuses on discrete time continuous frequency scenario which closely relates to DPSS. However, the optimal simultaneously concentrated DPSS is of infinite length. A straight forward approach is to truncate the simultaneously concentrated DPSS to desired finite length, but the resulting window will no longer guarantee to be optimal. Therefore, from practical standpoint and out of mathematical curiosity, this work aims at designing the optimal compact window with finite support which can simultaneously maximize the energy concentration in finite time interval and finite frequency band.

The problem of simultaneous maximization of two objective functions namely α^2 and β^2 is formulated as the maximization of weighted linear combination of desired concentration measures in time and frequency domains. The problem is solved through eigenvalue decomposition to give Pareto-optimal solutions. Further, upper bounds of achievable α^2 and β^2 for finite length sequences is derived. The optimal sequence thus obtained is termed as OWFS. This work derives several properties analytically illustrating the impact of chosen weight on α^2 , β^2 and $\alpha^2\beta^2$.

The work theoretically derives the condition to maximize $\alpha^2\beta^2$. It is shown that the condition for maximum $\alpha^2\beta^2$ may not necessarily align with $\alpha^2 = \beta^2$ for finite length sequences. Moreover, the work analytically proves that as the support of the proposed window approaches infinity, the proposed achievable upper bound merges with the achievable bound of simultaneously concentrated DPSS. To illustrate the efficacy of the proposed OWFS, it is compared with simultaneously concentrated truncated DPSS as well as other well-known window kernels.

This objective also briefly discusses the discrete time discrete frequency scenario which is closely related to P-DPSS. The existing work on P-DPSS mainly focuses on band limited sequences. To our knowledge, the simultaneously concentrated P-DPSS and corresponding achievable upper-bounds of α^2 and β^2 are not explored in literature. In this objective, another unique approach of multiobjective optimization similar to the one followed in the discrete time continuous frequency case is adopted to obtain upper bound of maximum achievable α^2 and β^2 .

4.2 Problem Formulation and Analysis

In this section, the simultaneous maximization of time and frequency domain energy concentrations for a finite length sequence of length N is formulated as a multiobjective optimization problem. The eigenvalue analysis of the corresponding cost function is carried out.

Problem Formulation

Consider a window \mathbf{w} of length N as

$$\mathbf{w} = \left(w[-\lfloor N/2 \rfloor], w[-\lfloor N/2 \rfloor + 1], \dots, w[\lfloor N/2 \rfloor - 1] \right)^T \quad (4.8)$$

The discrete time FT of \mathbf{w} is given by

$$W(f) = \sum_{n=-\lfloor N/2 \rfloor}^{\lfloor N/2 \rfloor - 1} w[n] e^{-i2\pi f n} = \mathbf{w}^T \mathbf{h}(f) \quad (4.9)$$

where

$$\mathbf{h}(f) = \left(e^{-i2\pi f[-\lfloor N/2 \rfloor]}, e^{-i2\pi f[-\lfloor N/2 \rfloor + 1]}, \dots, e^{-i2\pi f[\lfloor N/2 \rfloor - 1]} \right)^T$$

The energy concentration in frequency domain in a given frequency interval $(-B, B)$ can be considered as

$$\beta^2 = \frac{\int_{-B}^B |W(f)|^2 df}{\int_{-\frac{1}{2}}^{\frac{1}{2}} |W(f)|^2 df} \quad (4.10)$$

By using (4.9), the numerator of (4.10) can be rewritten as

$$\int_{-B}^B |W(f)|^2 df = \int_{-B}^B |\mathbf{w}^T \mathbf{h}(f)|^2 df = \mathbf{w}^T \mathbf{A}^{(B,N)} \mathbf{w} \quad (4.11)$$

where $\mathbf{A}^{(B,N)} = \int_{-B}^B \mathbf{h}(f) \mathbf{h}^H(f) df$ is an $N \times N$ positive semi-definite matrix. The $(m, n)^{th}$ element of $\mathbf{A}^{(B,N)}$ is denoted by

$$\begin{aligned} [\mathbf{A}^{(B,N)}]_{m,n} &= \int_{-B}^B e^{-i2\pi f[m-n]} df \\ &= \begin{cases} \frac{\sin(2\pi B[m-n])}{\pi[m-n]} & m \neq n \\ 2B, & m = n \end{cases} \end{aligned} \quad (4.12)$$

where $m, n = 1, \dots, N$. At $B = \frac{1}{2}$, $\mathbf{A}^{(B,N)}$ becomes an identity matrix. Using (4.11)

and (4.12), (4.10) can be redefined as

$$\beta^2 = \frac{\mathbf{w}^T \mathbf{A}^{(B,N)} \mathbf{w}}{\mathbf{w}^T \mathbf{w}} \quad (4.13)$$

The time domain energy concentration in a given time interval $(-\lfloor M/2 \rfloor, \lfloor M/2 \rfloor - 1)$, where $M \leq N$, can be represented as

$$\alpha^2 = \frac{\sum_{n=-\lfloor M/2 \rfloor}^{\lfloor M/2 \rfloor - 1} |w[n]|^2}{\sum_{n=-\lfloor N/2 \rfloor}^{\lfloor N/2 \rfloor - 1} |w[n]|^2} = \frac{\mathbf{w}^T \mathbf{T}^{(M,N)} \mathbf{w}}{\mathbf{w}^T \mathbf{w}} \quad (4.14)$$

where $\mathbf{T}^{(M,N)}$ represents an $N \times N$ diagonal matrix with M ones and $N - M$ zeros along the main diagonal. The $(m, n)^{th}$ element of $\mathbf{T}^{(M,N)}$ can be defined as

$$[\mathbf{T}^{(M,N)}]_{m,n} = \begin{cases} 1, & m = n \text{ and } 1 + \lfloor \frac{N}{2} \rfloor - \lfloor \frac{M}{2} \rfloor \leq m \leq \lfloor \frac{N}{2} \rfloor + \lfloor \frac{M}{2} \rfloor \\ 0, & \text{elsewhere} \end{cases} \quad (4.15)$$

For maximum energy concentration in both time and frequency domains, the aim is to maximize both α^2 and β^2 simultaneously. Scalarization is one of the standard techniques to solve multiple objective problems where two or more objective functions are combined into single objective function by weighted linear combinations of individual objectives [154]. In particular, if all objective functions are convex then the solutions obtained through scalarization leads to pareto optimal solutions *i.e.* from this solution one cannot improve one objective without degrading other. The objective functions under consideration *i.e.* α^2 and β^2 are convex (subject to $\mathbf{w}^T \mathbf{w} = 1$) because their Hessian [154], $\frac{d^2 \alpha^2}{d\mathbf{w}^2} = \mathbf{A}^{(B,N)}$ and $\frac{d^2 \beta^2}{d\mathbf{w}^2} = \mathbf{T}^{(M,N)}$ are semidefinite matrices. The approach of scalarization is adopted to simultaneously maximize both α^2 and β^2 . The Pareto optimality of solutions is proved in property 1 of subsequent section. The problem of simultaneous maximization of α^2 and β^2 can be defined as follows

$$\begin{aligned} & \max_{\mathbf{w}, \mu} \quad \mu \alpha^2 + (1 - \mu) \beta^2, \\ & \text{subject to} \quad \mathbf{w}^T \mathbf{w} = 1, \quad 0 < \mu < 1 \end{aligned} \quad (4.16)$$

where the parameter μ acts as a relative weighing factor. The larger value of μ favors maximization of energy concentration in the time interval $(-M/2, M/2)$, whereas the smaller value of μ tries to maximize the energy concentration in the given frequency interval $(-B, B)$. For a fixed value of $\mu \in (0, 1)$, using (4.13) and (4.14), (4.16) can be

redefined as follows

$$\begin{aligned} & \max_{\mathbf{w}} \quad \mathbf{w}^T \mathbf{P} \mathbf{w}, \\ & \text{subject to} \quad \mathbf{w}^T \mathbf{w} = 1 \end{aligned} \quad (4.17)$$

where

$$\mathbf{P} = (1 - \mu) \mathbf{A}^{(B,N)} + \mu \mathbf{T}^{(M,N)} \quad (4.18)$$

\mathbf{P} is a positive semi-definite matrix. For a fixed value of μ , the solution to the problem defined in (4.17) is an eigenvector, \mathbf{w}_0 , of matrix \mathbf{P} corresponding to the maximum eigenvalue λ_0 . Thus, \mathbf{w}_0 and λ_0 satisfy

$$((1 - \mu) \mathbf{A}^{(B,N)} + \mu \mathbf{T}^{(M,N)}) \mathbf{w}_0 = \lambda_0 \mathbf{w}_0 \quad (4.19)$$

These Pareto-optimal solutions obtained by varying μ , ensure that α^2 can not be further improved without degrading β^2 or vice-versa. Hence, the optimal solution gives Pareto-optimal front or upper bound of uncertainty for a finite length sequence.

4.3 Properties of Time Domain (α^2) and Frequency Domain (β^2) Energy Concentrations

4.3.1 Property 1

The time domain energy concentration, $\alpha^2 = \mathbf{w}_0^T \mathbf{T}^{(M,N)} \mathbf{w}_0$, and the frequency domain energy concentration, $\beta^2 = \mathbf{w}_0^T \mathbf{A}^{(B,N)} \mathbf{w}_0$, are increasing and decreasing functions of μ , respectively

Proof: The first derivative of α^2 with respect to μ can be formulated as

$$\begin{aligned} \frac{d\alpha^2}{d\mu} &= 2 \mathbf{w}_0^T \mathbf{T}^{(M,N)} \frac{d\mathbf{w}_0}{d\mu} \\ &= \left(\frac{2}{1 - \mu} \right) \mathbf{w}_0^T \mathbf{T}^{(M,N)} \mathbf{D}^0 (-\mathbf{P} + \mathbf{T}^{(M,N)}) \mathbf{w}_0 \\ &\quad \text{(Using Lemma 2 (see Appendix) and (4.18))} \\ &= \left(\frac{2}{1 - \mu} \right) \text{Tr}(\mathbf{w}_0^T \mathbf{T}^{(M,N)} \mathbf{U} \mathbf{R}^0 \mathbf{U}^T \mathbf{T}^{(M,N)} \mathbf{w}_0) \\ &\quad \text{(Using (7.2) and (7.4))} \end{aligned}$$

$$\begin{aligned}
 \frac{d\alpha^2}{d\mu} &= \left(\frac{2}{1-\mu} \right) \text{Tr} (\mathbf{R}^0 \mathbf{U}^T \mathbf{T}^{(M,N)} \mathbf{w}_0 \mathbf{w}_0^T \mathbf{T}^{(M,N)} \mathbf{U}) \\
 &\quad \text{(Using cyclic property of trace)} \\
 &= \left(\frac{2}{1-\mu} \right) \sum_{i=1}^{N-1} \frac{(\mathbf{w}_i^T \mathbf{T}^{(M,N)} \mathbf{w}_0)^2}{(\lambda_0 - \lambda_i)} \quad \text{(using (7.5))} \tag{4.20}
 \end{aligned}$$

Since, $\lambda_0 > \lambda_i$ for $i = 1, \dots, N-1$, it can be concluded that $\frac{d\alpha^2}{d\mu} \geq 0$. Hence, α^2 is an increasing function of μ .

The first derivative of β^2 with respect to μ can be formulated as

$$\begin{aligned}
 \frac{d\beta^2}{d\mu} &= 2\mathbf{w}_0^T \mathbf{A}^{(B,N)} \frac{d\mathbf{w}_0}{d\mu} \\
 &= \left(\frac{2}{\mu} \right) \mathbf{w}_0^T \mathbf{A}^{(B,N)} \mathbf{D}^0 (-\mathbf{A}^{(B,N)} + \mathbf{P}) \mathbf{w}_0 \\
 &\quad \text{(Using Lemma 2 (see Appendix) and (4.18))} \\
 &= - \left(\frac{2}{\mu} \right) \text{Tr} (\mathbf{w}_0^T \mathbf{A}^{(B,N)} \mathbf{U} \mathbf{R}^0 \mathbf{U}^T \mathbf{A}^{(B,N)} \mathbf{w}_0) \\
 &\quad \text{(Using (7.2) and (7.4))} \\
 &= - \left(\frac{2}{\mu} \right) \sum_{i=1}^{N-1} \frac{(\mathbf{w}_i^T \mathbf{A}^{(B,N)} \mathbf{w}_0)^2}{(\lambda_0 - \lambda_i)} \quad \text{(using (7.5))} \tag{4.21}
 \end{aligned}$$

Since, $\lambda_0 > \lambda_i$ for $i = 1, \dots, N-1$, it can be concluded that $\frac{d\beta^2}{d\mu} \leq 0$. Hence, β^2 is a decreasing function of μ .

This also proves the Pareto optimality of solutions obtain from the problem (4.17) because both α^2 or β^2 can not be increased further without decreasing the other.

4.3.2 Property 2

The product $(\alpha^2 \beta^2)$ of time and frequency domain energy concentrations is a concave function of μ .

Proof: The first derivative of $\alpha^2 \beta^2$ can be formulated as

$$\frac{d(\alpha^2 \beta^2)}{d\mu} = 2(\mathbf{w}_0^T \mathbf{A}^{(B,N)} \mathbf{w}_0) \mathbf{w}_0^T \mathbf{T}^{(M,N)} \frac{d\mathbf{w}_0}{d\mu} + 2\mathbf{w}_0^T \mathbf{A}^{(B,N)} \frac{d\mathbf{w}_0}{d\mu} (\mathbf{w}_0^T \mathbf{T}^{(M,N)} \mathbf{w}_0) \tag{4.22}$$

Using **Property 1**, (4.22) can be rewritten as

$$\frac{d(\alpha^2 \beta^2)}{d\mu} = \frac{2\mathbf{w}_0^T \mathbf{T}^{(M,N)} \mathbf{D}^0 \mathbf{T}^{(M,N)} \mathbf{w}_0}{(1-\mu)^2} f(\mu) \tag{4.23}$$

or

$$\frac{d(\alpha^2\beta^2)}{d\mu} = \frac{2\mathbf{w}_0^T \mathbf{A}^{(B,N)} \mathbf{D}^0 \mathbf{A}^{(B,N)} \mathbf{w}_0}{(\mu)^2} f(\mu) \quad (4.24)$$

where

$$f(\mu) = (1 - \mu)\mathbf{w}_0^T \mathbf{A}^{(B,N)} \mathbf{w}_0 - \mu\mathbf{w}_0^T \mathbf{T}^{(M,N)} \mathbf{w}_0 \quad (4.25)$$

Since $\mathbf{w}_0^T \mathbf{T}^{(M,N)} \mathbf{D}^0 \mathbf{T}^{(M,N)} \mathbf{w}_0$ and $\mathbf{w}_0^T \mathbf{A}^{(B,N)} \mathbf{D}^0 \mathbf{A}^{(B,N)} \mathbf{w}_0$ in (4.23) and (4.24) are always positive for $\mu \in (0, 1)$ (see **Property 1**),

$$\frac{d(\alpha^2\beta^2)}{d\mu} = 0 \quad \text{for} \quad f(\mu) = 0 \quad (4.26)$$

Taking first derivative of $f(\mu)$,

$$\begin{aligned} \frac{d}{d\mu} f(\mu) &= -\mathbf{w}_0^T \mathbf{A}^{(B,N)} \mathbf{w}_0 + (1 - \mu)2\mathbf{w}_0^T \mathbf{A}^{(B,N)} \frac{d\mathbf{w}_0}{d\mu} \\ &\quad - \mathbf{w}_0^T \mathbf{T}^{(M,N)} \mathbf{w}_0 - \mu 2\mathbf{w}_0^T \mathbf{T}^{(M,N)} \frac{d\mathbf{w}_0}{d\mu} < 0 \end{aligned} \quad (4.27)$$

Using **Property 1** and (4.25), it can be concluded that

$$f(\mu) \Big|_{\mu \rightarrow 0} > 0 \quad \text{and} \quad f(\mu) \Big|_{\mu \rightarrow 1} < 0 \quad (4.28)$$

Therefore, $f(\mu)$ is a monotonic decreasing function of μ . Hence, there is only one value of μ for which $f(\mu) = 0$, and this can be denoted as μ_{opt} . Using (4.24) and (4.28), it can be concluded that the product $(\alpha^2\beta^2)$ is a concave function of μ . The maximum value of $\alpha^2\beta^2$ is achieved for $\mu = \mu_{opt}$ where $f(\mu_{opt}) = 0$. At $\mu = \mu_{opt}$, the solution to the problem defined in (4.17) would be the desired OWFS.

The effect of μ on α^2 , β^2 and $\alpha^2\beta^2$ is demonstrated in Fig. 4.1 for $B = 1/16$ and $M = 4$. It can be observed that α^2 increases and β^2 decreases with increase in μ , and $\alpha^2\beta^2$ has only one maximum. The value of μ for which equal energy concentration ($\alpha^2 = \beta^2$) in both domains are achieved, has been denoted as μ_{eq} . In Fig. 4.1(a), the OWFS of length $N = 16$ is considered, for which μ_{opt} and μ_{eq} are found to be 0.437 and 0.365, respectively. For $N = 128$, the maximum value of $\alpha^2\beta^2$ and equal concentration ($\alpha^2 = \beta^2$) are achieved for $\mu_{opt} = 0.499$ and $\mu_{eq} = 0.497$, respectively as shown in Fig. 4.1(b). As the value of N increases, both μ_{opt} and μ_{eq} approach to $\mu = 0.5$. Ideally, as $N \rightarrow \infty$, both converge to $\mu = 0.5$ (see Theorem 1 in APPENDIX).

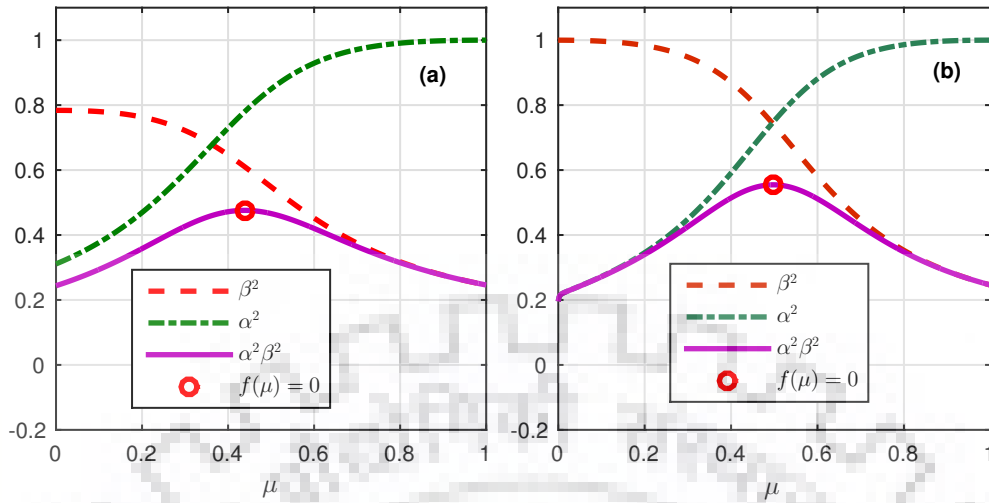


Fig. 4.1: Variation of α^2 , β^2 and $\alpha^2\beta^2$ with μ for (a) $B = 1/16$, $M = 4$ and $N = 16$ with $\mu_{\text{opt}} = 0.437$ and $\mu_{\text{eq}} = 0.365$; (b) $B = 1/16$, $M = 4$ and $N = 128$ with $\mu_{\text{opt}} = 0.497$ and $\mu_{\text{eq}} = 0.497$

4.4 Upper Bound of Achievable α^2 and β^2 for Finite Length Sequences

For given M and B , in case of simultaneously concentrated DPSS which is of infinite length, the region of attainable α^2 and β^2 is given by the intersection of unit square $0 \leq \alpha \leq 1$, $0 \leq \beta \leq 1$ and elliptical arc (4.7) [57]. Unity concentration in one domain is achieved at two intersection points given by $(\alpha, \beta) = \left(1, \sqrt{\lambda_0(M, B)}\right)$ and $(\sqrt{\lambda_0(M, B)}, 1)$.

In contrast to infinite length simultaneously concentrated DPSS, for finite length sequences, the achievable β^2 need not necessarily be 1 for any α^2 but rather depends on window support N and frequency interval B . The maximum achievable β^2 for a sequence of length N can be obtained by maximizing $\mathbf{w}^T \mathbf{A}^{(B, N)} \mathbf{w}$ subject to $\mathbf{w}^T \mathbf{w} = 1$ without any constraint on α^2 . The optimal solution is the maximum eigenvector of matrix $\mathbf{A}^{(B, N)}$ and the maximum achievable β^2 is equal to the maximum eigenvalue, λ_0^N . Therefore, the upper bound of attainable α^2 and β^2 is represented by intersection of rectangle $0 \leq \alpha^2 \leq 1$, $0 \leq \beta^2 \leq \lambda_0^N$ and the Pareto-optimal front obtained by solving (4.16). The intersection points of Pareto-optimal front and rectangle ($0 \leq \alpha^2 \leq 1$, $0 \leq \beta^2 \leq \lambda_0^N$) corresponding to $\mu \rightarrow 0$ and $\mu \rightarrow 1$ are discussed as follows:

The trade-off between α^2 and β^2 operates between two extrema corresponding to $\mu = 0$ and $\mu = 1$.

As $\mu \rightarrow 0$, (4.19) reduces to

$$\mathbf{A}^{(B,N)} \mathbf{w}_0^{(\mu=0)} = \lambda_0^{(\mu=0)} \mathbf{w}_0^{(\mu=0)} \quad (4.29)$$

where $\mathbf{w}_0^{(\mu=0)}$ is the eigenvector of $\mathbf{A}^{(B,N)}$ corresponding to maximum eigenvalue $\lambda_0^{(\mu=0)}$. $\mathbf{w}_0^{(\mu=0)}$ represents the time-limited N -length DPSS with maximum achievable $\beta^2 = \lambda_0^{(\mu=0)}$. Theoretically, $\beta^2 = 1$ can not be achieved in the given frequency interval for a finite length window. However, for large values of N , $\beta^2 \approx 1$ (see Appendix).

As $\mu \rightarrow 1$, (4.19) reduces to

$$\mathbf{T}^{(M,N)} \mathbf{w}_0^{(\mu=1)} = \lambda_0^{(\mu=1)} \mathbf{w}_0^{(\mu=1)} \quad (4.30)$$

where $\mathbf{w}_0^{(\mu=1)}$ is the eigenvector of $\mathbf{T}^{(M,N)}$ corresponding to maximum eigenvalue $\lambda_0^{(\mu=1)}$. Since the maximum eigenvalue of $\mathbf{T}^{(M,N)}$ is $\lambda_0^{(\mu=1)} = 1$, it can be inferred that

$$\mathbf{T}^{(M,N)} \mathbf{w}_0^{(\mu=1)} = \mathbf{w}_0^{(\mu=1)} \text{ where } \mathbf{w}_0^{(\mu=1)} = \begin{bmatrix} \mathbf{0}_{(N-M)/2} \\ \mathbf{w}_0^{(M)} \\ \mathbf{0}_{(N-M)/2} \end{bmatrix} \quad (4.31)$$

$\mathbf{0}_{(N-M)/2}$ represents a null vector of length $(N-M)/2$ and $\mathbf{w}_0^{(M)}$ is a M -length vector that represents M non-zero elements of vector $\mathbf{w}_0^{(\mu=1)}$. Pre-multiplying (4.19) with $\mathbf{T}^{(M,N)}$ and rearranging the result, leads to

$$\mathbf{T}^{(M,N)} \mathbf{A}^{(B,N)} \mathbf{w}_0 = \frac{\lambda_0 - \mu}{1 - \mu} \mathbf{T}^{(M,N)} \mathbf{w}_0 \quad (4.32)$$

As $\mu \rightarrow 1$, (4.32) can be rearranged using (4.31) as

$$\mathbf{T}^{(M,N)} \mathbf{A}^{(B,N)} \mathbf{T}^{(M,N)} \mathbf{w}_0^{(\mu=1)} = \frac{\lambda_0^{(\mu=1)} - \mu}{1 - \mu} \mathbf{T}^{(M,N)} \mathbf{w}_0^{(\mu=1)} \quad (4.33)$$

Using (4.31) and (4.33), it can be inferred that

$$\mathbf{A}^{(B,M)} \mathbf{w}_0^{(M)} = \lambda_0^{(M)} \mathbf{w}_0^{(M)} \quad (4.34)$$

$\mathbf{w}_0^{(M)}$ is a M length eigenvector of matrix $\mathbf{A}^{(B,M)}$ corresponding to eigenvalue $\lambda_0^{(M)}$ where the matrix $\mathbf{A}^{(B,M)}$ can be defined as a sub matrix of $\mathbf{A}^{(B,N)}$ as

$$[\mathbf{A}^{(B,M)}]_{p,q} = [\mathbf{A}^{(B,N)}]_{p+\lfloor \frac{N}{2} \rfloor - \lfloor \frac{M}{2} \rfloor, q+\lfloor \frac{N}{2} \rfloor + \lfloor \frac{M}{2} \rfloor - 1}$$

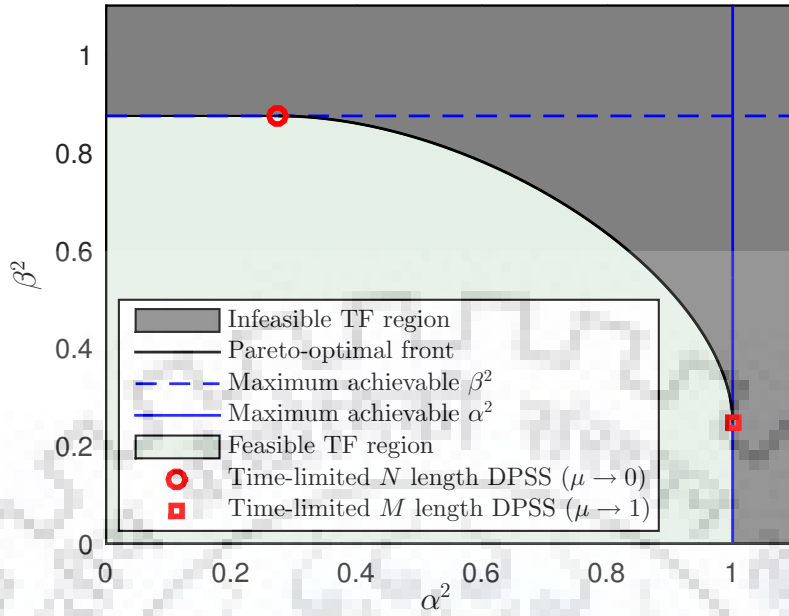


Fig. 4.2: Upper bound of achievable time and frequency domain energy concentration for finite length sequences for $M = 4$ and $N = 20$

for $p, q = 1, 2, \dots, M$. This can also be verified as

$$\begin{aligned} \lambda_0^{(M)} &= \left. \frac{\lambda_0^{(\mu=1)} - \mu}{1 - \mu} \right|_{\mu \rightarrow 1} \\ &= 1 - \left. \frac{d\lambda_0^{(\mu=1)}}{d\mu} \right|_{\mu \rightarrow 1} \quad (\text{L'Hospital's rule}) \end{aligned} \quad (4.35)$$

Using (7.9) and (4.31), (4.35) can be rewritten as

$$\begin{aligned} \lambda_0^{(M)} &= \left(\mathbf{w}_0^{(\mu=1)} \right)^T \mathbf{A}^{(B,N)} \mathbf{w}_0^{(\mu=1)} \\ &= \left(\mathbf{w}_0^{(M)} \right)^T \mathbf{A}^{(B,M)} \mathbf{w}_0^{(M)} \end{aligned} \quad (4.36)$$

Thus, as $\mu \rightarrow 1$, the solution to the problem defined in (4.17) converges to a M -length DPSS denoted by $\mathbf{w}_0^{(M)}$, with maximum achievable $\beta^2 = \lambda_0^{(M)}$.

In Fig. 4.2, the feasible region for time and frequency domain energy concentration is shown. It can be obtained by intersection of rectangle $0 \leq \alpha^2 \leq 1, 0 \leq \beta^2 \leq \lambda_0^N$, and the Pareto-optimal front obtained by solving (4.16). The Pareto-optimal front is obtained for $M = 4, B = 1/16$ and $N = 20$. The two extrema of the Pareto-optimal front corresponding to $\mu \rightarrow 0$ and $\mu \rightarrow 1$, shown in Fig 4.2, represent the energy concentrations obtained with time limited DPSS of length N and M , respectively.

In Fig. 4.3(a), the upper bounds obtained with proposed OWFS are plotted for $N = 20$ and different values of M and B . It can be inferred from the figure that as M or B

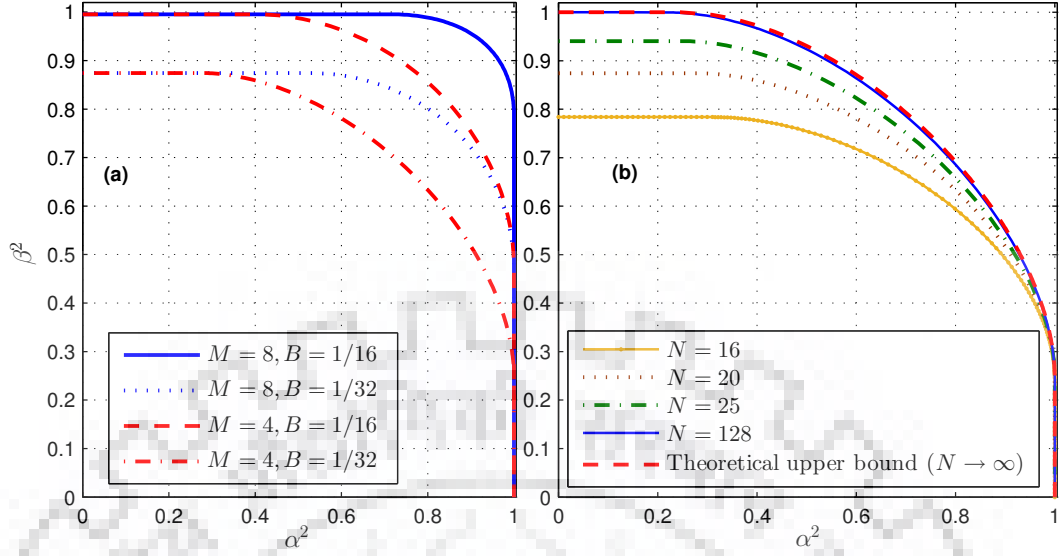


Fig. 4.3: Upper bound of achievable time and frequency domain energy concentration for finite length sequences for (a) $N = 20$ and different values of M and B ; (b) $M = 4$, $B = 1/16$, and different values of N

increases, the achievable α^2 (or β^2) increases for a given value of β^2 (or α^2). Also, the maximum achievable β^2 increases with increase in B . In Fig. 4.3(b), the upper bounds obtained with proposed OWFS are plotted for $M = 4$, $B = 1/16$ and different values of N . The bounds are also compared with theoretical upper-bound obtained with simultaneously concentrated DPSS in time interval $(-M/2, M/2)$ and frequency interval $(-B, B)$. It can be inferred that as N increases, the proposed upper bound approaches the theoretical bound. Ideally, as $N \rightarrow \infty$, the upper bound obtained with OWFS exactly matches with the theoretical upper bound of DPSS (see Theorem 1 in Appendix).

4.5 Performance Analysis

In this section, the proposed OWFS is compared with truncated DPSS and several commonly used windows.

4.5.1 Comparison with Truncated DPSS

For comparative analysis, this subsection introduces truncated version of simultaneously concentrated DPSS. The simultaneously concentrated DPSS can be obtained by linear combination of time limited and band limited DPSSs as

$$x[n] = (1 - p)\nu_\infty[n] + p\nu_M[n] \quad (4.37)$$

where p acts as a relative weighing factor. $\nu_\infty[n]$ represents zero order band limited DPSS. The time limited counterpart of $\nu_\infty[n]$, termed as time limited DPSS $\nu_M[n]$, is the maximum eigenvector of the matrix $\rho(M, B)$ defined as [57]

$$[\rho(M, B)]_{m,n} = \frac{\sin(2\pi B[m - n])}{\pi[m - n]} \quad (4.38)$$

for $m, n = 1, 2, \dots, M$. The truncated DPSS of length N denoted by $x_N[n]$, can be obtained by index limiting the ν_∞ to ν_N by solving the following equation [57]

$$\sum_{m=-M/2}^{M/2-1} \frac{\sin(2\pi B[n - m])}{\pi[n - m]} \nu_\infty[m] = \lambda_0(M, B) \nu_\infty[n] \quad (4.39)$$

for $n = -\lfloor N/2 \rfloor, -\lfloor N/2 \rfloor + 1, \dots, \lfloor N/2 \rfloor - 1$. $x_N(n)$ can be represented as $x_N[n] = (1 - p)\nu_N[n] + p\nu_M[n]$.

Fig. 4.4 compares the trade-off between α^2 and β^2 obtained from the proposed OWFS and simultaneously concentrated truncated DPSS for $M = 4$, $B = 1/16$ and $N = 20$. The achievable α^2 and β^2 for truncated DPSS is obtained by varying p from 0 to 1. It can be observed that the trade-off obtained with proposed OWFS coincides with achievable upper bound and covers all Pareto-optimal points. On the other hand, trade-off obtained with truncated DPSS deviates from the upper bound especially for lower values of α^2 (for $\alpha^2 \leq 0.6$). However, it converges to proposed window as p approaches 1 ($\alpha^2 \rightarrow 1$). It is also clear from analytical expression that both the proposed OWFS at $\mu \rightarrow 1$ and

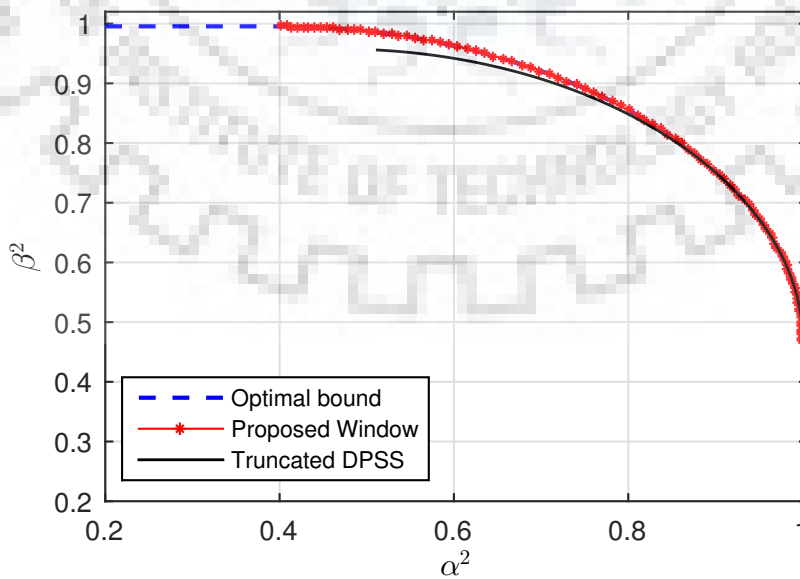


Fig. 4.4: Comparison of trade-off between α^2 and β^2 obtained with proposed OWFS and truncated DPSS

truncated DPSS at $p \rightarrow 1$ converge to time-limited M -length DPSS.

4.5.2 Comparison with Existing Well-known Windows

Fig. 4.5(a) compares the proposed OWFS with well known window functions in terms of maximum achievable α^2 and β^2 for $M = 4$ and $B = 1/16$. For windows having single parameter such as Hamming, Hanning, Blackman and Bartlett windows, the trade-off between α^2 and β^2 are obtained by varying the length of the window. On the other hand, for multi-parameter windows such as Gaussian, Dolph Chebyshev and Kaiser windows, the maximum achievable α^2 and β^2 for given M and B are obtained by grid search over window's parameter including window length. It can be observed that achievable trade-off curves of all well-known windows are strictly compliant with the derived upper bound. It is essentially justifying the capability of the proposed window to maximally concentrate the energy in narrow intervals in comparison to other window kernels. Fig. 4.5(b) compares all windows for $M = 4$ and $B = 1/8$. The achievable α^2 and β^2 for all kernels increase as compared to that of the previous case with $B = 1/16$. The trade-off curves shift closer to the upper bound. This is due to the fact that large time or frequency intervals allow more space to concentrate more energy in desired intervals, and achievable trade-off curves converge to rectangle ($0 \leq \alpha^2 \leq 1, 0 \leq \beta^2 \leq \lambda_0^N$).

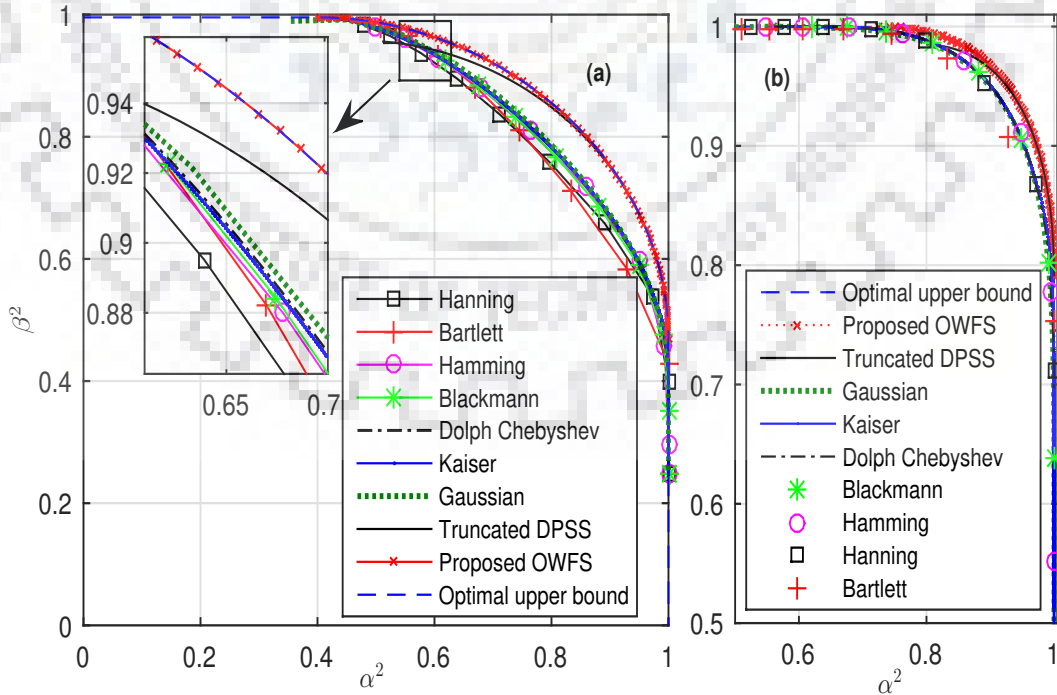


Fig. 4.5: Comparison of trade-off between α^2 and β^2 obtained with proposed OWFS and different windows for (a) $B = 1/16$; (b) $B = 1/8$

4.6 Extension of Proposed Work to Discrete Frequency Domain

The discrete FT (DFT) of the window \mathbf{w} can be represented as $\mathbf{w}^f = \left(w_k^f \right)_{k=-\lfloor N/2 \rfloor}^{\lceil N/2 \rceil - 1}$ where $w_k^f = \frac{1}{N} (\mathbf{w}^T \mathbf{d}_k)$ and $\mathbf{d}_k = \left(e^{-\frac{j2\pi k(-\lfloor N/2 \rfloor)}{N}}, e^{-\frac{j2\pi k(-\lfloor N/2 \rfloor + 1)}{N}}, \dots, e^{-\frac{j2\pi k(\lceil N/2 \rceil - 1)}{N}} \right)^T$. β^2 in a frequency interval $(-\lfloor L/2 \rfloor, \lceil L/2 \rceil - 1)$ can be defined as

$$\beta^2 = \frac{\sum_{k=-\lfloor L/2 \rfloor}^{\lceil L/2 \rceil - 1} |w_k^f|^2}{\sum_{k=-\lfloor N/2 \rfloor}^{\lceil N/2 \rceil - 1} |w_k^f|^2} \quad (4.40)$$

The numerator of (4.40) can be rephrased as

$$\sum_{k=-\lfloor L/2 \rfloor}^{\lceil L/2 \rceil - 1} |w_k^f|^2 = \frac{1}{N} \mathbf{w}^H \mathbf{B}^{(L,N)} \mathbf{w} \quad (4.41)$$

where $\mathbf{B}^{(L,N)} = \frac{1}{N} \sum_{k=-\lfloor L/2 \rfloor}^{\lceil L/2 \rceil - 1} \mathbf{d}_k \mathbf{d}_k^T$ is an $N \times N$ positive semi-definite matrix. The $(m, n)^{th}$ element of the matrix $\mathbf{B}^{(L,N)}$ is given by

$$\begin{aligned} [\mathbf{B}^{(L,N)}]_{m,n} &= \frac{1}{N} \sum_{k=-\lfloor L/2 \rfloor}^{\lceil L/2 \rceil - 1} e^{\frac{j2\pi k(-\lfloor N/2 \rfloor + m - 1)}{N}} e^{-\frac{j2\pi k(-\lfloor N/2 \rfloor + n - 1)}{N}} \\ &= \begin{cases} \frac{1}{N} \left(e^{\frac{j2\pi(m-n)}{N} \left(\frac{L}{2} - \lfloor \frac{L}{2} \rfloor - \frac{1}{2} \right)} \frac{\sin((m-n)(L\pi/N))}{\sin((m-n)(\pi/N))} \right), & m \neq n \\ \frac{L}{N}, & m = n \end{cases} \end{aligned} \quad (4.42)$$

For $L = N$, $\mathbf{B}^{(L,N)}$ becomes an identity matrix. Using (4.41) and (4.42), β^2 can be represented as

$$\beta^2 = \frac{\mathbf{w}^H \mathbf{B}^{(L,N)} \mathbf{w}}{\mathbf{w}^H \mathbf{w}} \quad (4.43)$$

The problem of simultaneous maximization of α^2 (4.14) and β^2 (4.43) can be defined similarly as defined in (4.16) with β^2 defined in (4.43). For a fixed value of μ , the solution to the problem is an eigenvector, $\mathbf{w}_{(0,D)}$, of matrix $(1 - \mu)\mathbf{B}^{(L,N)} + \mu\mathbf{T}^{(M,N)}$ corresponding to the maximum eigenvalue $\lambda_{(0,D)}$. Thus $\mathbf{w}_{(0,D)}$ satisfies,

$$\left((1 - \mu)\mathbf{B}^{(L,N)} + \mu\mathbf{T}^{(M,N)} \right) \mathbf{w}_{(0,D)} = \lambda_{(0,D)} \mathbf{w}_{(0,D)} \quad (4.44)$$

Since $\mathbf{B}^{(L,N)} \mathbf{B}^{(L,N)} = \mathbf{B}^{(L,N)}$ (see Lemma 3 in Appendix for proof), by using similar steps as in Theorem 1 (see Appendix), it can be proved that the achievable energy con-

centrations in this discrete time discrete frequency case fall on the elliptical arc

$$\alpha^2 + \beta^2 - 2\alpha\beta\sqrt{\lambda_{(0,D)}^{(M)}} = 1 - \lambda_{(0,D)}^{(M)} \quad (4.45)$$

where $\lambda_{(0,D)}^{(M)}$ is the maximum eigenvalue of $M \times M$ matrix $\mathbf{B}^{(L,M)}$ which can be defined as a subset of the matrix $\mathbf{B}^{(L,N)}$ as

$$[\mathbf{B}^{(L,M)}]_{p,q} = [\mathbf{B}^{(L,N)}]_{p+\lfloor \frac{N}{2} \rfloor - \lfloor \frac{M}{2} \rfloor, q+\lfloor \frac{N}{2} \rfloor + \lfloor \frac{M}{2} \rfloor - 1}$$

for $p, q = 1, 2, \dots, M$. $\lambda_{(0,D)}^{(M)}$ is upper bounded by the inequality [155]

$$\begin{aligned} \left(\lambda_{(0,D)}^{(M)}\right)^2 &\leq \min_{1 \leq m \leq M} \sum_{n=1}^M \left| [\mathbf{B}^{(L,M)}]_{m,n} \right| \\ &\leq \left(\frac{1}{N}\right) \min_m \sum_{n=1}^M L = \frac{ML}{N} \end{aligned} \quad (4.46)$$

where $ML \leq N$. From (4.46) it is understood that the achievable α^2 and β^2 are characterized by $\lambda_{(0,D)}^{(M)}$. Hence, this upper bound provides a good intuitive understanding of the impact of M , L and N on achievable α^2 and β^2 . For a fixed value of N , decreasing the value of M or L decreases the maximum achievable α^2 and β^2 which is illustrated in Fig. 4.6(a). The upper bounds for attainable α^2 and β^2 are plotted for $N = 20$ and different values of M and L . It can be inferred that as M or L decreases the achievable α^2 (or β^2) decreases for a given value of β^2 (or α^2). In the discrete time discrete frequency scenario we can achieve $\beta^2 = 1$ which is also evident from Fig. 4.6(a). In Fig. 4.6(b), the upper

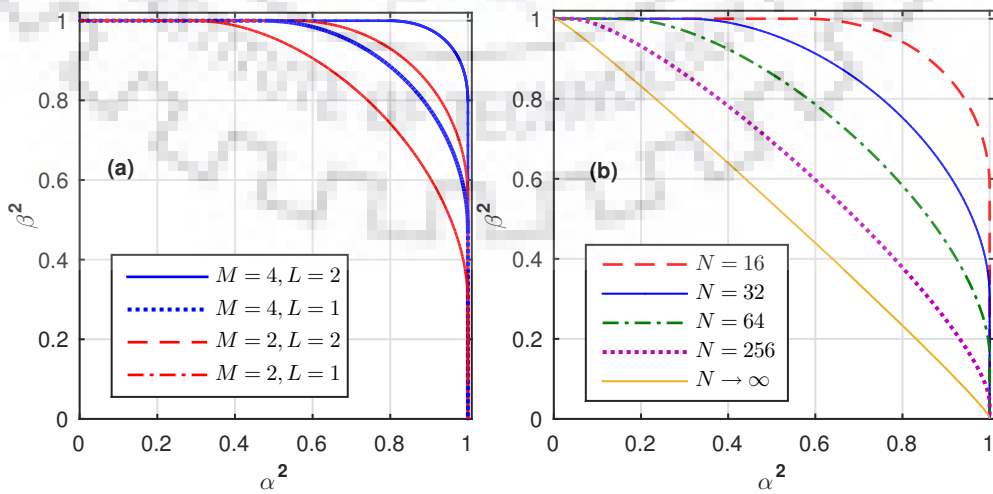


Fig. 4.6: Trade-off between α^2 and β^2 obtained with OCDW for (a) $N = 20$ and different values of M and L ; (b) $M = 2, L = 2$, and different values of N

bounds for attainable α^2 and β^2 are plotted for $M = 2$, $L = 2$ and different values of N . For a fixed value of M and L , the trade-off curves between α^2 and β^2 approach towards linear line as N approaches infinity. It is also evident from the upper bound derived in (4.46) that as $N \rightarrow \infty$, $\lambda_{(0,D)}^{(M)}$ approaches 0, and hence (4.45) reduces to $\alpha^2 + \beta^2 = 1$.

4.7 Application of Optimally Concentrated Window with Finite Support in Time-Frequency Analysis

In TFA, the IF estimation is a fundamental concept. It represents the instantaneous rate of change of phase of the signal. IF estimation based on TFA involves finding the peaks of the magnitude of TFR. Therefore, it is desired to design a highly concentrated TFR which can follow signal IF law correctly. Hence, numerous recent researches are focused on adaptive TFRs whose parameters are adapted according to signal. Adaptive STFT (ASTFT) [156], adaptive ST [128], adaptive WVD [157], etc. are some well known TFRs in this category.

Authors in [34], [156] and [158], have proposed variants of ASTFT which adapt the window width based on the chirp rate of the signal (first derivative of the IF). First, a preliminary TFR (PTFR) is constructed to make rough IF estimate by detecting the ridges of the TFR, and thereafter the chirp rate, defined as the first derivative of the IF, is computed. Finally, the chirp rate is used for adapting the window width, and thereby the final TFR is obtained. In [156], WT is used as the PTFR and the difference operator is used for chirp rate calculation. The window width is adapted at each time instant based on the chirp rate. Herein, this approach is represented as ASTFT-t. The conventional ST [9] uses a Gaussian window whose width varies inversely proportional to frequency. Many variants of ST have been proposed in literature which modify the scaling criterion in conventional ST [159]. In [128], the authors have suggested to remove any unnecessary constraint on choosing the window width, and instead adapt the window width at each frequency based on concentration measure (CM). This approach can also be considered as a form of ASTFT with frequency dependent window. Herein, it is represented as ASTFT-f. It is suggested in [34] that the WT used as PTFR in [156] is not signal dependent, and the difference operator used for calculating the chirp rate is sensitive to IF estimation error. Moreover, the window width is dependent only on time, and the relationship between the window width and the chirp rate is not accurate enough. Therefore, authors in [34] have modified the approach used in [156] by using a CM-based ASTFT as PTFR, and further used principal component analysis (PCA) for chirp rate calculation. A more accurate relationship between window width and chirp rate derived by Cohen is used to adapt the window width at each TF point in the TFR. Herein, this variant is represented

as ASTFT-tf. It is mentioned in [158] that in case of multicomponent signal and in noisy environment, the CM-based methods favor the slow-varying frequency component compared to the fast varying component. Therefore, to obtain the PTFR, the authors used regular rate which is the ratio between the effective bandwidth and effective time duration of the signal. IF estimates are smoothed by using simple moving average filter before applying the conventional difference operator for estimating the chirp rate. However, the accuracy of this process of chirp rate calculation is limited. The window width is adapted in TF domain using chirp rate and statistics such as bias and variance of the IF estimation error in noisy environment. Herein, this more generalized ASTFT approach is termed as GASTFT-tf.

The proposed OWFS carries importance on its own, and has the potential to replace other window functions where a high energy concentration is desired in narrow time and frequency intervals which is also evident in Fig. 5. For simulation results, the performances of ASTFT-t, ASTFT-f, ASTFT-tf and GASTFT-tf are compared with GASTFT-tf using OWFS. Herein, GASTFT-tf using OWFS is termed as OASTFT-tf. For calculating the chirp rate, PCA is used in ASTFT-t, GSTFT-tf and OASTFT-tf as it is less sensitive to IF estimation error. In case of OASTFT-tf, the relationship between the regular rate and window width parameters M and B can be represented as $\frac{B}{M} = \frac{\nu_0}{2N}$, where ν_0 represents regular rate [158] and N is the length of the signal. Through simulation, it is found that more than 99% of energy is captured within a TF box of area $BM = 2/N$. Accordingly, M and B are calculated, and the PTFR is obtained.

For simulation study, a multicomponent signal is considered in presence of additive white Gaussian noise (AWGN) of 18 dB. The multicomponent signal consists of a frequency modulated (FM) signal and a linear chirp. The noisy signal is shown in Fig. 4.7(a), and can be represented as

$$x(t) = \cos(200\pi t + 20 \cos(4\pi t)) + \cos(25\pi t + 20\pi t^2) + n(t)$$

where $n(t)$ represents the AWGN. The TFRs of ASTFT-t, ASTFT-f, ASTFT-tf, GSTFT-tf and OASTFT-tf are shown in Figs. 4.7(b), 4.7(c), 4.7(d), 4.7(e) and 4.7(f) respectively. It can be observed in Fig. 4.7 that the GASTFT-tf provides more concentrated TFR for both the components (linear chirp and FM) as compared to ASTFT-t, ASTFT-f and ASTFT-tf. The energy concentration is further improved by replacing the Gaussian window by OWFS as shown in the TFR of OASTFT-tf.

Instead of visual inspection, accuracy of IF estimate can provide more clarity on the performance of the TFRs. The normalized mean square error (NMSE) curves for the five TFRs illustrated in Fig. 4.7 are shown in Fig. 4.8. It can be concluded that OASTFT-tf provides more accurate IF estimate than that of other counterparts, and the improvement

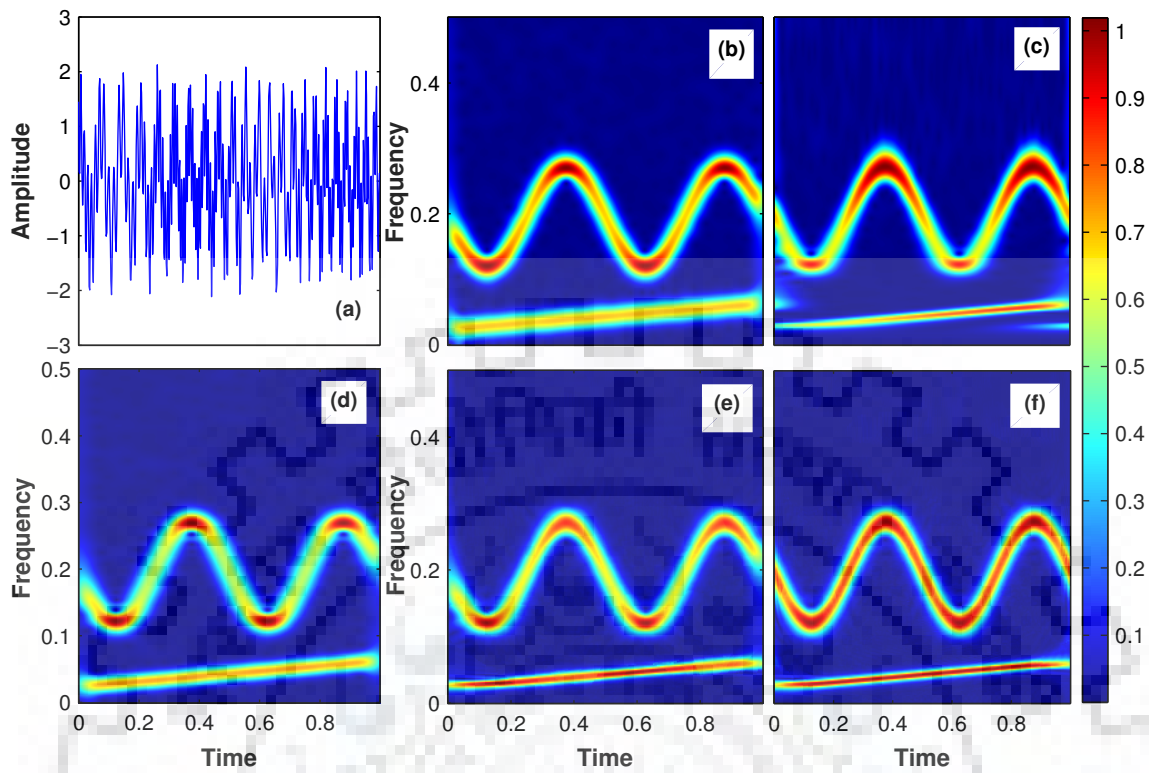


Fig. 4.7: Comparison of TFRs: (a) Synthetic signal composed of two components with AWGN (SNR = 18 dB); TFR of (b) ASTFT-t; (c) ASTFT-f; (d) ASTFT-tf; (e) GSTFT-tf; (f) OASTFT-tf

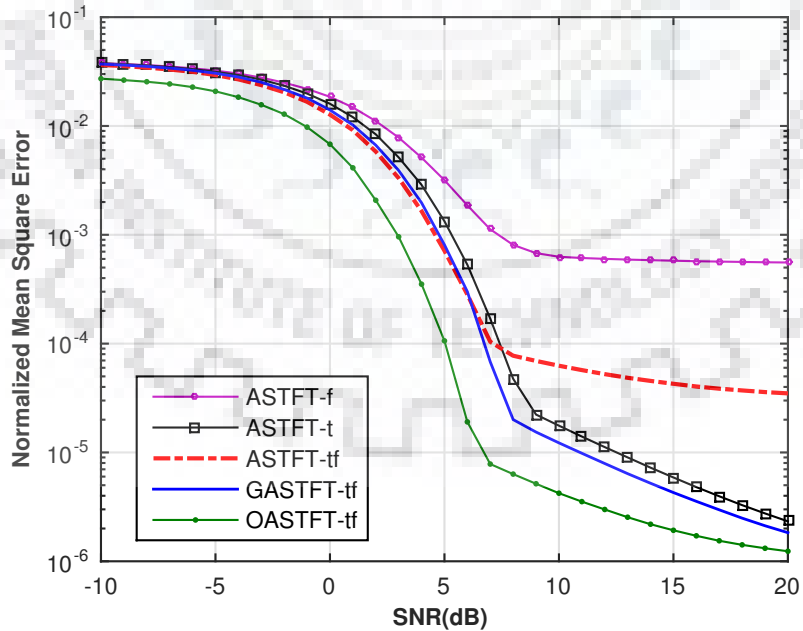


Fig. 4.8: Normalized mean square error in IF estimation based on different adaptive TFRs

in the IF estimate is more at low SNR.

4.8 Proposed Optimally Concentrated Discrete Window (OCDW)

In this section a novel OCDW is proposed based on a constraint optimization problem of maximization of the product of time and frequency domain energy concentrations in given discrete time discrete frequency intervals. Further, it is extended to design an OST for multi-resolution analysis. A new scaling criterion is also presented for OST which prevents unnecessary deterioration in frequency resolution at higher frequencies, and time resolution at lower frequencies.

In order to maximize the product of time (4.14) and frequency (4.43) domain energy concentrations *i.e.* $\alpha^2\beta^2$, the desired optimization problem can be formulated as

$$\max_{\mathbf{w}} (\mathbf{w}^H \mathbf{T}^{(M,N)} \mathbf{w})(\mathbf{w}^H \mathbf{B}^{(L,N)} \mathbf{w}) \quad (4.47)$$

$$\text{subject to } \mathbf{w}^H \mathbf{w} = 1 \quad (4.48)$$

Using Lagrangian method, the problem turns into

$$J(\mathbf{w}, \xi) = (\mathbf{w}^H \mathbf{T}^{(M,N)} \mathbf{w})(\mathbf{w}^H \mathbf{B}^{(L,N)} \mathbf{w}) + \xi(1 - \mathbf{w}^H \mathbf{w})$$

where ξ denotes the Lagrangian multiplier. By putting $\frac{\partial J(\mathbf{w}, \xi)}{\partial \mathbf{w}} = 0$, the optimality condition is

$$(\mathbf{w}^H \mathbf{T}^{(M,N)} \mathbf{w}) \mathbf{B}^{(L,N)} \mathbf{w} + (\mathbf{w}^H \mathbf{B}^{(L,N)} \mathbf{w}) \mathbf{T}^{(M,N)} \mathbf{w} = \xi \mathbf{w} \quad (4.49)$$

Since $\mathbf{B}^{(L,N)} \mathbf{B}^{(L,N)} = \mathbf{B}^{(L,N)}$, premultiplying (4.49) by $\mathbf{w}^H \mathbf{B}^{(L,N)}$ and $\mathbf{w}^H \mathbf{T}^{(M,N)}$, respectively leads to

$$\mathbf{w}^H \mathbf{T}^{(M,N)} \mathbf{w} + \mathbf{w}^H \mathbf{B}^{(L,N)} \mathbf{T}^{(M,N)} \mathbf{w} = \xi \quad (4.50)$$

$$\mathbf{w}^H \mathbf{B}^{(L,N)} \mathbf{w} + \mathbf{w}^H \mathbf{T}^{(M,N)} \mathbf{B}^{(L,N)} \mathbf{w} = \xi \quad (4.51)$$

Since $\mathbf{w}^H \mathbf{B}^{(L,N)} \mathbf{T}^{(M,N)} \mathbf{w} = (\mathbf{w}^H \mathbf{T}^{(M,N)} \mathbf{B}^{(L,N)} \mathbf{w})^*$,

$$\mathbf{w}^H \mathbf{T}^{(M,N)} \mathbf{w} = \mathbf{w}^H \mathbf{B}^{(L,N)} \mathbf{w} \quad (4.52)$$

Using (4.52), (4.49) can be rewritten as

$$(\mathbf{T}^{(M,N)} + \mathbf{B}^{(L,N)}) \mathbf{w} = \lambda \mathbf{w} \quad (4.53)$$

where $\lambda = \xi / \mathbf{w}^H \mathbf{T}^{(M,N)} \mathbf{w} = \xi / \mathbf{w}^H \mathbf{B}^{(L,N)} \mathbf{w}$. It can be inferred from (4.53) that the optimal solution \mathbf{w}_0 is an eigenvector of matrix $(\mathbf{T}^{(M,N)} + \mathbf{B}^{(L,N)})$ corresponding to maximum

eigenvalue λ_0 . \mathbf{w}_0 is the desired OCDW which satisfies $\alpha^2\beta^2 = \gamma^2$ and $\alpha^2 = \beta^2 = \gamma$, where $\gamma = \lambda_0/2$. For OCDW, premultiplying (4.53) by $\mathbf{T}^{(M,N)}$ and $\mathbf{B}^{(L,N)}$, respectively leads to

$$\mathbf{T}^{(M,N)}\mathbf{B}^{(L,N)}\mathbf{w}_0 = (\lambda_0 - 1)\mathbf{T}^{(M,N)}\mathbf{w}_0 \quad (4.54)$$

$$\mathbf{B}^{(L,N)}\mathbf{T}^{(M,N)}\mathbf{w}_0 = (\lambda_0 - 1)\mathbf{B}^{(L,N)}\mathbf{w}_0 \quad (4.55)$$

Using (4.55), (4.54) can be re-written as

$$\mathbf{T}^{(M,N)}\mathbf{B}^{(L,N)}\mathbf{T}^{(M,N)}\mathbf{w}_0 = (\lambda_0 - 1)^2\mathbf{T}^{(M,N)}\mathbf{w}_0 \quad (4.56)$$

$(\lambda_0 - 1)^2$ is the eigenvalue of matrix $\mathbf{B}^{(L,M)}$ where

$$[\mathbf{B}^{(L,M)}]_{m,n} = \begin{cases} [\mathbf{B}^{(L,N)}]_{m,n}, & 1 + \lfloor \frac{N}{2} \rfloor - \lfloor \frac{M}{2} \rfloor \leq m, n \leq \lfloor \frac{N}{2} \rfloor + \lfloor \frac{M}{2} \rfloor \\ 0, & \text{elsewhere} \end{cases}$$

An upper bound [155] on $(\lambda_0 - 1)^2$ can be found as

$$(\lambda_0 - 1)^2 \leq \min_{1 \leq m \leq M} \sum_{n=1}^M |[\mathbf{B}^{(L,M)}]_{m,n}| \quad (4.57)$$

$$\leq \left(\frac{1}{N}\right) \min_m \sum_{n=1}^M L = \frac{ML}{N} \quad (4.58)$$

where $ML \leq N$. Using this inequality and $\gamma = \lambda_0/2$, M and L can be chosen to satisfy

$$ML \geq N(2\gamma - 1)^2 \quad (4.59)$$

where equality only holds for $M = 1$ or $L = 1$.

Fig. 4.9 shows the trade-off between minimum possible time and frequency intervals (M, L) for various values of γ . M and L increase with increase in γ . Fig. 4.9 also verifies the validity of theoretical lower bound defined in (4.59). For $\gamma \leq 0.9$, the theoretical bound closely matches with simulated curves. For $\gamma > 0.9$, simulated curves deviate from theoretical bound. Therefore, for $\gamma \leq 0.9$, (4.59) can be used for selecting desired L and M .

The proposed OCDW is shown in time and frequency domain in Figs. 4.10(a) and 4.10(b), respectively, for $M = 15$ and different values of γ . Minimum value of L is chosen for desired γ . Increasing the value of γ results in wider mainlobe in frequency domain. It is because the OCDW requires larger L to accommodate higher energy concentration. This additional parameter γ provides extra degree of freedom to optimize the concentra-

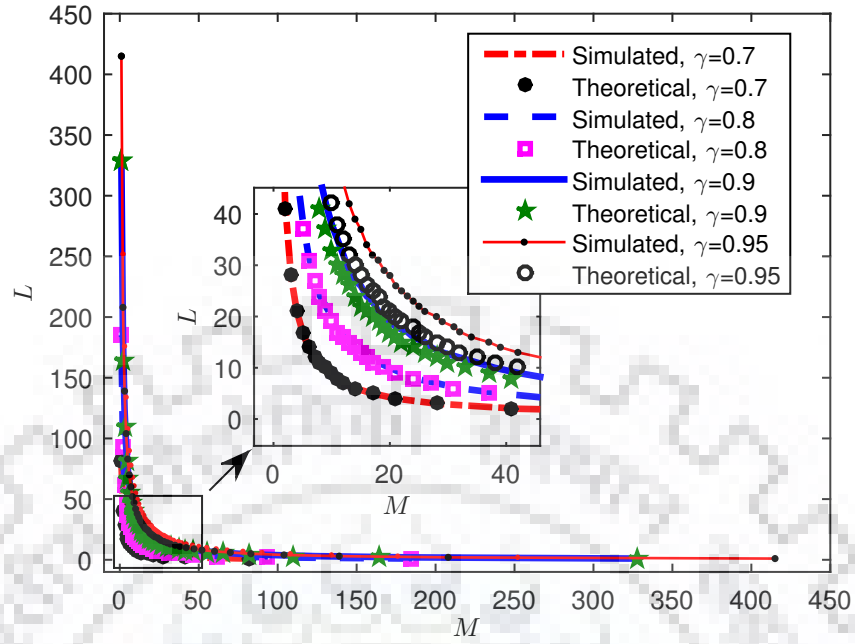


Fig. 4.9: Selection of time and frequency intervals (M, L) for different values of γ and $N = 512$

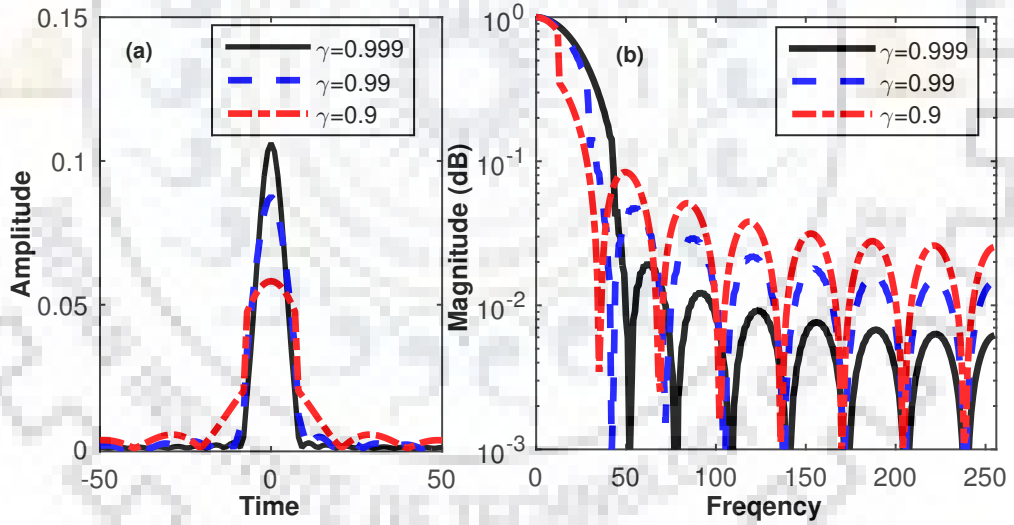


Fig. 4.10: Proposed OCDW for $M = 15$ and different values of γ in (a) Time domain; (b) Frequency domain

tion of TFR. To summarize, higher γ means wider mainlobe but lesser sidelobes, whereas lower γ results in narrower mainlobe but higher sidelobes.

Table 4.1 compares the OCDW with Gaussian window (GW) and Dolph-Chebyshev window (DCW) in terms of achievable $\alpha^2\beta^2$ for given M and L . In case of GW and DCW, the window parameters are varied heuristically to determine maximum achievable $\alpha^2\beta^2$. It is observed that OCDW outperforms GW and DCW. The difference in performance is larger for smaller intervals *i.e.* the OCDW is beneficial for concentrating energy in narrow

Table 4.1: Comparison of windows in terms of $\alpha^2\beta^2$

Parameters	GW	DCW	OCDW
$M = L = 8$	0.2199	0.2169	0.4575
$M = L = 16$	0.6236	0.6128	0.7091
$M = L = 32$	0.9757	0.9631	0.9906

time and frequency intervals. The proposed OCDW could be extended to design the kernel for any TFA techniques such as STFT, WT, ST, etc. As a case study, the proposed window is extended to design a variant of ST.

4.8.1 Proposed OCDW based ST (OST)

By extending the proposed OCDW, $w_0 = (w_{0,k})_{k=-\lfloor N/2 \rfloor}^{\lceil N/2 \rceil - 1}$, the frequency dependent normalized OCDW and the OCDW based ST (OST) can be represented as

$$\varphi[k, n] = \frac{w_{0,k}^{(M_n, L_n)}}{\sum_{k=-\lfloor N/2 \rfloor}^{\lceil N/2 \rceil - 1} w_{0,k}^{(M_n, L_n)}}$$

$$S^\varphi[j, n] = \sum_{m=-\lfloor N/2 \rfloor}^{\lceil N/2 \rceil - 1} X[m + n] \Psi[m, n] e^{i2\pi \frac{m}{N} j} \quad (4.60)$$

where subscript n in M_n and L_n represents the dependency of time and frequency intervals on frequency as desired for multiresolution analysis. $\Psi[m, n]$ represents the FT of the normalized OCDW. For a desired value of γ , M_n and L_n can be selected as

$$M_n = \left\lceil \frac{\kappa N}{n} \right\rceil, \quad L_n = \left\lceil \frac{N}{M_n} (2\gamma - 1)^2 \right\rceil \quad (4.61)$$

where κ is the scaling parameter. The selection of M_n using (4.61) provides scaling similar to conventional ST [9]. The other existing scaling criteria are also applicable for the OCDW based ST.

4.8.2 Proposed Fair Scaling Criterion for OST

Existing scaling approaches are unable to provide a fair trade-off between time and frequency domain resolution. Therefore, a new scaling criterion is proposed to maintain fairness between time and frequency domain window widths in conventional ST. For comparison purpose, the time and frequency domain widths of the Gaussian window in conventional ST is denoted as σ_T and σ_F , respectively. Further, the proposed scaling criterion is adopted in OST.

Fig. 4.11 illustrates the selection of (σ_T, σ_F) in proposed scaling. To achieve desired fairness criteria, scaling parameters (σ_T, σ_F) are chosen at the intersection of a hyperbolic arc and straight lines as shown in Fig. 4.11. The hyperbolic arc denotes the relationship between σ_T and σ_F of the Gaussian window which can mathematically be represented as

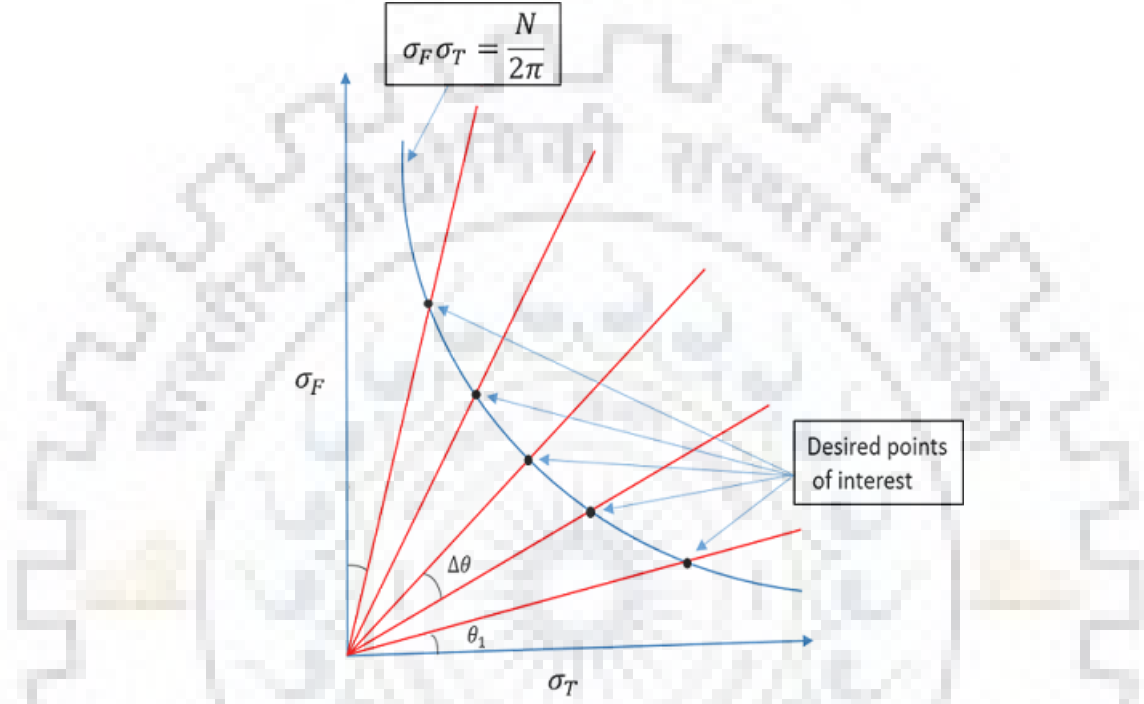


Fig. 4.11: Proposed scaling: Approach for selecting time and frequency domain SD (σ_T) and (σ_F), respectively

$$\sigma_T \sigma_F = N/2\pi \quad (4.62)$$

The straight lines in Fig. 4.11 can be expressed as

$$\sigma_F = \sigma_T \tan(\theta_n) \quad (4.63)$$

To obtain desired fair scaling, θ_n is varied uniformly as

$$\theta_n = \theta_1 + \frac{\theta_2 - \theta_1}{N/2 - 1}(n - 1) \quad (4.64)$$

where $\theta_2 = \pi/2 - \theta_1$. By solving (4.63) and (4.64), the desired σ_T and σ_F are obtained. θ_1 in (4.64) determines the time and frequency domain window width at minimum ($n = 1$) and maximum ($n = N/2$) frequencies. A suitable value of θ_1 can be chosen to control unnecessary time spreading at lower frequencies, and frequency spreading at higher frequencies.

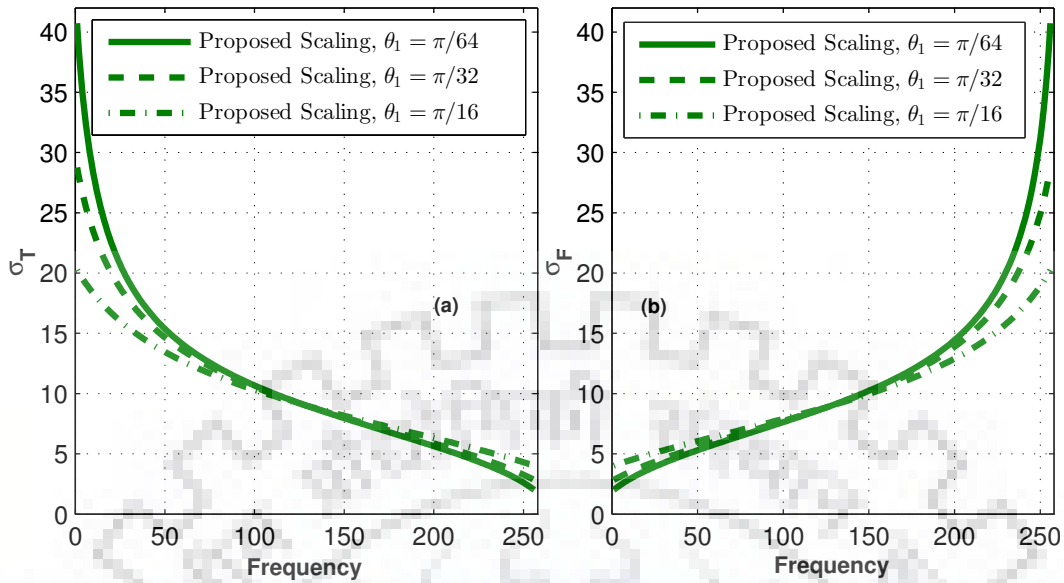


Fig. 4.12: Proposed scaling: SD of GW for $N = 512$ in (a) Time domain; (b) Frequency domain

The variation of σ_T and σ_F with frequency in time and frequency domain according to proposed scaling criteria are illustrated in Fig. 4.12. A fair trade-off between σ_T and σ_F can be observed. As σ_F increases with frequency, σ_T decreases with the same rate. Fig. 4.12 also shows the variation of σ_T and σ_F at different values of θ_1 . By varying θ_1 , the window width at most of the mid-range frequencies is not varying. The major differences are observed at lower and higher frequencies as θ_1 determines the window width at low and higher frequencies.

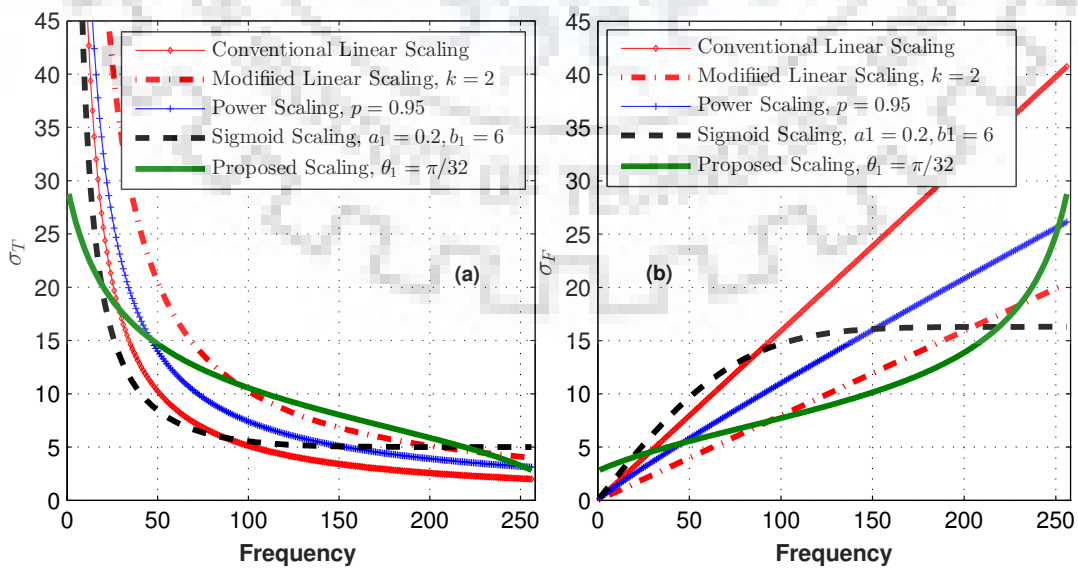


Fig. 4.13: Comparison of scaling criteria: SD of GW for length $N = 512$ in (a) Time domain; (b) Frequency domain

In Fig. 4.13, the proposed scaling criterion is compared with the other existing scaling criteria. The proposed scaling provides a fair trade-off between time and frequency domain window width profile. The proposed scaling provides smaller windows for most of the frequencies in the frequency domain as compared to other scaling criteria, which leads to better frequency resolution for most of the frequencies and also avoids the unnecessary deterioration in frequency resolution at higher frequencies. Compared to other scaling criteria, the window width in the proposed approach is wider in the frequency domain for lower frequencies, and hence provides better time resolution for lower frequencies.

To incorporate the proposed fair scaling (FS) criterion in the proposed OST, M_n and L_n are chosen as

$$M_n = \left\lceil \frac{\sqrt{N}(2\gamma - 1)}{\sqrt{\tan(\theta_n)}} \right\rceil, L_n = \left\lceil \sqrt{N}(2\gamma - 1)\sqrt{\tan(\theta_n)} \right\rceil \quad (4.65)$$

where

$$\theta_n = \tan^{-1} \left(\frac{k_5^2}{N(2\gamma-1)^2} \right) + \left(\frac{4 \tan^{-1}((N/k_5^2)(2\gamma-1)^2) - \pi}{N-2} \right) (n-1)$$

k_5 is a parameter that determines M and L at minimum ($n = 1$) and maximum ($n = \lceil N/2 \rceil$) frequencies *i.e.* $L_1 = M_{\lceil N/2 \rceil} = k_5$. A suitable value of k_5 can avoid unnecessary spreading at lower frequencies and shortening at higher frequencies.

Fig. 4.14 compares the width of GW and OCDW using CLS. In case of GW, for desired concentration γ , the equivalent M_n and L_n are chosen as $\sqrt{2}T^{-1} \left(\frac{1-\gamma}{2} \right) \sigma_t[n]$ and

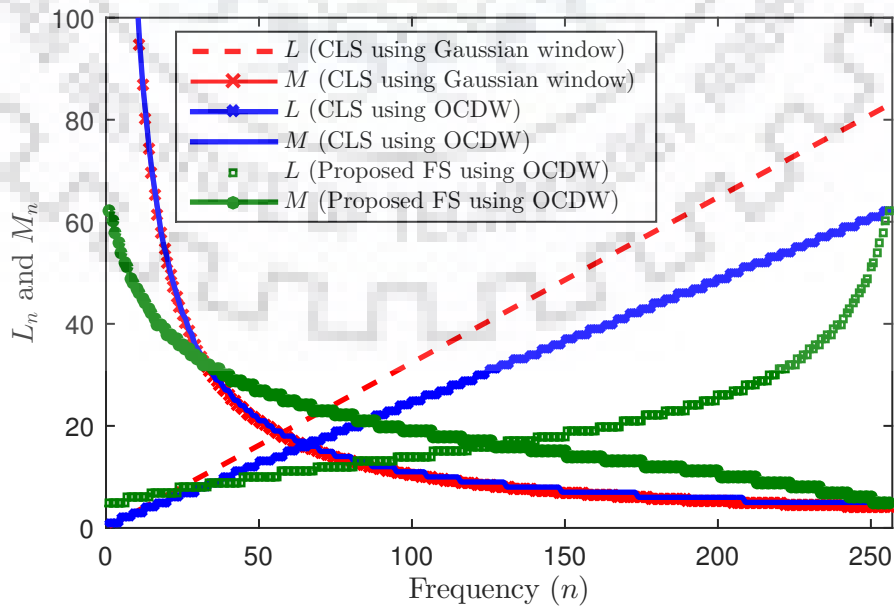


Fig. 4.14: Comparison of scaling criteria used in GW based ST and proposed OST for $N = 512$ and $\gamma = 0.9$

$\sqrt{2}\mathbf{T}^{-1}\left(\frac{1-\gamma}{2}\right)\sigma_f[n]$, respectively. $\mathbf{T}^{-1}(\cdot)$ represents the inverse Q -function. For fair comparison, $\kappa = \sqrt{2}\mathbf{T}^{-1}\left(\frac{1-\gamma}{2}\right)$ is chosen in (4.61) to ensure the same time domain intervals for both OCDW and GW. The corresponding frequency intervals are narrower in OCDW as compared to GW. Fig. 3 also illustrates the proposed FS given in (4.65) for $k_5 = 2\kappa$. It provides fair trade-off between time and frequency intervals unlike CLS. It also avoids unnecessary window width shortening in time, and spreading in frequency for lower and higher frequencies, respectively.

In order to evaluate the efficacy of the proposed OCDW and scaling criteria, a synthetic signal with multiple power quality disturbances is considered in Fig. 4.15. The signal is synthesized with sampling frequency of 3.2 KHz and duration of $t = 0.2$ sec as per the IEEE 1159 standards [120]. The signal consists of voltage interruption, oscillatory transient and odd harmonic components upto seventh order along with fundamental frequency component of 50 Hz. The magnitudes of fundamental frequency component, third, fifth and seventh harmonic components are 1, 0.9, 0.7 and 0.5 pu, respectively. The

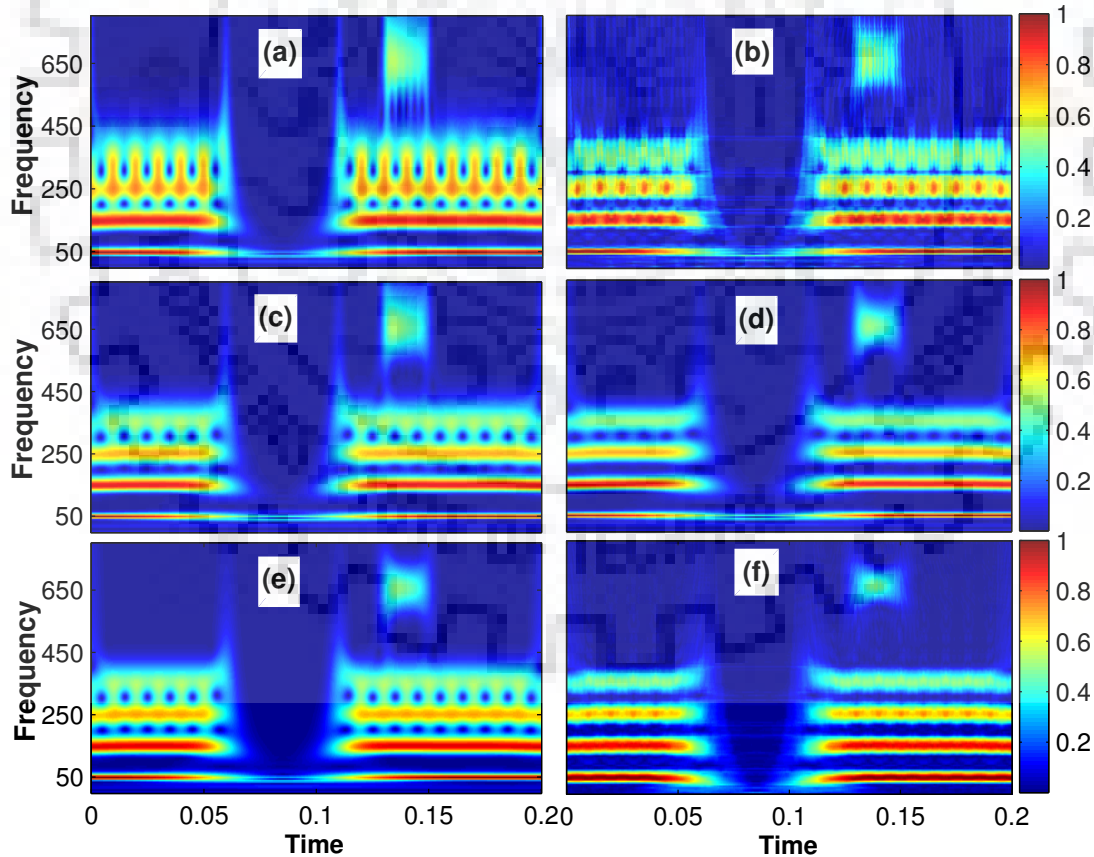


Fig. 4.15: Comparison of amplitude spectra of TFRs: (a) ST using CLS; (b) Proposed OST using CLS for $\gamma = 0.9$ and $\kappa = 2.3262$; ST with (c) MLS [20] for $k = 2$; (d) PS [39] for $p = 0.85$; (e) SS [105] for $a = 0.2$ and $b = 6$; (f) OST with proposed FS with $\gamma = 0.9$ and $k_5 = 10$

Table 4.2: Comparison of TFRs shown in Fig. 4.15 in terms of CM

	ST				OST	
	CLS	MLS	PS	SS	CLS	FS
CM	0.1341	0.14	0.143	0.1379	0.1423	0.1503

duration of voltage interruption is from $t = 0.06$ sec to $t = 0.11$ sec. The duration of transient is from $t = 0.13$ sec to $t = 0.15$ sec. TFR of ST using CLS shown in Fig. 4.15(a) indicates that harmonic components are not distinguishable, especially fifth and seventh harmonics are completely merged. The frequency resolution of oscillatory transient is poor. Due to very poor time resolution for lower frequencies, the voltage interruption is also not detectable. In the TFR of proposed OST using CLS (4.61) shown in Fig. 4.15(b), all disturbances are clearly visible and distinguishable. In the TFR of ST using MLS [20] shown in Fig. 4.15(c), the frequency resolution has improved as compared to CLS, but at the cost of degradation in time resolution of voltage interruption. The fifth and seventh harmonic components are still not clearly distinguishable. In the TFR of ST using PS [39] shown in Fig. 4.15(d), the third and fifth harmonics are distinguishable, and frequency resolution for transient has improved. However, the voltage interruption is not detectable. In the TFR of ST using SS [105] shown in Fig. 4.15(e), the harmonics are not distinguishable, and the voltage interruption is also not detectable. Fig. 4.15(f) illustrates the effectiveness of proposed FS in detecting all disturbances. The FS provides better time resolution at lower frequencies, and better frequency resolution at higher frequencies.

The CM [112] for each TFR is listed in Table 4.2. It can be observed that OST with CLS outperforms ST with CLS. Moreover, proposed OST with FS is superior than existing scaling approaches. The ability of the proposed OCDW in concentrating the energy in given intervals in both domain can be observed in Figs. 4.15(b) and 4.15(f) and Table 4.2. The proposed FS along with OCDW provides a more reliable and highly concentrated TFR as compared to other scaling criteria with GW.

4.9 Conclusion

The simultaneously concentrated DPSS has maximum energy concentrations in finite intervals in both time and frequency domains. However, it is of infinite length. In this chapter, a multi-objective optimization approach was adopted for simultaneous maximization of time (α^2) and frequency (β^2) domain energy concentrations in finite intervals for finite length sequences. The optimal sequence thus obtained has been termed as OWFS. It has been derived that the feasible region of α^2 and β^2 is an intersection of a rectangle and Pareto-optimal front formed by the solutions of the aforementioned multi-objective

optimization problem. It has been shown analytically and through simulations that, as the support of proposed window approaches infinity, the feasible region merges to the feasible region of simultaneously concentrated DPSS. The achievable concentrations of various well known window kernels with finite support including truncated DPSS, have been compared with that of the proposed OWFS. This chapter also briefly introduced the simultaneously concentrated P-DPSS using the same approach as that of OWFS. A closed form expression for achievable α^2 and β^2 for simultaneously concentrated P-DPSS has been derived, and the impact of various window parameters has been discussed. A novel OCDW has been developed by solving a constraint optimization problem of maximization of the product $\alpha^2\beta^2$ in given discrete time discrete frequency intervals. The efficacy of the proposed OWFS has been presented by using it in TFA for IF estimation of multicomponent signal in noisy environment. The proposed OCDW was extended to design OST. Further, a novel fair scaling criterion has also been proposed for MRA. The proposed OCDW along with the novel scaling criterion provides higher energy concentration and better trade-off between time and frequency resolutions in TFR of ST.

Chapter 5

Sharp Detection of Event's Onset with Asymmetrical Modified Kaiser Window based ST

5.1 Introduction

In various fields such as seismology, biomedical engineering, audio and speech processing, etc. the main motive of signal analysis is event recognition. The example of some finite duration events are start and end of QRS complex, the arrival time of p and h seismic waves [42] and sudden changes of the spin rate of the Earth [59]. The correct localization of the events in time is of prime importance.

Reliable detection and identification of seismic events are extremely important for accurate estimation of magnitude and location of seismic events. Different methods for onset detection of events are discussed in literature that include method based on correlation coefficients from clusters of relevant adjacent traces [60], best fitted auto regressive (AR) model [61], AR moving average models [61] and Akaike information criterion (AIC) based model [62], and their combinations such as AR-AIC model [160], Machine learning based approaches [161], short and long time average ratio based model [63, 64], etc.

Since the aforementioned methods analyze the seismic traces either in time or frequency domain, they are suitable for analysis of signals having less noise and randomness. However, the seismic traces are non-stationary in nature, and mostly severely contaminated with noise. It is well suited to analyze these kind of signals in both time and frequency domains simultaneously [65].

The STFT and CWT coefficients are used for both identification and characterization of clusters in seismic traces [162, 163]. The WVD with Rényi entropy measure is used

for detection of seismic events [164, 165]. The ST has been widely used in seismic signal analysis [13, 53, 166, 167]. However, the long taper of the GW results in degraded time resolution of event's onset. In [168], the GST is presented which utilizes an asymmetrical window for decomposition and analysis of vibrations of gearbox. The Gaussian nose is welded to an exponential tail to provide asymmetry. The resulting time-frequency spectrum has better time resolution at onset of events. However, due to the long taper of the exponential tail, the event signatures are smeared in time. The GST using BGW is proposed for detection of various seismic events [59, 66]. The two half GW with different SDs are welded to provide asymmetry. In [53], a different scaling criterion is suggested for BGW based ST which can further improve the detection of event's onset at the cost of degraded frequency resolution. An another form of GST is also proposed which utilizes asymmetrical HW to determine different events in a noisy seismograph [42, 54] and power quality disturbances [68, 69]. The asymmetry in window provides asymmetry in time-frequency spectrum which leads to better time resolution at event's onset. The conventional ST [9] using GW provides poor time resolution for lower frequencies and good time resolution for higher frequencies. Hence, the asymmetry is preferably required at lower frequencies. The frequency dependent asymmetry is introduced in [42, 59]. However to provide asymmetry, welding of two functions leads to discontinuities.

In this work, an AMKW based ST is proposed for analyzing the time-frequency content of a broadband earthquake seismogram. MRA and frequency dependent asymmetry are obtained by modifying the β parameter of first order Bessel function. The basic form of GST using BGW and HW are reviewed in brief, and then AMKW and its extension in ST is proposed. Further, AMKW and AMKW based ST are proposed. The proposed method is tested by using synthetic seismic trace and real seismic data.

5.2 Proposed Asymmetrical Modified Kaiser Window based ST

The Kaiser window [169] approximates the first order discrete prolate spheroidal sequence, which is a finite length optimally concentrated function, and maximizes the energy concentration in main lobe. The conventional Kaiser window can be represented as [169]

$$w_K[h] = \begin{cases} \frac{I_0(\beta\sqrt{1-(h/N)^2})}{\sum_{-N/2}^{N/2-1} I_0(\beta\sqrt{1-(h/N)^2})}, & -\frac{N}{2} \leq h \leq \frac{N}{2} - 1 \\ 0, & \text{elsewhere} \end{cases}$$

where I_0 is the zero order modified Bessel function of the first kind. N is the length of the window. The parameter β controls the width of the window *i.e.* higher values of

β result in narrow windows in time domain, and vice versa. The Kaiser window based ST is presented in [170] where multi-resolution property is achieved by making β to be frequency dependent.

This objective proposes a modified asymmetrical version of Kaiser window for sharp detection of event's onset. The idea is to make the parameter β a decreasing function of time. It leads to narrower taper in forward direction due to high values of β , and longer taper in back direction due to smaller values of β . The time dependent parameter β can be defined as

$$\beta[h] = \pi\sigma_{k_1} \left(\frac{\sigma_{k_2}}{\sigma_{k_1}} \right)^{\left(\frac{h}{N} + 0.5 \right)} \quad (5.1)$$

where the parameters σ_{k_1} and σ_{k_2} control the characteristics of the modified Kaiser window. The width of the window is primarily characterized by the parameter σ_{k_1} , and the asymmetry is characterized by σ_{k_2} with respect of σ_{k_1} . To obtain narrow front taper as compared to back taper, σ_{k_1} is chosen to be greater than σ_{k_2} , and hence making (5.1) to be an exponentially decreasing function of h . Smaller the value of $\sigma_{k_2}/\sigma_{k_1}$, more will be the asymmetry. At $\sigma_{k_1} = \sigma_{k_2}$, the function $\beta[h]$ reduces to $\pi\sigma_{k_1}$, and hence results in conventional symmetrical Kaiser window.

It is to note that, in contrast to conventional Kaiser window function, the peak of the modified Kaiser window does not lie at $t = 0$. To account for that, a translation parameter ξ_K is introduced which can be defined as

$$\xi_K = \frac{N}{2} \left(\frac{1}{\ln(\sigma_{k_2}/\sigma_{k_1})} + \sqrt{1 + \left(\frac{1}{\ln(\sigma_{k_2}/\sigma_{k_1})} \right)^2} \right) \quad (5.2)$$

For multi-resolution analysis similar to conventional ST *i.e.* better frequency resolution at lower frequencies and higher time resolution at higher frequencies, the parameters of the proposed window can be chosen as

$$\sigma_{k_1} = kn, \quad \sigma_{k_2} = \sigma_{k_1} \left(\frac{2n}{N} \right) \quad (5.3)$$

The scaling criterion (5.3) provides frequency dependent scaling as well as frequency dependent asymmetry. As n increases, the time domain window becomes narrower due to increase in σ_{k_1} . Also, $\sigma_{k_2}/\sigma_{k_1}$ increases with increase in n , hence making the window more symmetrical. The perfect symmetry is achieved at Nyquist frequency $n = N/2$ where $\sigma_{k_2} = \sigma_{k_1}$. The additional scale parameter k is introduced to provide more flexibility in controlling the trade-off between time and frequency resolution. Increase in k leads to improved time resolution at the cost of degraded frequency resolution. The proposed

AMKW can be represented as

$$w_{MK}[h, n] = \begin{cases} \frac{I_0\left(\beta[h-\xi_K]\sqrt{1-\left(\frac{h-\xi_K}{N}\right)^2}\right)}{\sum_{-N/2}^{N/2-1} I_0\left(\beta[h-\xi_K]\sqrt{1-\left(\frac{h-\xi_K}{N}\right)^2}\right)}, & -\frac{N}{2} \leq h \leq \frac{N}{2} - 1 \\ 0, & \text{elsewhere} \end{cases}$$

The modified asymmetrical Kaiser window based ST can be represented as

$$S_K[l, n] = \sum_{m=-N/2}^{N/2-1} X[m+n] W_{MK}[m, n] e^{i2\pi\frac{m}{N}l} \quad (5.4)$$

$W_{MK}[m, n]$ represents the FT of the normalized $w_{MK}[l, n]$.

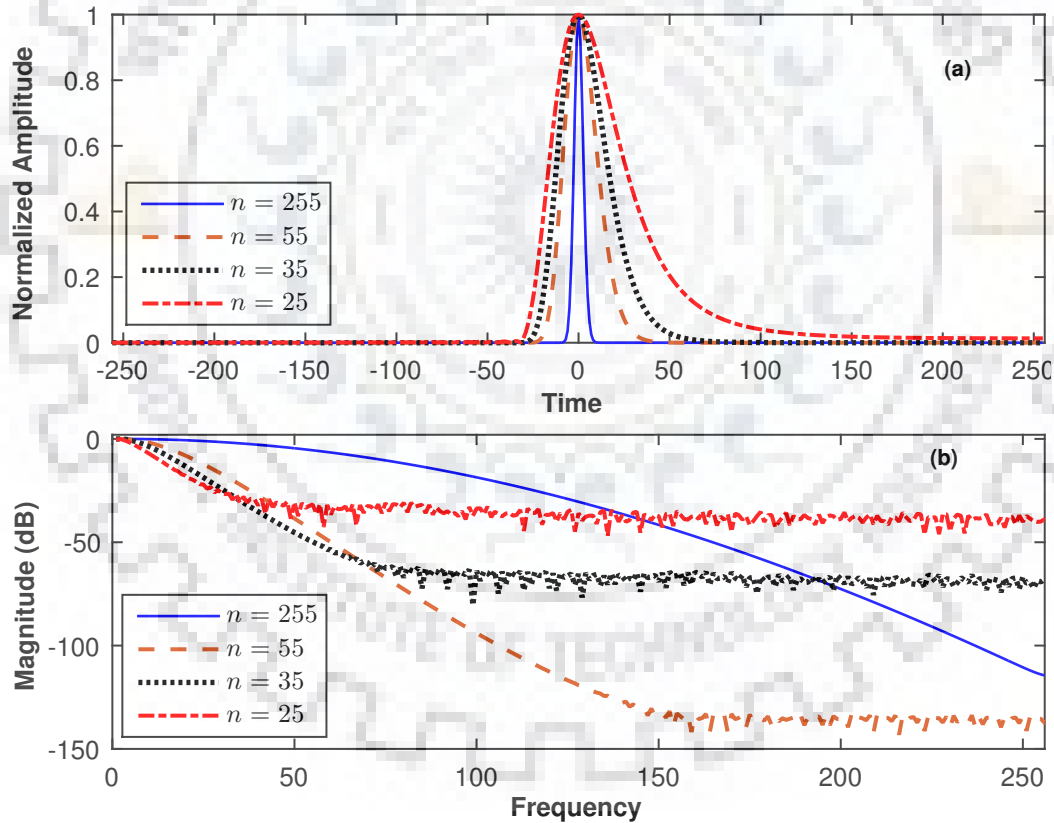


Fig. 5.1: Proposed window of length $N = 512$ for different frequencies: (a) Windows in time domain; (b) Corresponding frequency domain spectra

In Fig. 5.1, the proposed AMKW is illustrated in time domain for different frequencies n , along with their corresponding spectra. The multi-resolution property and asymmetric behaviour of the window can be observed in these figures. At lower frequency $n = 25$, the window is more asymmetrical in time domain (Fig. 5.1(a)) as well as having shorter

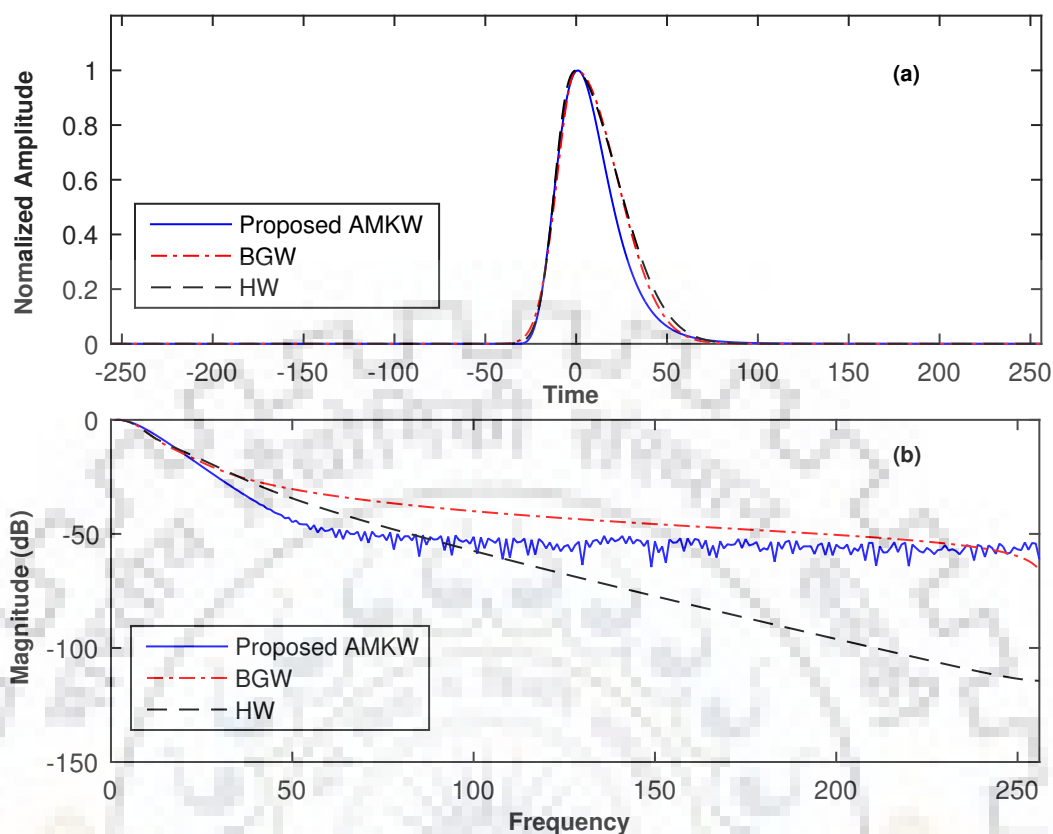


Fig. 5.2: (a) Comparison of HW, BGW and proposed AMKW of length $N = 512$: (a) Windows in time domain; (b) Corresponding frequency domain spectra

main lobe in frequency domain (Fig. 5.1(b)). As frequency increases, windows become more symmetrical. At Nyquist frequency $n = 255$, the window is symmetrical as well as having shorter width in time domain.

Fig. 5.2 compares the proposed AMKW with BGW [53, 59] and HW [42, 69] at frequency $n = 30$. Time domain windows and their spectra are shown in Fig. 5.2(a) and Fig. 5.2(b), respectively. It can be observed in Fig. 5.2(a) that the proposed window has steeper forward taper and faster roll-off in backward direction as compared to both BGW and HW. However, it has a very small slowly decaying tail. In Fig. 5.2(b), it can be observed that from 0 to 20 Hz, roll-off of all three windows are comparable. The proposed window has steeper roll-off from 20 Hz to 50 Hz, and saturated side-lobes are observed beyond 50 Hz.

5.3 Simulation Results

Case Study I:

The synthetic time series considered in this case study can be represented as [59]

$$x(1 : 128) = 0$$

$$x(129 : 512) = \exp(-4[0 : 388]/256)\sin(2\pi[0 : 383]20.4/512)$$

$$x(157 : 512) = x(157 : 512) + \exp(-5[0 : 355]/256)\sin(2\pi[0 : 355]30.7/512)$$

$$x(269 : 512) = x(269 : 512) + \exp(-4[0 : 243]/256)\sin(2\pi[0 : 243]25.3/512)$$

$$x(397 : 512) = x(397 : 512) + \exp(-4[0 : 115]/256)\sin(2\pi[0 : 115]15.6/512)2$$

The sampling frequency is 4 Hz. The time series shown in Fig 5.3(a) contains distinct changes at the 129th, 157th, 269th, and 397th sample points indicating four decaying

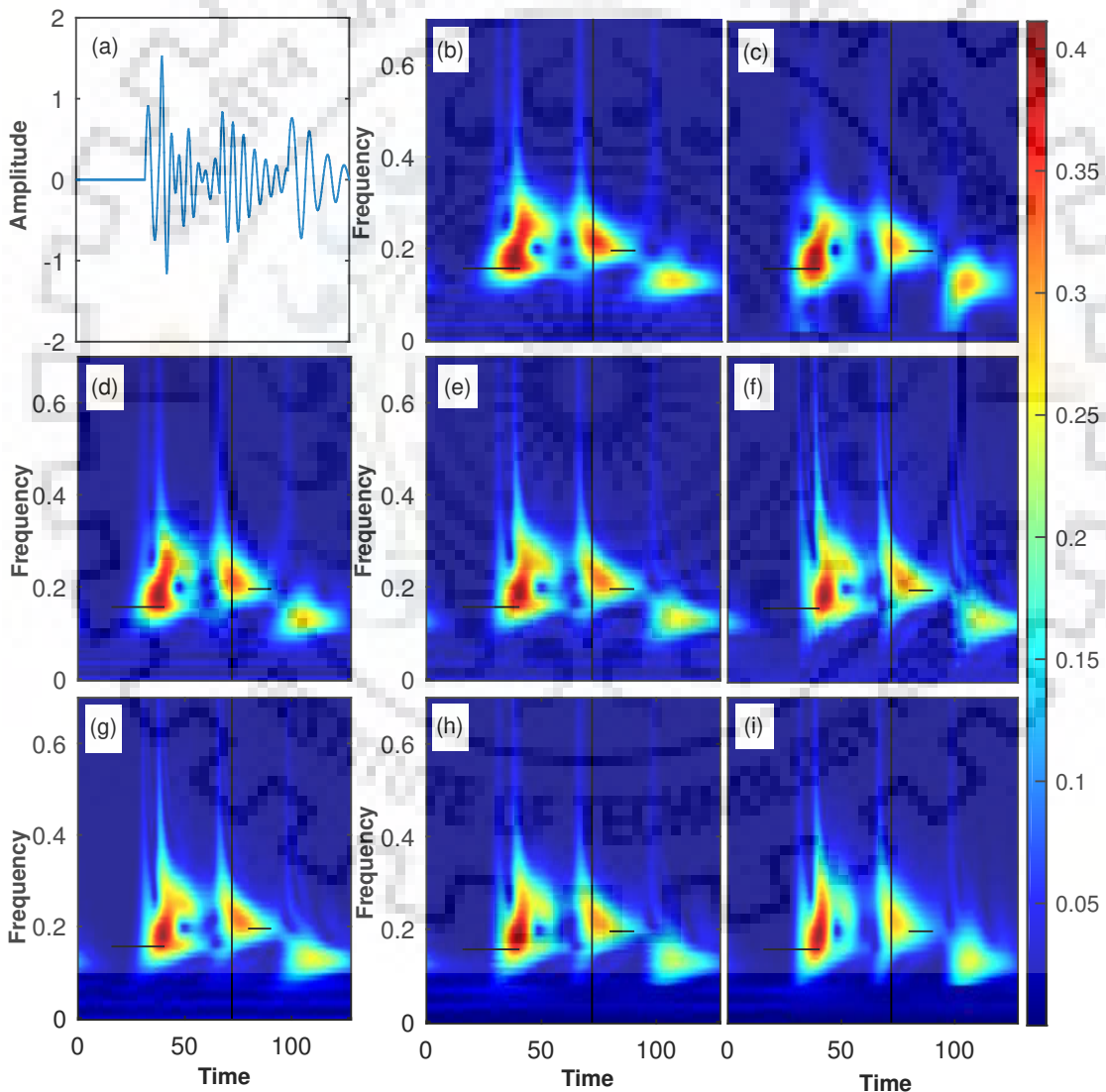


Fig. 5.3: Comparison of different symmetrical and asymmetrical window based STs: (a) Synthetic time series; Amplitude spectrum of (b) Conventional ST [9]; (c) 3PST [13]; (d) 4PST [19]; (e) BGW based ST [59]; (f) Variant of BGW based ST [53]; (g) HW based ST [69]; (h) Proposed AMKW based ST with $k = 1$; (i) Proposed AMKW based ST with $k = 1.5$. The horizontal and vertical lines show the cross-sections used for Fig. 5.4

sinusoidal events that overlap in time which leads to localized destructive interference. TFR using conventional ST is shown in Fig. 5.3(b). Due to long taper of the GW, time domain smearing of event's onset can be easily observed in the TFR. TFRs obtained using 3PST [13] 4PST [19] are shown in Fig. 5.3(c) and (d). The scaling parameters in 3PST and 4PST are tuned such as to maximize the overall CM of the TFRs. The improved time and frequency resolution can be observed in 5.3(c) and (d) as compared to that of the conventional ST. However, sharp time resolution at initiation of the events is missing in the three aforementioned symmetrical window based STs. Fig. 5.3(e) shows the TFR obtained using BGW based ST with frequency dependent asymmetry [59]. The asymmetry in window width profile leads to sharpness in forward direction with degraded resolution in backward direction. Also, due to asymmetry, some degradation in frequency resolution is observed as compared to the TFRs based on symmetrical windows. The TFR obtained using a different scaling for BGW based ST with lesser forward variance *i.e.* $l_{BG}^F = 0.1$ [53] is shown in Fig. 5.3(f). This modified scaling further improves the time resolution in forward direction but at the cost of degradation in frequency resolution. The TFR obtained using the HW based ST with frequency dependent asymmetry [69] is shown in Fig. 5.3(g). It is having very similar TFR characteristics as that of the BGW based ST. Fig. 5.3(h) shows the TFR obtained using proposed AMKW based ST with $k = 1$ in (5.3). It reveals improved time resolution in forward direction, and also has less smearing in backward direction with comparable frequency domain resolution. The resolution of initiation time of the events can be further improved by increasing the value of k at the cost of degraded frequency resolution as shown in Fig. 5.3(i) with $k = 1.5$.

To quantify the differences in the time and frequency resolution of different asymmetrical window based STs, Fig. 5.4 shows the amplitude of TFRs are along horizontal and vertical cross-sections shown in Fig. 5.3. In each TFR shown in Fig. 5.3, the first horizontal cross-section is shown at normalized frequency $20/128$ Hz, from time 16 seconds to 40 seconds. The second horizontal cross-section is shown at normalized frequency $25/128$ Hz from 80 seconds to 90 seconds. The vertical cross-section is shown at time 72 seconds. Horizontal cross-sections capture the time of initiation of first event. Short rise time indicates improved time resolution of event onset. It can be observed in Fig. 5.4(a) that the rise time of proposed AMKW based ST is much shorter than that of conventional ST. Moreover, the proposed AMKW based ST provides better event onset detection as compared to BGW, variant of BGW and HW based STs. The impact of backward taper on time resolution is illustrated in Fig. 5.4(b) which depicts the faster decay for proposed AMKW based ST as compared to other asymmetrical window based STs. The conventional ST, 3PST and 4PST have faster decay due to symmetric window characteristics. The characteristics of windows shown in Fig. 5.4(c) reveals that higher values beyond 0.4

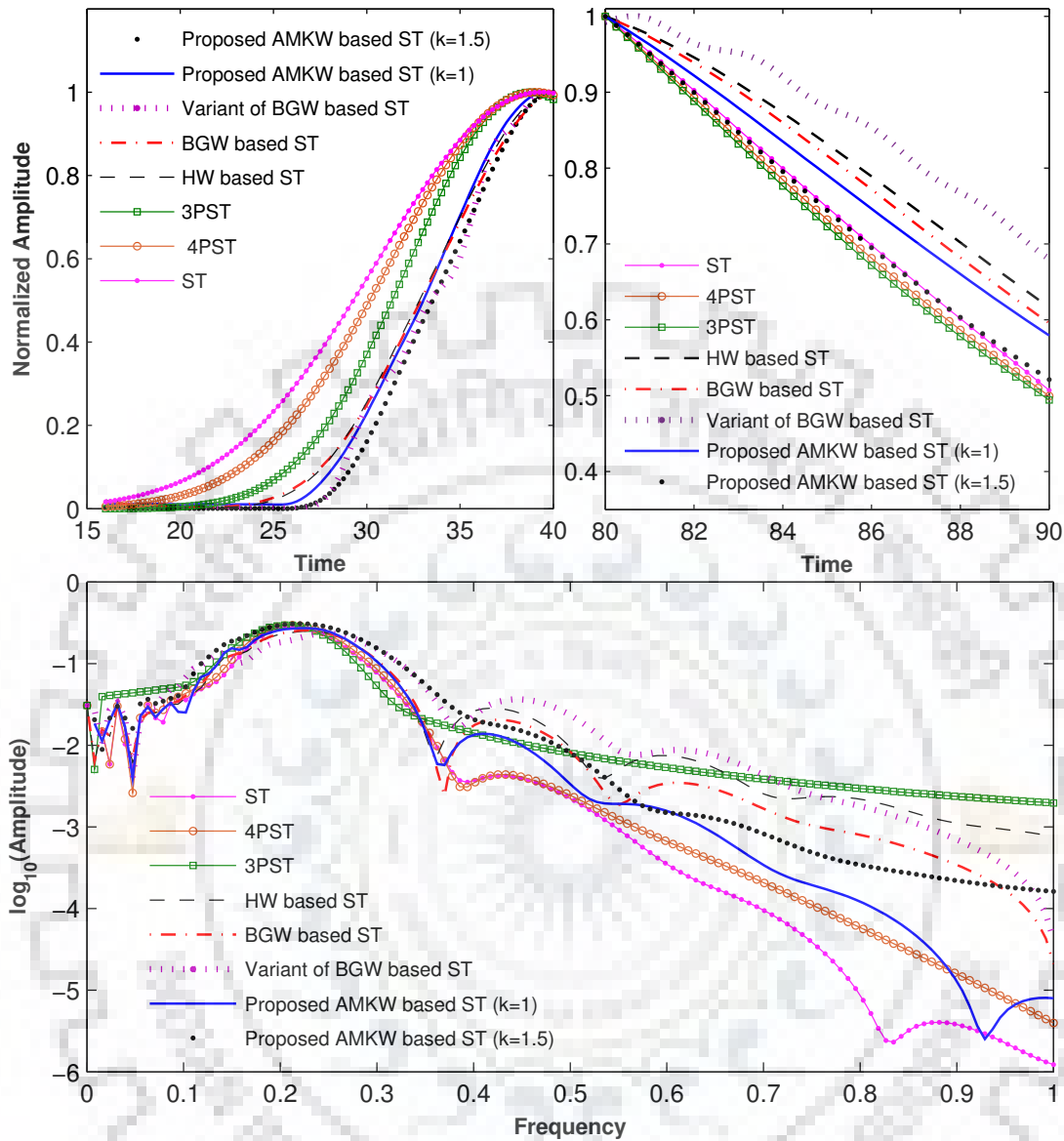


Fig. 5.4: Amplitude spectra of the TFRs for the cross sections shown in Fig. 5.3: (a) Along first horizontal cross-section; (b) Along second horizontal cross-section; (c) Along vertical cross-section

Hz correspond to unwanted artifacts due to poor frequency resolution. It can be observed that the asymmetrical window based STs have poor frequency resolution as compared to symmetrical window based STs. However, the proposed AMKW based ST has lower artifacts than that of the other three asymmetrical window based STs.

Table 5.1 compares the TFRs of ST, 3PST, 4PST, BGW based ST, HW based ST and AMKW based ST shown in Fig. 5.3 in terms of accuracy in detecting event's onset. The signal considered in Fig. 5.3(a) includes four decaying sinusoidal events starting at $t = 32$ second, $t = 39$ second, $t = 67$ second and $t = 99$ second. To quantify the event's arrival time, the amplitude variations in the TFR for the voice corresponding

Table 5.1: Comparison of TFRs in terms of accuracy (in seconds) in detecting event's onset

Event	Actual arrival	ST	3PST	4PST	BGW based ST	HW based ST	AMKW based ST
I	32	27	29	28	31	31	31.75
II	39	36	37	37.25	38	38	38.75
III	67	64	65	64	66	66	66.75
VI	99	94	96	95	97	97	98.75

to each event is studied. After several tests, the 30% amplitude threshold criterion is used to detect the arrival time of the event. It can be observed in Table 5.1 that due to long tapering of the symmetrical GW, conventional ST, 3PST and 4PST fail to detect the onset of the events accurately. As compared to the symmetrical window based STs, the asymmetrical window based STs provide better event detection accuracy. Due to similar window characteristics, the event detection accuracy of HW and BGW based STs are equal. The proposed AMKW based ST provides the best estimates of arrival time for the four events.

Case Study II:

Fig. 5.5 considers a 80-second segment of an earthquake seismogram recorded on 28 July 1995, at the GRFO seismic station (49.6919N, 11.2217E) in Graefenberg, Germany beginning at 14:43:51 UT for the earthquake occurred in the Tonga Trench (21.1S, 175.5E). The seismogram data can be downloaded from [171]. It is important to accurately determine the arrival times of different PKP phases for studying the anisotropy of the earth's inner core [172]. The seismogram is captured at the sampling rate of 20 Hz, and with angle being 151 degrees between the earthquake epicenter and the seismic station with respect to center of the earth. TFA is helpful in identifying several DF and BC phases of the core PKP wave.

Fig. 5.5 compares the TFRs of different symmetrical and asymmetrical window based STs. The first two visible events on each TFR, correspond to the arrival of the DF and BC phases of the PKP wave [172]. TFR using conventional ST is shown in Fig. 5.5(b). Due to long taper of the GW, time domain smearing of onset of DF and BC phases can be easily observed in the TFR. TFRs obtained using 3PST and 4PST are shown in Fig. 5.5(c) and (d). The scaling parameters in 3PST and 4PST are tuned such as to maximize the overall CM of the TFRs. The 3PST and 4PST provide improved time and frequency resolution as compared to that of the conventional ST which can also be observed in 5.5(c) and (d). However, for sharp detection of event's initiation, the time resolution at start of the events

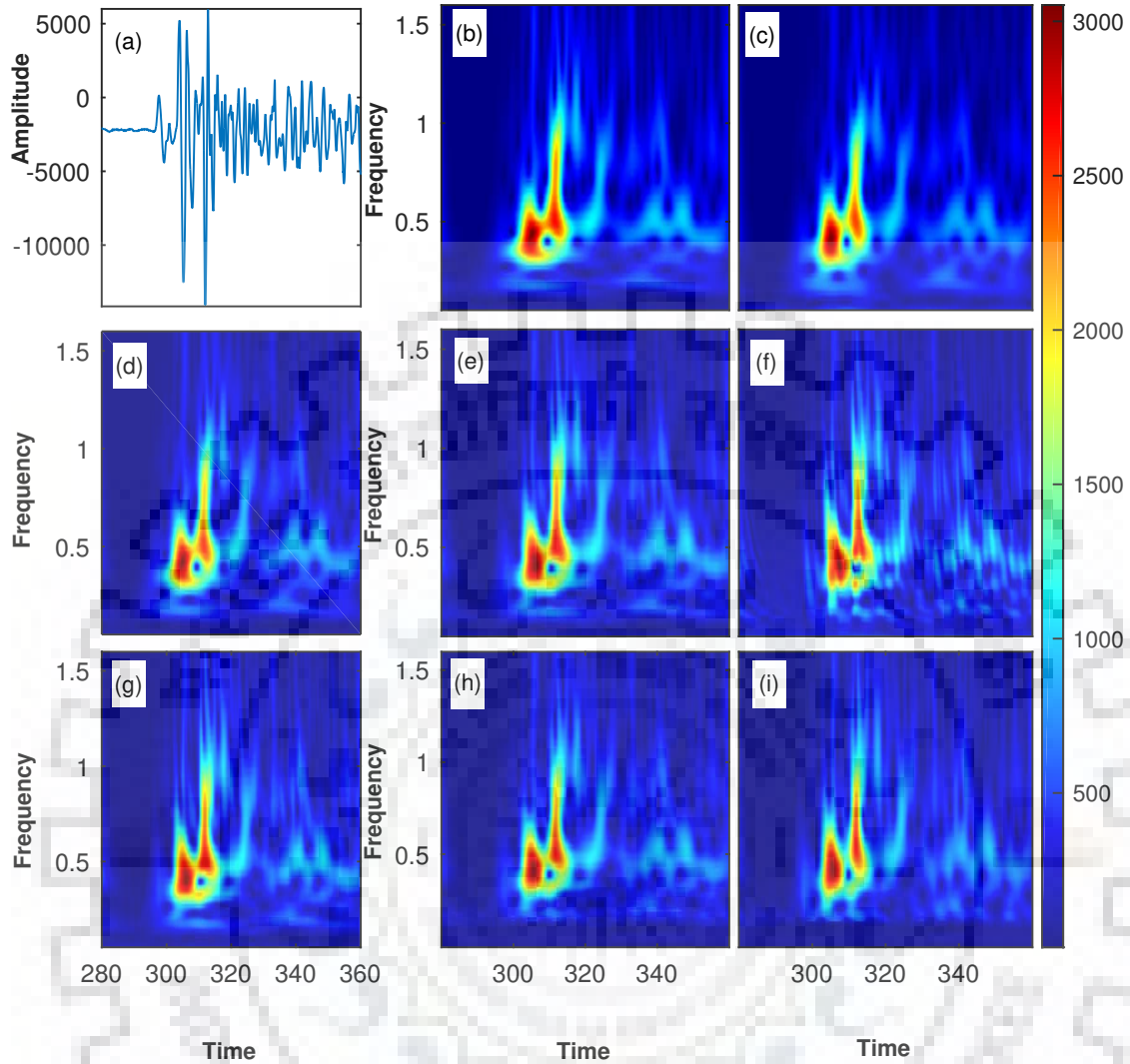


Fig. 5.5: Amplitude spectrum of different symmetrical and asymmetrical window based STs: (a) Earthquake seismogram [171]; Amplitude spectrum of (b) Conventional ST [9]; (c) 3PST [13]; (d) 4PST [19]; (e) BGW based ST [59]; (f) Variant of BGW based ST [53]; (g) HW based ST [69]; (h) Proposed AMKW based ST with $k = 1$; (i) Proposed AMKW based ST with $k = 1.5$

should be very precise which is missing in the three aforementioned symmetrical window based STs. Fig. 5.5(e) shows the TFR obtained using BGW based ST with frequency dependent asymmetry [59]. The asymmetry in window width profile leads to sharpness in forward direction with degraded resolution in backward direction. The TFR obtained using a different scaling for BGW based ST with lesser forward variance *i.e.* $l_{BG}^F = 0.1$ [53] is shown in Fig. 5.5(f). This modified scaling further improves the time resolution in forward direction but at the cost of degradation in frequency resolution. The TFR obtained using the HW based ST with frequency dependent asymmetry [69] is shown in Fig. 5.5(g). It is having very similar TFR characteristics as that of the BGW based ST.

Fig. 5.5(h) shows the TFR obtained using proposed AMKW based ST with $k = 1$ in (5.3). It reveals improved time resolution in forward direction, and also has less smearing in backward direction with comparable frequency domain resolution. The resolution of initiation time of the events can be further improved by increasing the value of k at the cost of degraded frequency resolution as shown in Fig. 5.3(i) with $k = 1.5$. Therefore, it can be said that the resolution of event initiation time in the TFR of proposed AMKW based ST is better than that of other counterparts. The leading edge of each event signature has a more “vertical” profile in TFR of proposed AMKW based ST as compared to the three asymmetrical window based TFRs. Moreover, the high-frequency artifacts are also lesser in the TFR of proposed AMKW based ST.

Table 5.2: Comparison of TFRs in terms of accuracy in detecting event’s onset

Events	Actual arrival	ST	3PST	4PST	BGW based ST	HW based ST	AMKW based ST
I	303.7	301	301.6	301.4	302.8	302.4	303.5
II	311	308.1	308.5	308.4	309.6	309.9	310.7

Table 5.2 compares the TFRs of ST, 3PST, 4PST, BGW based ST, HW based ST and AMKW based ST shown in Fig. 5.5 in terms of accuracy in detecting event’s onset. The signal considered in Fig. 5.5(a) has two events which correspond to the arrival of the DF and BC phases of the PKP wave. It is important to accurately detect the arrival time of the events. The 30% amplitude threshold criterion is used to detect the arrival time of the events. It can be observed in Table 5.2 that the the accuracy in detection of first event for TFRs of BGW and AMKW based STs are 99.93% and 99.7%, respectively. The accuracy in detection of second event for TFRs of HW and AMKW based STs are 99.64% and 99.9%, respectively. The TFR of proposed AMKW based ST provides the best estimates of arrival time for both the events as compared to other TFRs.

5.4 Conclusion

Due to long taper of the GW, the conventional ST provides poor time resolution in TFR, especially at lower frequencies. BGW and HW based STs provide better time resolution in forward direction as compared to conventional ST, and hence can be used for sharp detection of onset of events in seismic signals. However, the benefits are obtained at the cost of poorer time resolution in backward direction which may affect the resolvability of successive events. In this work, AMKW has been proposed which provides a sharp front taper as well as faster decaying back taper as compared to BGW and HW. The window parameters are chosen in such a way that it provides frequency dependent asymmetry.

The inherent maximum energy concentration of Kaiser window along with frequency dependent asymmetry help in eliminating the unwanted high frequency artifacts in the TFR. The efficacy of the proposed approach has been tested using a synthetic time series as well as a real noisy earthquake seismogram. The results show that the proposed AMKW based ST is able to detect the events early as compared to other symmetrical and asymmetrical window based STs.



Chapter 6

Reassignment of Energy in the TFRs of OST and Product-ST

6.1 Introduction

In order to achieve near ideal TFR, some advanced post processing methods have been proposed in literature such as the RM [45, 46] and SST [47, 48]. These tools have the ability to reassign or squeeze the time-frequency coefficients obtained by classical TFA methods into the IF trajectory [49, 50]. The RM reassigns the time-frequency coefficients along both time and frequency axes in the TFR. The SST squeezes the time-frequency coefficients into the IF trajectory only along the frequency axis. Also, the SST has the ability to reconstruct the different modes of the signal. In recent years, RM and SST has been widely used in various disciplines such as earth sciences [71, 72], biomedical engineering [70, 73], mechanical engineering [74], civil engineering [75–77], etc.

Although the conventional linear TFRs along with RM and SST provide very narrow ridges as compared to the conventional TFRs, their ability to separate out two signal components still depend on the width of the window in time and frequency domains. For SST and RM to properly resolve two modes in frequency domain, the minimum separation between these two modes must be equivalent to the bandwidth of the used window. Similarly, to separate out two signal components in time domain, the support of the window in time must be shorter than that of signal components [51]. Resolving closely spaced signal components in both time and frequency domain simultaneously using SST and RM techniques remains a challenge.

The efficiency of the aforementioned post processing methods depends on the separability of modes in time and frequency domains. To counter this shortcoming, the SST and RM are deployed on the TFR of OST, and further investigated for detecting multiple power quality disturbances. It is found that the OST combined with RM and SST provides

better visualization as compared to OST. A concept of product-ST is also proposed to further improve the visualization of TFR for very closely spaced signal components in time and frequency. The TFR of product-ST is obtained by multiplying the TFRs of TST and BST. The concepts of RM and SST are incorporated in the product-ST. It is found that the product-ST combined with RM and SST provides better visualization and accurate frequency detection as compared to its OST counterpart.

6.2 OST Combined with RM and SST

The RM and SST reassign the TFR coefficients of OST into IF, whose coordinates are defined as

$$\hat{f} = f - \Im \left(\frac{S^{\varphi'}(t, w)}{S^{\varphi}(\tau, w)} \right) \quad (6.1)$$

$$\hat{\tau} = \tau + \Re \left(\frac{S_{OCDW}^{t\varphi}(t, w)}{S_{OCDW}^{\varphi}(\tau, w)} \right) \quad (6.2)$$

where $S^{\varphi'}$ represents the TFR of OST obtained with derivative of the OCDW and $S^{t\varphi}$ represents the TFR of OST obtained with function $t\varphi(t, f)$.

The OST combined with RM at any point (τ_0, f_0) can be represented as

$$SS_{OCDW}(\tau_0, f_0) = \int \int S^{\varphi}(\tau, f) \delta(\tau_0 - \hat{t}) \delta(f_0 - \hat{f}) d\tau df$$

6.3 Proposed Product-ST

To further improve the time and frequency resolution in TFR of OST, the concept of product-ST is discussed. The highly concentrated product-ST can be obtained by multiplying the TFRs of TST and BST. The frequency domain computation of TST and BST of continuous signal $x(t)$ can be represented as

$$S^{v_{TL}}(\tau, f) = \int_{-\infty}^{\infty} X(\alpha + f) \zeta_{TL}(\alpha, f) e^{i2\pi\alpha\tau} d\alpha \quad (6.3)$$

$$S^{v_{BL}}(\tau, f) = \int_{-\infty}^{\infty} X(\alpha + f) \zeta_{BL}(\alpha, f) e^{i2\pi\alpha\tau} d\alpha \quad (6.4)$$

where $X(\alpha)$, $\zeta_{TL}(\alpha)$ and $\zeta_{BL}(\alpha)$ represent FT of $x(t)$, optimally concentrated time-limited window $v_{TL}(t)$ and optimally concentrated band-limited window $v_{BL}(t)$, respectively. The

proposed product-ST can be represented as

$$P^{(v_{TL}, v_{BL})}(\tau, f) = S^{v_{TL}}(\tau, f)S^{v_{BL}}(\tau, f) \quad (6.5)$$

6.3.1 Product-ST Combined with SST

To obtain the IF, consider a monocomponent (\hat{f}) signal with fixed amplitude A as

$$x(t) = Ae^{i2\pi\hat{f}t} \quad (6.6)$$

The FT of the signal can be represented as

$$X(\alpha) = A \delta(\alpha - \hat{f}) \quad (6.7)$$

where $\delta(\cdot)$ represents dirac function. Using (6.7), (6.3) and (6.4) can be represented as

$$S^{v_{TL}}(\tau, f) = A\zeta_{TL}(\hat{f} - f, f)e^{i2\pi(\hat{f}-f)\tau} \quad (6.8)$$

$$S^{v_{BL}}(\tau, f) = A\zeta_{BL}(\hat{f} - f, f)e^{i2\pi(\hat{f}-f)\tau} \quad (6.9)$$

To obtain the IF, it is suggested to calculate derivative of the TFR with respect to time. The derivative of product-ST can be written as

$$\partial_{\tau}(P^{(v_{TL}, v_{BL})}(\tau, f)) = i4\pi(\hat{f} - f)P^{(v_{TL}, v_{BL})}(\tau, f) \quad (6.10)$$

Therefore, the IF can be estimated as

$$\hat{f} = f - i \frac{\partial_{\tau}(P^{(v_{TL}, v_{BL})}(\tau, f))}{4\pi P^{(v_{TL}, v_{BL})}(\tau, f)} \quad (6.11)$$

Using time domain computation of TST and BST, $\partial_{\tau}(P^{(v_{TL}, v_{BL})}(\tau, f))$ can be represented as

$$\partial_t(P^{(v_{TL}, v_{BL})}(\tau, f)) = S^{\partial_t(v_{TL})}(\tau, f)S^{v_{BL}}(\tau, f) + S^{v_{TL}}(\tau, f)S^{\partial_t(v_{BL})}(\tau, f) \quad (6.12)$$

where $S^{\partial_t(v_{TL})}(\tau, f)$ and $S^{\partial_t(v_{BL})}(\tau, f)$ represent the ST obtained using time derivative of v_{TL} and v_{BL} as window functions, respectively.

By using (6.12), the IF in (6.11) can be redefined as

$$\hat{f} = f - \Im \left(\frac{S^{\partial_t(v_{TL})}(\tau, f)S^{v_{BL}}(\tau, f) + S^{v_{TL}}(\tau, f)S^{\partial_t(v_{BL})}(\tau, f)}{4\pi P^{(v_{TL}, v_{BL})}(\tau, f)} \right) \quad (6.13)$$

where $\Im(x)$ represents imaginary part of x . The SST reassigns the TFR coefficients along IF trajectory. The value of the product-ST combined with SST at any frequency (f_0) can be represented as

$$SSPST(\tau, f_0) = \int_{-\infty}^{\infty} P^{(v_{TL}, v_{BL})}(\tau, f) \delta(f_0 - \hat{f}) df \quad (6.14)$$

6.3.2 Product-ST Combined with RM

To derive the GD, consider a signal having an impulse as

$$x(t) = A \delta(t - \hat{\tau}) \quad (6.15)$$

By considering time domain computation of TST and BST, $S^{v_{TL}}(\tau, f)$ and $S^{v_{BL}}(\tau, f)$ for this signal can be represented as

$$S^{v_{TL}}(\tau, f) = Av_{TL}(\tau - \hat{\tau}, f) e^{-i2\pi f \hat{\tau}} \quad (6.16)$$

$$S^{v_{BL}}(\tau, f) = Av_{BL}(\tau - \hat{\tau}, f) e^{-i2\pi f \hat{\tau}} \quad (6.17)$$

For GD, derivative of $P^{(v_{TL}, v_{BL})}(\tau, f)$ with respect to frequency can be represented as

$$\begin{aligned} \partial_f(P^{(v_{TL}, v_{BL})}(\tau, f)) &= \partial_f(S^{v_{TL}}(\tau, f)) S^{v_{BL}}(\tau, f) + \partial_f(S^{v_{BL}}(\tau, f)) S^{v_{TL}}(\tau, f) \\ &= S^{\partial_f(v_{TL})}(\tau, f) S^{v_{BL}}(\tau, f) + S^{v_{TL}}(\tau, f) S^{\partial_f(v_{BL})}(\tau, f) \\ &\quad - (\hat{\tau} i 4\pi) S^{v_{TL}}(\tau, f) S^{v_{BL}}(\tau, f) \end{aligned} \quad (6.18)$$

Therefore,

$$\hat{\tau} = \frac{S^{\partial_f(v_{TL})}(\tau, f) S^{v_{BL}}(\tau, f) + S^{v_{TL}}(\tau, f) S^{\partial_f(v_{BL})}(\tau, f)}{i4\pi P^{(v_{TL}, v_{BL})}(\tau, f)} - \frac{\partial_f(P^{(v_{TL}, v_{BL})}(\tau, f))}{i4\pi P^{(v_{TL}, v_{BL})}(\tau, f)} \quad (6.19)$$

Similar to (6.12), $\partial_f(P^{(v_{TL}, v_{BL})}(\tau, f))$ can be represented as

$$\begin{aligned} \partial_f(P^{(v_{TL}, v_{BL})}(\tau, f)) &= S^{\partial_f(v_{TL})}(\tau, f) S^{v_{BL}}(\tau, f) + S^{v_{TL}}(\tau, f) S^{\partial_f(v_{BL})}(\tau, f) \\ &\quad - i2\pi (S^{(tv_{TL})}(\tau, f) S^{v_{BL}}(\tau, f) + S^{(tv_{BL})}(\tau, f) S^{v_{TL}}(\tau, f)) \\ &\quad - i4\pi \tau P^{(v_{TL}, v_{BL})}(\tau, f) \end{aligned} \quad (6.20)$$

By using (6.20), GD in (6.19) can be redefined as

$$\hat{\tau} = \tau + \Re\left(\frac{S^{(tv_{TL})}(\tau, f) S^{v_{BL}}(\tau, f) + S^{(tv_{BL})}(\tau, f) S^{v_{TL}}(\tau, f)}{2P^{(v_{TL}, v_{BL})}(\tau, f)}\right) \quad (6.21)$$

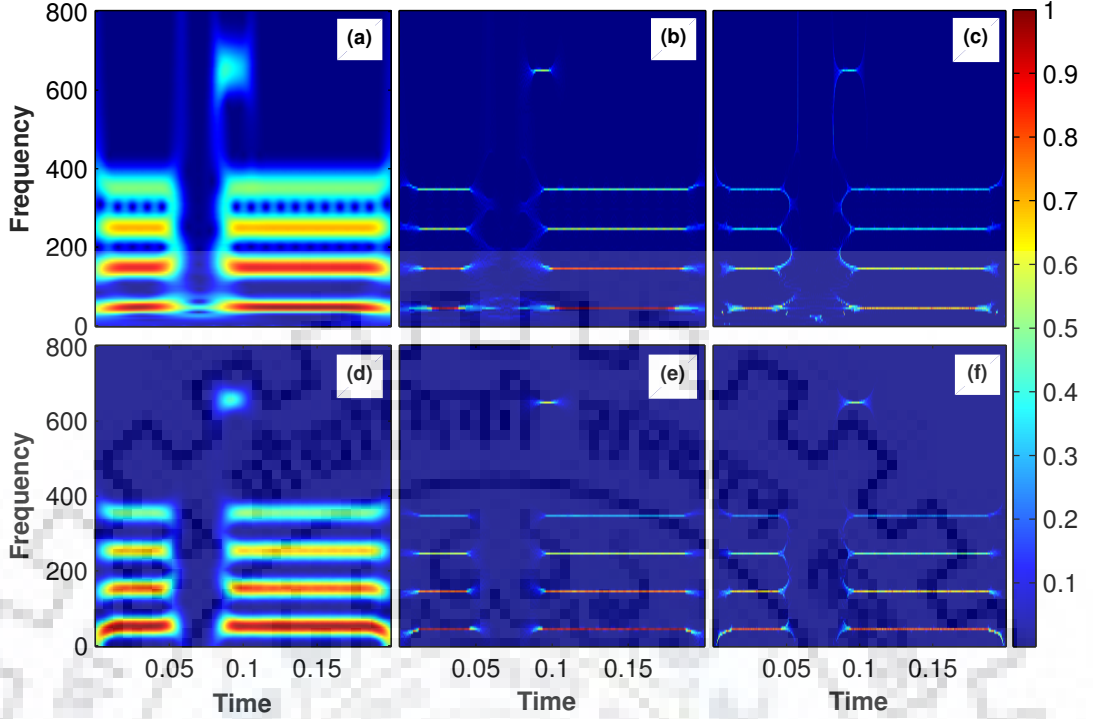


Fig. 6.1: Comparison of amplitude spectrum of TFRs: (a) OST (b) OST combined with SST; (c) OST combined with RM; (d) Proposed product-ST for $k_1 = 64, k_2 = 0.42, k_3 = 20, k_4 = 100, M_{th} = 5$ and $L_{th} = 5$; (e) Proposed product-ST combined with SST; (f) Proposed product-ST combined with RM

where $\Re(x)$ represents real part of x . RM reassign the TFR coefficients to $(\hat{\tau}, \hat{f})$ rather than to (τ, f) where it is computed. The value of the product-ST combined with RM at any point (τ_0, f_0) can be represented as

$$RPST(\tau_0, f_0) = \int_{-\infty}^{\infty} \int_{-\infty}^{\infty} P^{(\nu_{TL}, \nu_{BL})}(\tau, f) \delta(\tau_0 - \hat{\tau}) \delta(f_0 - \hat{f}) d\tau df \quad (6.22)$$

For a multicomponent signal having well separated distinct modes, (6.13) and (6.21) can be used for estimating the IF and GD of each mode effectively [50, 173].

6.4 Simulation Results

6.4.1 Case Study 1: Detection of Multiple Power Quality Disturbances

In order to evaluate the performance of the OST and Product-ST combined with RM and SST, a synthetic signal with multiple power quality disturbances is considered in Fig. 6.1. The signal of duration 0.2 seconds is synthesized with sampling frequency of 3.2 KHz as

per the IEEE 1159 standards [120]. The signal consists of voltage interruption, oscillatory transient and odd harmonic components upto seventh order along with fundamental frequency component of 50 Hz. The magnitude of fundamental frequency component, third, fifth and seventh harmonic components are 1, 0.9, 0.7 and 0.5 pu, respectively. The duration of voltage interruption is from $t = 0.058$ sec to $t = 0.082$ sec. The duration of transient is from $t = 0.082$ sec to $t = 0.105$ sec. Fig. 6.1(a) shows the TFR of OST with FS for $\gamma = 0.99$ and $k_5 = 10$. It can be observed that due to very short duration, the interruption is not clearly distinguishable. Further, frequency resolution of fifth and seventh harmonic components is poor. The TFRs of OST combined with SST and RM are shown in Figs. 6.1(b) and 6.1(c), respectively. By using these post processing tools, the time and frequency resolution of the frequency components in TFR have improved drastically. However, due to very closely spaced interruption and harmonics, the TFR of OST fails to provide clearly separable components in time and frequency. Therefore, the TFRs of OST combined with RM and SST are also not able to provide very good resolvability in components in time and frequency domain. The interruption is not clearly detectable.

The TFR of product-ST is shown in Fig. 6.1(d) for $k_1 = 64, k_2 = 0.42, k_3 = 20, k_4 = 100, M_{th} = 5$ and $L_{th} = 5$. It can be observed in Fig. 6.1(d) that as compared to TFR of OST shown in Fig. 6.1(a), the TFR of product-ST provides very good time and frequency resolution. All disturbances are clearly detectable and distinguishable. TFRs of the product-ST combined with SST and RM are shown in Figs. 6.1(e) and 6.1(f), respectively. The RM and SST further improves the time and frequency resolution. The interruption and its duration in signal are detectable. The frequency resolution of fifth and seventh harmonic components are better than their counterparts based on OST. Therefore, the proposed product-ST combined with RM and SST provide better TFR resolution than that of OST combined with RM and SST. Moreover, the product-ST combined with RM and SST are very useful for TFA of very closely spaced signal components in time and frequency.

6.4.2 Case Study 2: Analysis of San Fernando Earthquake Data

Recent advancement in seismology facilitates unprecedented investigation into the changing dynamic properties of structures during moderate and strong ground motions. Development of seismic stations in structures such as buildings, bridges, dams, etc. provides great insight into moderate or permanent change in dynamic properties of structures, and is also useful for detection of onset and peak velocities of this event [75, 76].

Permanent damage caused by strong earthquake motion results in plastic deformation or fracture due to permanently decreasing natural frequency of structures. This is due to loss of system's stiffness. Change in frequency is directly proportional to change in

stiffness of the structure, $f = \frac{1}{2\pi} \sqrt{\frac{k}{m}}$ where f , k and m are natural frequency, stiffness and mass of the structure, respectively. The temporary decrease in natural frequency can cause large and rapid destruction due to nonlinearity of the force-displacement relationship. Therefore, it is important to investigate the changes in natural frequency of the structures [77]. Fourier analysis can provide information regarding frequency content of the signal. However, it is unable to localize the exact onset of changes and their shifting variation in time [75], [77].

In this case study, the product-ST combined with RM and SST are used to analyze the San Fernando earthquake data. The San Fernando earthquake (9 February 1971, Magnitude= 6.6, distance approx. 31 kilometer), was recorded at Millikan Library east-west roof located in the main campus of the California Institute of Technology in Pasadena. This structure is a nine-storey reinforced concrete building built in 1966. In 1968, the building was instrumented with two permanent triaxial Teledyne-Geotech RFT-250 accelerometers located on the roof and basement. It is a well-inspected testbed building for structural health monitoring [75]. The San Fernando earthquake caused severe damage to the structure. The data was recorded by the accelerometer on top of the structure for approximately 98.90 seconds where peak ground acceleration is 340.8 cm/s^2 . The p wave arrival is at $t = 3.06$ second.

The data is considered upto 35 seconds for analysis as shown in Fig. 6.2(a). The sampling frequency is 50 Hz. It has a constant frequency of 1.2 Hz from $t = 5$ second to $t = 7.5$ second. At $t = 7.5$ second, the building starts losing its stiffness. The data has an exponential decay in frequency from 1.2 Hz to 0.9 Hz starting from $t = 7.5$ second to $t = 16$ second. A constant frequency pattern is observed after $t = 16$ seconds which indicates a permanent loss of stiffness.

The TFR of conventional ST shown in Fig. 6.2(b) provides poor time and frequency localization. Therefore, it is unable to interpret the exact frequency and event's initiation time such as start of loss of stiffness and exact time of permanent loss. The TFR of 3PST is shown in Fig. 6.2(c). It can be observed that the smearing is less as compared to conventional ST. However, it is unable to precisely localize the frequency component and its shifting pattern. The TFR of OST shown in Fig. 6.2(d) provides better time and frequency resolution than that of conventional ST and 3PST. The TFR of OST combined with SST and RM are shown in Figs. 6.2(e) and 6.2(f), respectively. The SST and RM improves the time resolution in the TFR of OST. The TFR of product-ST is shown in Fig. 6.2(g). The window parameters in TST and BST are chosen so as to maximize over all CM. It provides good time and frequency resolution as compared to other conventional counterparts. The noise effect in accelerometer data is also less visible. The TFR of product-ST combined with SST and RM shown in Figs. 6.2(h) and 6.2(i), respectively

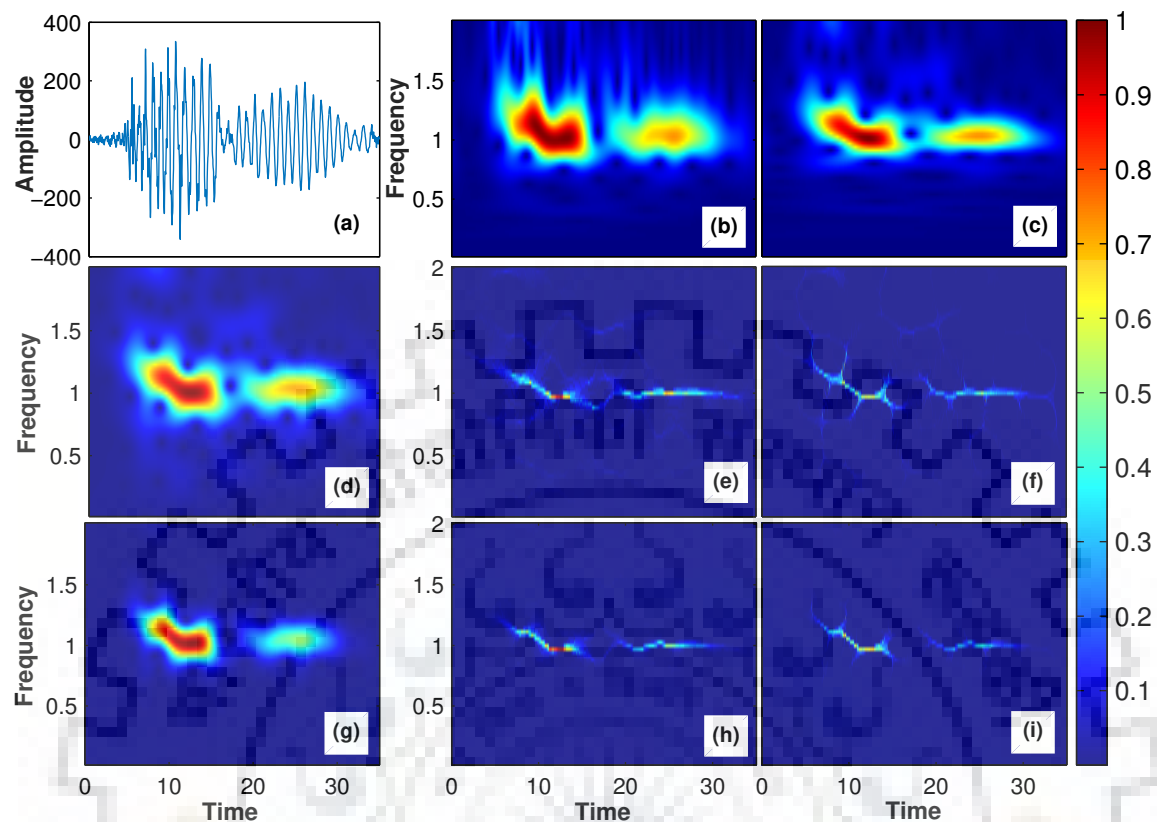


Fig. 6.2: Comparison of different TFA tools for San Fernando earthquake data (a) San Fernando earthquake data: TFR of (b) Conventional ST; (c) 3PST; (d) OST; (e) OST combined with SST; (f) OST combined with RM; (g) Proposed product-ST; (h) Proposed product-ST combined with SST; (i) Proposed product-ST combined with SST

provide excellent visualization of shifting pattern of frequencies. The product-ST combined with SST provides better frequency resolution than that of OST combined with SST. The product-ST combined with RM provides better time and frequency resolution as compared to other shown TFRs. This TFR can be considered as a close match of ideal behaviour of frequency shifting pattern (from 1.3 Hz to 0.9 Hz during 5-16 seconds, and a constant frequency of approx. 1 Hz from 16 to 34 seconds after losing its stiffness permanently) during earthquake.

6.4.3 Case Study 3: Analysis of Northridge Earthquake Data

In this case study, the considered signal is Northridge earthquake data (17 January 1994, Magnitude= 6.7, distance approx. 34 kilometer), recorded at Burbank ten-storey residential building roof center. This structure is a ten-storey residential building constructed in 1974. At the time of earthquake, the building was instrumented with 16 accelerometers, on four levels (first, fourth, and eighth floors, and roof) in the building. Severe cracks have been reported in the structure due to the Northridge earthquake. The data was recorded

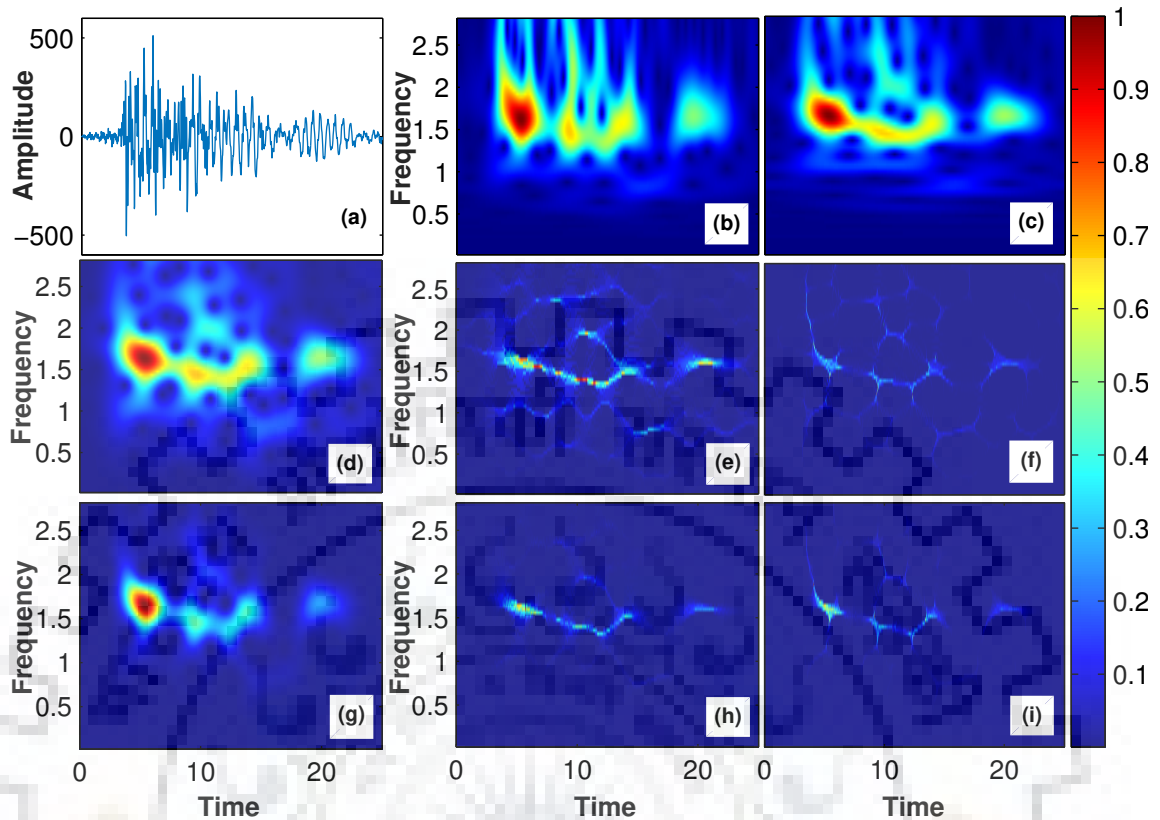


Fig. 6.3: Comparison of different TFA tools for Northridge earthquake data; (a) Northridge earthquake data; TFR of (b) Conventional ST; (c) 3PST; (d) OST; (e) OST combined with SST; (f) OST combined with RM; (g) Proposed product-ST; (h) Proposed product-ST combined with SST; (i) Proposed product-ST combined with SST

by the accelerometer on the top of the structure for around 50 seconds. The peak ground acceleration is 511.99 cm/s^2 . The p wave arrival is at $t = 4$ second.

The data is considered for $t = 0 - 25$ seconds for analysis as shown in Fig. 6.3(a). The sampling frequency is 50 Hz. The frequency shifting pattern in Northridge data can be interpreted in three different regions. A constant frequency of 1.75 Hz is observed at $t = 4$ second. The data has an exponential decay in frequency from $t = 4$ seconds to $t = 11$ seconds. A constant frequency pattern is observed after $t = 11$ seconds which indicates a permanent loss of stiffness.

Fig. 6.3 compares different TFA tools used for analyzing frequency shifting pattern at Burbank during Northridge earthquake. The TFR of ST shown in Fig. 6.3(b), provides poor time and frequency localization. Therefore, it is unable to interpret the exact frequency and event's initiation time. The TFR of 3PST is shown in Fig. 6.2(c). It can be observed that the frequency domain smearing is less as compared to conventional ST. However, it is unable to precisely localize the frequency component and its shifting pattern. The TFR of OST shown in Figs. 6.3(d) provides better time and frequency resolution

than that of conventional ST and 3PST. The TFR of OST combined with SST and RM, shown in Fig. 6.3(e) and 6.3(f), respectively, further improves the time and frequency resolution in the TFR of OST. The TFR of product-ST is shown in Fig. 6.3(g). The window parameters in TST and BST are chosen so as to maximize CM. It provides good time and frequency resolution as compared to other conventional counterparts. The noise effect in accelerometer data is also decimated significantly. The TFR of product-ST combined with SST and RM shown in Fig. 6.3(h) and 6.3(i), respectively provide significant improvement as compared to its OST counterpart. The product-ST combined with RM provides better time and frequency resolution as compared to other shown TFRs. This TFR can be considered as a close match of ideal behaviour of frequency shifting pattern (from 1.8 Hz to 1.3 Hz during $t = 4 - 12$ seconds and a constant frequency of approx. 1.65 Hz after losing its stiffness permanently) during Northridge earthquake.

6.5 Conclusion

In this chapter, a novel approach of OST combined with RM and SST, a highly concentrated product-ST and product-ST combined with RM and SST are proposed. The product-ST is obtained by multiplying the two TFRs of proposed variant of ST in chapter 3, namely TST and BST. The TST has the ability to resolve two components precisely in time while having optimal possible energy concentration in frequency. The BST is able to resolve two frequency components precisely in frequency. Therefore, the product-TFR is having excellent time and frequency resolvable capability. It also decimates the effect of noise in the signal. One of the limitations of the proposed product-ST is that it loses the reconstruction ability of ST as it is obtained through multiplying the two TFRs of ST which results in phase distortion.

The post processing methods such as SST and RM improves the TFR resolution. The concepts of SST and RM are also incorporated in product-ST. The performance of OST and product-ST along with RM and SST is evaluated for detection of very closely spaced power quality disturbances and frequency shifting pattern in structural buildings during earthquake. It is found that, the product-ST combined with RM and SST outperform the OST combined with RM and SST.

Chapter 7

Conclusions and Future Scope

The research work discussed in this dissertation focuses on maximization of energy concentration in TFR of the ST. Previous chapters have reported the entire work carried out in this dissertation. This chapter finally summarizes the conclusions that have been drawn from comprehensive result analysis and observations. Also, it recommends the directions for future studies.

7.1 Conclusions

As a preliminary task, two optimally concentrated time-limited and band-limited windows have been proposed, and their associated properties have been illustrated. These proposed windows have been extended to develop two variants of ST, namely TST and BST for better analysis of the time-limited and band-limited signals, respectively. The proposed TST has the ability to precisely localize the signals in time domain while maximizing the energy concentration in frequency domain. The TST can potentially be helpful in precise detection of event initiation and termination in signals such as heart rate signals, p and s waves in seismology, etc. The proposed BST has the ability to precisely localize the signals in a given band while maximizing the energy concentration in time domain. The BST is helpful in analysis of band-limited EEG signals and detection of harmonics in power quality disturbances.

In the second objective, the problem of maximally achievable energy concentration simultaneously in both time and frequency domains has been formulated for discrete time scenario. The maximum achievable trade-off between time and frequency domain energy concentration has been deduced. The obtained trade-off provides flexibility in designing the window according to required energy concentration in time and frequency domain. An optimal window, named OCDW for discrete time continuous frequency scenario has been proposed, and its application in IF estimation for multicomponent signal in noisy

environment has been shown. Similarly, an OCDW for discrete time discrete frequency scenario has also been proposed. The proposed OCDW has been extended to develop OST. A novel fair scaling criterion has also been proposed for OST. The performance of OST has been tested for detecting multiple power quality disturbances. The proposed OCDW has the ability to maximize the energy concentration in narrow intervals in both time and frequency domains. The proposed scaling criterion provides fair trade-off between time and frequency domain resolution.

The third objective of the thesis aims at designing asymmetrical window based ST for sharp detection of onset of events in signals. An AMKW has been proposed. The width parameter of conventional Kaiser window is modified to provide frequency dependent asymmetry. The proposed AMKW has been extended to design AMKW based ST. The performance of the proposed AMKW based ST has been shown in a case study for sharp detection of onset of seismic events in seismic signals. The proposed AMKW based ST provides sharp detection of events in front direction while having minimum degradation in backward direction. In the proposed AMKW based ST, there is minimum degradation in frequency resolution as compared to other existing asymmetrical window based STs for event detection.

In chapter 6, the ability of RM and SST to squeeze the spreaded energy to true IF coefficients has been discussed, and further incorporated in the OST. The reassigned and synchrosqueezing OST provide very narrow ridges in the TFR as compared to the OST. A novel concept of product-ST has also been proposed to improve the TFR visualization for closely spaced components in time and frequency. The proposed product-ST is obtained by multiplying the TFRs of TST and BST. The proposed product-ST has the ability to resolve very closely spaced signal components in time and frequency. The concept of RM and SST has also been introduced in the product-ST. The efficacy of the product-ST along with RM and SST has been illustrated in analysis of signals having multiple power quality disturbances. The proposed approach is able to detect closely spaced harmonics as well as very short interruptions.

7.2 Future Scope

Maximization of the energy concentration in TFR of linear transforms specially ST can lead to better analysis of practical signals of various disciplines. Accordingly, there is always a possibility for improvement in this area of research. With regard to the overall work presented in this thesis, following suggestions are stated for future investigations.

The proposed TST and BST in Chapter 3 are very effective variants of ST for analyzing the time-limited and band-limited signals. However, the used scaling criterion is linear

as used in conventional ST. New scaling criteria can be designed for further improving the time-frequency resolution in TST and BST.

The proposed OCDW in Chapter 4 can replace existing windows where very precise resolution is desired in both time and frequency domain. The window can be utilized in various applications such as ECG and EEG signal analysis, seismic signal analysis, machine fault detection, etc. The proposed approach for energy concentration maximization in time and frequency domain simultaneously can be extended to asymmetrical windows to facilitate sharp detection of events in time series.

The proposed AMKW based ST in Chapter 5 has the ability to sharply detect the onset of the events. The performance of AMKW based ST can be tested for detection of events' arrival in multiple power quality disturbances such as islanding, interruption, etc.

The proposed product-ST along with RM and SST in Chapter 6 has the ability to resolve very closely spaced signal components in time and frequency. The concept of high-order synchrosqueezing and reassignment can be also be used in product-ST for further improvement in time and frequency resolution.





Appendix

Lemma 1. Any eigenvector \mathbf{w}_i of the matrix \mathbf{P} corresponding to eigenvalue λ_i , satisfies

$$\mathbf{D}^i \mathbf{w}_i = \mathbf{0}_N \quad (7.1)$$

and

$$\mathbf{D}^i \mathbf{P} \mathbf{w}_i = \mathbf{0}_N \quad (7.2)$$

where $\mathbf{D}^i = (\lambda_i \mathbf{I}_N - \mathbf{P})^\dagger$. \mathbf{I}_N is an $N \times N$ identity matrix and $\mathbf{0}_N$ is an $N \times 1$ null vector.

Proof: The eigenvalue decomposition of \mathbf{P} can be represented as

$$\mathbf{P} = \mathbf{U} \mathbf{\Sigma} \mathbf{U}^T \quad (7.3)$$

where \mathbf{U} is an orthogonal matrix such that $\mathbf{U}^{-1} = \mathbf{U}^T$ and $\mathbf{U} \mathbf{U}^T = \mathbf{U}^T \mathbf{U} = \mathbf{I}_N$. The i^{th} column of \mathbf{U} denotes the eigenvector \mathbf{w}_i , and $\mathbf{\Sigma}$ is a diagonal matrix whose diagonal elements represent the corresponding eigenvalues, *i.e.* $[\mathbf{\Sigma}]_{i,i} = \lambda_i$. Using (7.3), \mathbf{D}^i can be represented as

$$\mathbf{D}^i = (\lambda_i \mathbf{I}_N - \mathbf{U} \mathbf{\Sigma} \mathbf{U}^T)^\dagger = \mathbf{U} \mathbf{R}^i \mathbf{U}^T \quad (7.4)$$

where $\mathbf{R}^i = (\lambda_i \mathbf{I}_N - \mathbf{\Sigma})^\dagger$ is a diagonal matrix whose diagonal elements can be represented as

$$[\mathbf{R}^i]_{jj} = \begin{cases} \frac{1}{\lambda_i - \lambda_j}, & i \neq j \\ 0, & i = j \end{cases} \quad (7.5)$$

Using (7.4), the LHS of (7.1) can be written as

$$\mathbf{D}^i \mathbf{w}_i = \mathbf{U} \mathbf{R}^i \mathbf{U}^T \mathbf{w}_i = \mathbf{U} \mathbf{R}^i \mathbf{d}^i \quad (7.6)$$

where $\mathbf{d}^i = \mathbf{U}^T \mathbf{w}_i$ is an $N \times 1$ vector, defined as

$$[\mathbf{d}^i]_j = \begin{cases} 1, & i = j \\ 0, & \text{elsewhere} \end{cases}$$

Since $\mathbf{R}^i \mathbf{d}^i = \mathbf{0}_N$, (7.6) leads to (7.1). Similarly by using (7.3) and (7.4), LHS of (7.2) can be written as

$$\mathbf{D}^i \mathbf{P} \mathbf{w}_i = \mathbf{U}(\lambda_i \mathbf{I}_N - \boldsymbol{\Sigma})^\dagger \mathbf{U}^T \mathbf{U} \boldsymbol{\Sigma} \mathbf{U}^T \mathbf{w}_i = \mathbf{U} \mathbf{C}^i \mathbf{d}^i \quad (7.7)$$

where $\mathbf{C}^i = (\lambda_i \mathbf{I}_N - \boldsymbol{\Sigma})^\dagger \boldsymbol{\Sigma}$ is a diagonal matrix whose diagonal elements can be represented as

$$[\mathbf{C}^i]_{j,j} = \begin{cases} \frac{\lambda_j}{\lambda_i - \lambda_j}, & i \neq j \\ 0, & i = j \end{cases} \quad (7.8)$$

Since $\mathbf{C}^i \mathbf{d}^i = \mathbf{0}_N$, (7.7) leads to (7.2).

Lemma 2. The first derivative of the eigenvalue λ_i associated with eigenvector \mathbf{w}_i of the matrix \mathbf{P} can be obtained as

$$\frac{d\lambda_i}{d\mu} = \mathbf{w}_i^T (-\mathbf{A}^{(B,N)} + \mathbf{T}^{(M,N)}) \mathbf{w}_i \quad (7.9)$$

and the first derivative of eigenvector \mathbf{w}_i can be obtained as

$$\frac{d\mathbf{w}_i}{d\mu} = \mathbf{D}^i (-\mathbf{A}^{(B,N)} + \mathbf{T}^{(M,N)}) \mathbf{w}_i \quad (7.10)$$

Proof: The eigenvalue equation of \mathbf{P} can be written as

$$\mathbf{P} \mathbf{w}_i = \lambda_i \mathbf{w}_i \quad (7.11)$$

Taking the first derivative of (7.11) with respect to μ , we obtain

$$\mathbf{P} \left(\frac{d\mathbf{w}_i}{d\mu} \right) + \left(\frac{d\mathbf{P}}{d\mu} \right) \mathbf{w}_i = \lambda_i \left(\frac{d\mathbf{w}_i}{d\mu} \right) + \left(\frac{d\lambda_i}{d\mu} \right) \mathbf{w}_i \quad (7.12)$$

Using the symmetric property of matrix \mathbf{P} , (7.11) can be rewritten as

$$\mathbf{w}_i^T \mathbf{P} = \lambda_i \mathbf{w}_i^T \quad (7.13)$$

Premultiplying (7.12) by \mathbf{w}_i^T and thereafter using (7.13), (7.12) leads to (7.9). Eq. (7.12) can be rearranged as

$$(\lambda_i \mathbf{I}_N - \mathbf{P}) \left(\frac{d\mathbf{w}_i}{d\mu} \right) = \left(\frac{d\mathbf{P}}{d\mu} \right) \mathbf{w}_i - \left(\frac{d\lambda_i}{d\mu} \right) \mathbf{w}_i \quad (7.14)$$

Premultiplying (7.14) by \mathbf{D}^i , and thereafter using (7.1) leads to (7.10).

Theorem 1. For large values of N (ideally $N \rightarrow \infty$), following properties hold true.

1. $\mathbf{A}^{(B,N)} \mathbf{A}^{(B,N)} = \mathbf{A}^{(B,N)}$
2. $\alpha^2 + \beta^2 - 2\alpha\beta\sqrt{\lambda_0^{(M)}} = 1 - \lambda_0^{(M)}$, where $\lambda_0^{(M)}$ is the maximum eigenvalue of matrix $\mathbf{A}^{(B,M)}$
3. The maximum value of product $(\alpha^2\beta^2)$ is achieved at $\mu = 0.5$, where $\alpha^2 = \beta^2$ ($\mu_{\text{opt}} = \mu_{\text{eq}} = 0.5$).

Proof: The eigenvalue decomposition of matrix $\mathbf{A}^{(B,N)}$ can be represented as $\mathbf{A}^{(B,N)} = \bar{\mathbf{U}}\bar{\Sigma}\bar{\mathbf{U}}^T$ where $\bar{\mathbf{U}}$ is an orthonormal matrix such that $\bar{\mathbf{U}}^T\bar{\mathbf{U}} = \mathbf{I}_N$, and $\bar{\Sigma}$ is a diagonal matrix containing eigenvalues of $\mathbf{A}^{(B,N)}$ as diagonal elements. For large values of N , all eigenvalues of $\mathbf{A}^{(B,N)}$ cluster around 0 or 1 [174]. It implies that $\bar{\Sigma}^2 = \bar{\Sigma}$. Thus, $\mathbf{A}^{(B,N)} \mathbf{A}^{(B,N)}$ can be evaluated as

$$\mathbf{A}^{(B,N)} \mathbf{A}^{(B,N)} = \bar{\mathbf{U}}\bar{\Sigma}\bar{\mathbf{U}}^T \bar{\mathbf{U}}\bar{\Sigma}\bar{\mathbf{U}}^T = \bar{\mathbf{U}}\bar{\Sigma}^2\bar{\mathbf{U}}^T = \mathbf{A}^{(B,N)}$$

Pre-multiplying (4.19) by $\mathbf{T}^{(M,N)}$ leads to

$$(1 - \mu)\mathbf{T}^{(M,N)} \mathbf{A}^{(B,N)} \mathbf{w}_0 = (\lambda_0 - \mu)\mathbf{T}^{(M,N)} \mathbf{w}_0 \quad (7.15)$$

Similarly, pre-multiplication of $\mathbf{A}^{(B,N)}$ to (4.19) results in

$$\mu \mathbf{A}^{(B,N)} \mathbf{T}^{(M,N)} \mathbf{w}_0 = (\lambda_0 - (1 - \mu)) \mathbf{A}^{(B,N)} \mathbf{w}_0 \quad (7.16)$$

Using (4.19) and (7.16), we can obtain

$$\mathbf{T}^{(M,N)} \mathbf{A}^{(B,N)} \mathbf{T}^{(M,N)} \mathbf{w}_0 = \lambda_0^{(M)} \mathbf{T}^{(M,N)} \mathbf{w}_0 \quad (7.17)$$

where

$$\lambda_0^{(M)} = \frac{(\lambda_0 - \mu)(\lambda_0 - (1 - \mu))}{\mu(1 - \mu)} \quad (7.18)$$

denotes the maximum eigenvalue of matrix $\mathbf{A}^{(B,M)}$. Pre-multiplying (4.19), (7.15) and (7.16) with \mathbf{w}_0^T , we obtain

$$(1 - \mu)\beta^2 + \mu\alpha^2 = \lambda_0 \quad (7.19)$$

$$(1 - \mu)\mathbf{w}_0^T \mathbf{T}^{(M,N)} \mathbf{A}^{(B,N)} \mathbf{w}_0 = (\lambda_0 - \mu)\alpha^2 \quad (7.20)$$

$$\mu \mathbf{w}_0^T \mathbf{A}^{(B,N)} \mathbf{T}^{(M,N)} \mathbf{w}_0 = (\lambda_0 - (1 - \mu))\beta^2 \quad (7.21)$$

Since $\mathbf{w}_0^T \mathbf{T}^{(M,N)} \mathbf{A}^{(B,N)} \mathbf{w}_0 = \mathbf{w}_0^T \mathbf{A}^{(B,N)} \mathbf{T}^{(M,N)} \mathbf{w}_0$, from (7.20) and (7.21), we obtain

$$\frac{(\lambda_0 - \mu)}{(1 - \mu)} \alpha^2 = \frac{(\lambda_0 - (1 - \mu))}{\mu} \beta^2 \quad (7.22)$$

Substituting (7.19) in (7.22), we get

$$\mu = \frac{\beta \sqrt{1 - \beta^2}}{\alpha \sqrt{1 - \alpha^2} + \beta \sqrt{1 - \beta^2}} \quad (7.23)$$

Substituting (7.19) and (7.23) in (7.18), we obtain

$$\alpha^2 + \beta^2 - 2\alpha\beta\sqrt{\lambda_0^{(M)}} = 1 - \lambda_0^{(M)} \quad (7.24)$$

This represents the theoretical upper bound on simultaneously achievable energy concentrations [57]. Substituting (7.23) in (4.26), results in $\alpha^2 = \beta^2$. Therefore, $\mu = 0.5$ maximizes the product $(\alpha^2 \beta^2)$ of time and frequency domain energy concentrations.

Lemma 3. $\mathbf{B}^{(L,N)} \mathbf{B}^{(L,N)} = \mathbf{B}^{(L,N)}$

Proof: The $(m, n)^{th}$ element of matrix $\mathbf{B}^{(L,N)} \mathbf{B}^{(L,N)}$ can be represented as

$$\begin{aligned} & [\mathbf{B}^{(L,N)} \mathbf{B}^{(L,N)}]_{m,n} \\ &= \frac{1}{N^2} \sum_{p=1}^N \sum_{a=-L}^L \sum_{b=-L}^L e^{j2\pi am} e^{-j2\pi ap} e^{j2\pi bp} e^{-j2\pi bn} \\ &= \frac{1}{N^2} \sum_{a=-L}^L \sum_{b=-L}^L e^{j2\pi am} e^{-j2\pi bn} (N\delta(a-b)) \\ &= \frac{1}{N} \sum_{k=-L}^L e^{j2\pi a[m-n]} \quad (\text{using } a=b=k) \\ &= [\mathbf{B}^{L,N}]_{m,n} \end{aligned} \quad (7.25)$$

where $\delta(\cdot)$ represents Kronecker delta function.

Bibliography

- [1] S. Deb and S. Dandapat, "Fourier model based features for analysis and classification of out-of-breath speech," *Speech Communication*, vol. 90, pp. 1–14, June 2017.
- [2] B. Boashash, *Time-frequency signal analysis and processing: A comprehensive reference*. Academic Press, 2015.
- [3] S. M. Mohammadi, S. Kouchaki, M. Ghavami, and S. Sanei, "Improving time-frequency domain sleep EEG classification via singular spectrum analysis," *Journal of Neuroscience Methods*, vol. 273, pp. 96 – 106, 2016.
- [4] M. Azarbad, H. Azami, S. Sanei, and A. Ebrahimzadeh, "A time-frequency approach for EEG signal segmentation," *Journal of AI and Data Mining*, vol. 2, no. 1, pp. 63–71, 2014.
- [5] F. Hlawatsch and G. F. Boudreaux-Bartels, "Linear and quadratic time-frequency signal representations," *IEEE Signal Processing Magazine*, vol. 9, no. 2, pp. 21–67, April 1992.
- [6] Hae-Gil Hwang, Hyun-Ju Choi, Byoung-Doo Kang, Hye-Kyoung Yoon, Hee-Cheol Kim, Sang-Kyoon Kim, and Heung-Kook Choi, "Classification of breast tissue images based on wavelet transform using discriminant analysis, neural network and SVM," in *7th International Workshop on Enterprise networking and Computing in Healthcare Industry (HEALTHCOM)*, June 2005, pp. 345–349.
- [7] J. Seshadrinath, B. Singh, and B. K. Panigrahi, "Investigation of vibration signatures for multiple fault diagnosis in variable frequency drives using complex wavelets," *IEEE Transactions on Power Electronics*, vol. 29, no. 2, pp. 936–945, Feb 2014.
- [8] M. Sharma, A. Dhere, R. B. Pachori, and U. R. Acharya, "An automatic detection of focal EEG signals using new class of time-frequency localized orthogonal wavelet filter banks," *Knowledge-Based Systems*, vol. 118, pp. 217–227, 2017.

- [9] R. G. Stockwell, L. Mansinha, and R. P. Lowe, "Localization of the complex spectrum: The S-transform," *IEEE Transactions on Signal Processing*, vol. 44, no. 4, pp. 998–1001, Apr 1996.
- [10] N. V. George, "S transform: Time frequency analysis & filtering," Ph.D. dissertation, 2009.
- [11] P. K. Dash, B. K. Panigrahi, and G. Panda, "Power quality analysis using S-transform," *IEEE Transactions on Power Delivery*, vol. 18, no. 2, pp. 406–411, April 2003.
- [12] R. B. Pachori and P. Sircar, "A new technique to reduce cross terms in the Wigner distribution," *Digital Signal Processing*, vol. 17, no. 2, pp. 466–474, 2007.
- [13] N. Liu, J. Gao, B. Zhang, F. Li, and Q. Wang, "Time-frequency analysis of seismic data using a three parameters S-transform," *IEEE Geoscience and Remote Sensing Letters*, vol. 15, no. 1, pp. 142–146, Jan 2018.
- [14] W. Xue, J. Zhu, X. Rong, Y. Huang, Y. Yang, and Y. Yu, "The analysis of ground penetrating radar signal based on generalized S- transform with parameters optimization," *Journal of Applied Geophysics*, vol. 140, pp. 75 – 83, May 2017.
- [15] N. V. George, K. F. Tiampo, S. S. Sahu, S. Mazzotti, L. Mansinha, and G. Panda, "Identification of glacial isostatic adjustment in eastern Canada using S transform filtering of GPS observations," *Pure and Applied Geophysics*, vol. 169, no. 8, pp. 1507–1517, Aug 2012.
- [16] N. V. George, S. S. Sahu, L. Mansinha, K. F. Tiampo, and G. Panda, "Time localised band filtering using modified S-transform," in *International Conference on Signal Processing Systems*, May 2009, pp. 42–46.
- [17] S. Mishra, C. N. Bhende, and B. K. Panigrahi, "Detection and classification of power quality disturbances using S-transform and probabilistic neural network," *IEEE Transactions on Power Delivery*, vol. 23, no. 1, pp. 280–287, Jan 2008.
- [18] J. Li, Z. Teng, Q. Tang, and J. Song, "Detection and classification of power quality disturbances using double resolution S-transform and DAG-SVMs," *IEEE Transactions on Instrumentation and Measurement*, vol. 65, no. 10, pp. 2302–2312, Oct 2016.
- [19] M. V. Reddy and R. Sodhi, "A modified S-transform and random forests-based power quality assessment framework," *IEEE Transactions on Instrumentation and Measurement*, vol. 67, no. 99, pp. 78–89, Nov 2017.

- [20] L. Mansinha, R. Stockwell, R. Lowe, M. Eramian, and R. Schincariol, "Local S-spectrum analysis of 1-D and 2-D data," *Physics of the Earth and Planetary Interiors*, vol. 103, no. 3, pp. 329 – 336, Nov 1997.
- [21] K. F. Tiampo, D. Assefa, J. Fernandez, L. Mansinha, and H. Rasmussen, "Post seismic deformation following the 1994 Northridge earthquake identified using the localized Hartley transform filter," *Pure and Applied Geophysics*, vol. 165, no. 8, pp. 1577–1602, 2008.
- [22] P. K. Dash, B. K. Panigrahi, D. K. Sahoo, and G. Panda, "Power quality disturbance data compression, detection, and classification using integrated spline wavelet and S-transform," *IEEE Transactions on Power Delivery*, vol. 18, no. 2, pp. 595–600, April 2003.
- [23] S. R. Samantaray, B. K. Panigrahi, P. K. Dash, and G. Panda, "Power transformer protection using S-transform with complex window and pattern recognition approach," *IET Generation, Transmission Distribution*, vol. 1, no. 2, pp. 278–286, March 2007.
- [24] S. R. Samantaray, A. Samui, and B. Chitti Babu, "S-transform based cumulative sum detector (CUSUM) for islanding detection in distributed generations," in *2010 Joint International Conference on Power Electronics, Drives and Energy Systems Power India*, Dec 2010, pp. 1–6.
- [25] S. R. Samantaray, A. Samui, and B. C. Babu, "Time-frequency transform-based islanding detection in distributed generation," *IET Renewable Power Generation*, vol. 5, no. 6, pp. 431–438, November 2011.
- [26] B. Biswal, "ECG signal analysis using modified S-transform," *Healthcare Technology Letters*, vol. 4, no. 2, pp. 68–72, May 2017.
- [27] J. R. Mitchell, T. C. Fong, B. G. Goodyear, and H. Zhu, "Filtering artifact from fMRI data using the Stockwell transform," Mar. 10 2009, uS Patent 7,502,526.
- [28] J. R. Mitchell, T. C. Fong, R. Brown, and H. Zhu, "Distributed vector processing of the S transform for medical applications," Jul. 31 2007, uS Patent 7,251,379.
- [29] B. G. Goodyear, H. Zhu, R. A. Brown, and J. R. Mitchell, "Removal of phase artifacts from fMRI data using a Stockwell transform filter improves brain activity detection," *Magnetic Resonance in Medicine: An Official Journal of the International Society for Magnetic Resonance in Medicine*, vol. 51, no. 1, pp. 16–21, 2004.

- [30] S. Drabycz, R. G. Stockwell, and J. R. Mitchell, "Image texture characterization using the discrete orthonormal S-transform," *Journal of Digital Imaging*, vol. 22, no. 6, p. 696, Aug 2008.
- [31] K. Eftaxias and S. Sanei, "Discrimination of task-related EEG signals using diffusion adaptation and S-transform coherency," in *2014 IEEE International Workshop on Machine Learning for Signal Processing (MLSP)*, Sep. 2014, pp. 1–6.
- [32] A. Chatterjee, R. Fournier, A. Nait-Ali, and P. Siarry, "A postural information-based biometric authentication system employing S-transform, radial basis function network, and extended Kalman filtering," *IEEE Transactions on Instrumentation and Measurement*, vol. 59, no. 12, pp. 3131–3138, Dec 2010.
- [33] K. Gröchenig, *Foundations of time-frequency analysis*. Springer Science & Business Media, 2013.
- [34] S. C. Pei and S. G. Huang, "STFT with adaptive window width based on the chirp rate," *IEEE Transactions on Signal Processing*, vol. 60, no. 8, pp. 4065–4080, Aug 2012.
- [35] S. S. Sahu, G. Panda, and N. V. George, "An improved S-transform for time-frequency analysis," in *IEEE International Advance Computing Conference*, March 2009, pp. 315–319.
- [36] S. Agrawal, N. V. George, and A. Prashant, "GPR data analysis of weak signals using modified S-transform," *Geotechnical and Geological Engineering*, vol. 33, no. 5, pp. 1167–1182, 2015.
- [37] L. Tripathy, S. R. Samantaray, and P. K. Dash, "Sparse S-transform for location of faults on transmission lines operating with unified power flow controller," *IET Generation, Transmission Distribution*, vol. 9, no. 15, pp. 2108–2116, 2015.
- [38] S. Samantaray, "Fast S-transform based distance relaying in transmission line," *Electric Power Systems Research*, vol. 95, pp. 268–274, 2013.
- [39] I. Djurović, E. Sejdić, and J. Jiang, "Frequency-based window width optimization for S-transform," *International Journal of Electronics and Communications*, vol. 62, no. 4, pp. 245 – 250, 2008.
- [40] E. Sejdić, I. Djurović, and J. Jiang, "A window width optimized S-transform," *EURASIP Journal on Advances in Signal Processing*, vol. 2008, no. 1, pp. 1–13, Dec 2007.

- [41] C. R. Pinnegar and L. Mansinha, “The Bi-Gaussian S-transform,” *SIAM J. Sci. Comput.*, vol. 24, no. 5, pp. 1678–1692, May 2002.
- [42] ———, “The S-transform with windows of arbitrary and varying shape,” *Geophysics*, vol. 68, no. 1, pp. 381–385, 2003.
- [43] W. Yao, Z. Teng, Q. Tang, and P. Zuo, “Adaptive dolph-chebyshev window-based S-transform in time-frequency analysis,” *IET Signal Processing*, vol. 8, no. 9, pp. 927–937, Dec 2014.
- [44] C. Simon, S. Ventosa, M. Schimmel, A. Heldring, J. J. Danobeitia, J. Gallart, and A. Manuel, “The S-transform and its inverses: Side effects of discretizing and filtering,” *IEEE Transactions on Signal Processing*, vol. 55, no. 10, pp. 4928–4937, Oct 2007.
- [45] F. Auger and P. Flandrin, “Improving the readability of time-frequency and time-scale representations by the reassignment method,” *IEEE Transactions on Signal Processing*, vol. 43, no. 5, pp. 1068–1089, 1995.
- [46] F. Auger, P. Flandrin, Y. Lin, S. McLaughlin, S. Meignen, T. Oberlin, and H. Wu, “Time-frequency reassignment and synchrosqueezing: An overview,” *IEEE Signal Processing Magazine*, vol. 30, no. 6, pp. 32–41, Nov 2013.
- [47] Q. Wang, J. Gao, N. Liu, and X. Jiang, “High-resolution seismic time-frequency analysis using the synchrosqueezing generalized S-transform,” *IEEE Geoscience and Remote Sensing Letters*, vol. 15, no. 3, pp. 374–378, March 2018.
- [48] W. Liu, S. Cao, Z. Wang, K. Jiang, Q. Zhang, and Y. Chen, “A novel approach for seismic time-frequency analysis based on high-order synchrosqueezing transform,” *IEEE Geoscience and Remote Sensing Letters*, vol. 15, no. 8, pp. 1159–1163, Aug 2018.
- [49] I. Daubechies, J. Lu, and H.-T. Wu, “Synchrosqueezed wavelet transforms: An empirical mode decomposition-like tool,” *Applied and Computational Harmonic Analysis*, vol. 30, no. 2, pp. 243–261, 2011.
- [50] G. Thakur, E. Brevdo, N. S. Fučkar, and H.-T. Wu, “The synchrosqueezing algorithm for time-varying spectral analysis: Robustness properties and new paleoclimate applications,” *Signal Processing*, vol. 93, no. 5, pp. 1079–1094, 2013.
- [51] T. Oberlin, S. Meignen, and V. Perrier, “The Fourier-based synchrosqueezing transform,” in *2014 IEEE International Conference on Acoustics, Speech and Signal Processing (ICASSP)*, 2014, pp. 315–319.

- [52] S. Barma, B. W. Chen, W. Ji, F. Jiang, and J. F. Wang, "Measurement of duration, energy of instantaneous frequencies, and splits of subcomponents of the second heart sound," *IEEE Transactions on Instrumentation and Measurement*, vol. 64, no. 7, pp. 1958–1967, July 2015.
- [53] Z. Cheng, W. Chen, Y. Chen, Y. Liu, W. Liu, H. Li, and R. Yang, "Application of bi-Gaussian S-transform in high-resolution seismic time-frequency analysis," *Interpretation*, vol. 5, no. 1, pp. SC1–SC7, Oct 2016.
- [54] S. Azadi and A. A. Safavi, "S-transform based P-wave and S-wave arrival times measurements toward earthquake locating," *2nd IEEE International Conference on Control, Instrumentation and Automation (ICCIA)*, pp. 241–246, Dec 2011.
- [55] A. Bhattacharyya and R. B. Pachori, "A multivariate approach for patient-specific EEG seizure detection using empirical wavelet transform," *IEEE Transactions on Biomedical Engineering*, vol. 64, no. 9, pp. 2003–2015, Sep. 2017.
- [56] D. Slepian and H. O. Pollak, "Prolate spheroidal wave functions, Fourier analysis and uncertainty-I," *The Bell System Technical Journal*, vol. 40, no. 1, pp. 43–63, Jan 1961.
- [57] D. Slepian, "Prolate spheroidal wave functions, Fourier analysis and uncertainty-V: the discrete case," *The Bell System Technical Journal*, vol. 57, no. 5, pp. 1371–1430, May 1978.
- [58] W. Zong, G. B. Moody, and D. Jiang, "A robust open-source algorithm to detect onset and duration of QRS complexes," in *Computers in Cardiology*, Sep. 2003, pp. 737–740.
- [59] C. R. Pinnegar and L. Mansinha, "The bi-Gaussian S-transform," *SIAM Journal on Scientific Computing*, vol. 24, no. 5, pp. 1678–1692, May 2003.
- [60] J. Akram and D. W. Eaton, "Refinement of arrival-time picks using a cross-correlation based workflow," *Journal of Applied Geophysics*, vol. 135, no. 1, pp. 55–66, Dec 2016.
- [61] A. M. Sykulski, S. C. Olhede, and J. M. Lilly, "A widely linear complex autoregressive process of order one," *IEEE Transactions on Signal Processing*, vol. 64, no. 23, pp. 6200–6210, Dec 2016.
- [62] M. Zhu, L. Wang, X. Liu, J. Zhao, and P. Peng, "Accurate identification of microseismic P- and S-phase arrivals using the multi-step AIC algorithm," *Journal of Applied Geophysics*, vol. 150, no. 1, pp. 284 – 293, Mar 2018.

- [63] Z. E. Ross and Y. Ben-Zion, "Automatic picking of direct P, S seismic phases and fault zone head waves," *Geophysical Journal International*, vol. 199, no. 1, pp. 368–381, Aug 2014.
- [64] X. Li, X. Shang, Z. Wang, L. Dong, and L. Weng, "Identifying P-phase arrivals with noise: An improved Kurtosis method based on DWT and STA/LTA," *Journal of Applied Geophysics*, vol. 133, pp. 50 – 61, Oct 2016.
- [65] W. Liu, S. Cao, and Y. Chen, "Seismic time-frequency analysis via empirical wavelet transform," *IEEE Geoscience and Remote Sensing Letters*, vol. 13, no. 1, pp. 28–32, Jan 2016.
- [66] Z. Cheng, Y. Chen, Y. Liu, W. Liu, G. Zhang, H. Li, and W. Chen, "Seismic time-frequency analysis using bi-Gaussian S transform," in *78th EAGE Conference and Exhibition*, May 2016.
- [67] S. V. Samsonov, K. F. Tiampo, A. G. Camacho, J. Fernández, and P. J. González, "Spatiotemporal analysis and interpretation of 1993–2013 ground deformation at Campi Flegrei, Italy, observed by advanced DInSAR," *Geophysical Research Letters*, vol. 41, no. 17, pp. 6101–6108, 2014.
- [68] A. Ashrafian, M. Rostami, and G. Gharehpetian, "Hyperbolic S-transform-based method for classification of external faults, incipient faults, inrush currents and internal faults in power transformers," *IET generation, transmission & distribution*, vol. 6, no. 10, pp. 940–950, Oct 2012.
- [69] P. K. Ray, S. R. Mohanty, N. Kishor, and J. P. Catalão, "Optimal feature and decision tree-based classification of power quality disturbances in distributed generation systems," *IEEE Transactions on Sustainable Energy*, vol. 5, no. 1, pp. 200–208, Jan 2014.
- [70] S. Wang, X. Chen, C. Tong, and Z. Zhao, "Matching synchrosqueezing wavelet transform and application to aeroengine vibration monitoring," *IEEE Transactions on Instrumentation and Measurement*, vol. 66, no. 2, pp. 360–372, Feb 2017.
- [71] Z. Huang, J. Zhang, T. Zhao, and Y. Sun, "Synchrosqueezing S-transform and its application in seismic spectral decomposition," *IEEE Transactions on Geoscience and Remote Sensing*, vol. 54, no. 2, pp. 817–825, Feb 2016.
- [72] R. Anvari, M. A. Nazari Siahsar, S. Gholtashi, A. Roshandel Kahoo, and M. Mohammadi, "Seismic random noise attenuation using synchrosqueezed wavelet

- transform and low-rank signal matrix approximation,” *IEEE Transactions on Geoscience and Remote Sensing*, vol. 55, no. 11, pp. 6574–6581, Nov 2017.
- [73] H. Wu, S. Hseu, M. Bien, Y. R. Kou, and I. Daubechies, “Evaluating physiological dynamics via synchrosqueezing: Prediction of ventilator weaning,” *IEEE Transactions on Biomedical Engineering*, vol. 61, no. 3, pp. 736–744, March 2014.
- [74] G. Yu, Z. Wang, and P. Zhao, “Multisynchrosqueezing transform,” *IEEE Transactions on Industrial Electronics*, vol. 66, no. 7, pp. 5441–5455, July 2019.
- [75] S. C. Bradford, “Time-frequency analysis of systems with changing dynamic properties,” 2006.
- [76] J. P. Amezcuita-Sanchez and H. Adeli, “Signal processing techniques for vibration-based health monitoring of smart structures,” *Archives of Computational Methods in Engineering*, vol. 23, no. 1, pp. 1–15, Mar 2016.
- [77] R. Kumar, P. Sumathi, and A. Kumar, “Synchrosqueezing transform-based frequency shifting detection for earthquake-damaged structures,” *IEEE Geoscience and Remote Sensing Letters*, vol. 14, no. 8, pp. 1393–1397, Aug 2017.
- [78] P. Bloomfield, *Fourier analysis of time series: An introduction*. John Wiley & Sons, 2004.
- [79] A.-C. Tsai, J.-J. Luh, and T.-T. Lin, “A novel STFT-ranking feature of multi-channel EMG for motion pattern recognition,” *Expert Systems with Applications*, vol. 42, no. 7, pp. 3327 – 3341, May 2015.
- [80] S. Kara, “Classification of mitral stenosis from Doppler signals using short time Fourier transform and artificial neural networks,” *Expert Systems with Applications*, vol. 33, no. 2, pp. 468 – 475, Aug 2007.
- [81] T. Bendory, Y. C. Eldar, and N. Boumal, “Non-convex phase retrieval from STFT measurements,” *IEEE Transactions on Information Theory*, vol. 64, no. 1, pp. 467–484, Jan 2018.
- [82] J.-D. Wu and C.-K. Huang, “An engine fault diagnosis system using intake manifold pressure signal and Wigner-Ville distribution technique,” *Expert Systems with Applications*, vol. 38, no. 1, pp. 536 – 544, Jan 2011.
- [83] D. D. Yong, S. Bhowmik, and F. Magnago, “An effective power quality classifier using wavelet transform and support vector machines,” *Expert Systems with Applications*, vol. 42, no. 15, pp. 6075 – 6081, Sep 2015.

- [84] O. Alpar, "Online signature verification by continuous wavelet transformation of speed signals," *Expert Systems with Applications*, vol. 104, pp. 33 – 42, Aug 2018.
- [85] M. R. Portnoff, "Time-frequency representation of digital signals and systems based on short-time Fourier analysis," *IEEE Transactions on Acoustics, Speech and Signal Processing*, Feb. 1980.
- [86] N. E. Huang, Z. Shen, S. R. Long, M. C. Wu, H. H. Shih, Q. Zheng, N.-C. Yen, C. C. Tung, and H. H. Liu, "The empirical mode decomposition and the Hilbert spectrum for nonlinear and non-stationary time series analysis," *Proceedings of the Royal Society of London. Series A: Mathematical, Physical and Engineering Sciences*, vol. 454, no. 1971, pp. 903–995, 1998.
- [87] R. B. Pachori, "Discrimination between ictal and seizure-free EEG signals using empirical mode decomposition," *Research Letters in Signal Processing*, vol. 2008, p. 14, 2008.
- [88] A. W. Rihaczek and E. Bedrosian, "Hilbert transforms and the complex representation of real signals," *Proceedings of the IEEE*, vol. 54, no. 3, pp. 434–435, 1966.
- [89] M. E. Torres, M. A. Colominas, G. Schlotthauer, and P. Flandrin, "A complete ensemble empirical mode decomposition with adaptive noise," in *2011 IEEE International Conference on Acoustics, Speech and Signal Processing (ICASSP)*, 2011, pp. 4144–4147.
- [90] A. Upadhyay and R. B. Pachori, "Speech enhancement based on mEMD-VMD method," *Electronics Letters*, vol. 53, no. 7, pp. 502–504, 2017.
- [91] I. Daubechies, "The wavelet transform, time-frequency localization and signal analysis," *IEEE Transactions on Information Theory*, Sep 1990.
- [92] —, *Ten lectures on wavelets*. Siam, 1992, vol. 61.
- [93] R. Katiyar, V. Gupta, and R. B. Pachori, "FBSE-EWT-based approach for the determination of respiratory rate from PPG signals," *IEEE Sensors Letters*, vol. 3, no. 7, pp. 1–4, July 2019.
- [94] S. Patidar and R. B. Pachori, "Segmentation of cardiac sound signals by removing murmurs using constrained tunable-Q wavelet transform," *Biomedical Signal Processing and Control*, vol. 8, no. 6, pp. 559 – 567, 2013.
- [95] S. Mann and S. Haykin, "The chirplet transform: physical considerations," *IEEE Transactions on Signal Processing*, vol. 43, no. 11, pp. 2745–2761, Nov 1995.

- [96] Jean-Luc Starck, E. J. Candes, and D. L. Donoho, “The curvelet transform for image denoising,” *IEEE Transactions on Image Processing*, vol. 11, no. 6, pp. 670–684, June 2002.
- [97] L. Mansinha, R. Stockwell, and R. Lowe, “Pattern analysis with two-dimensional spectral localisation: Applications of two-dimensional S transforms,” *Physica A: Statistical Mechanics and its Applications*, vol. 239, no. 1-3, pp. 286–295, 1997.
- [98] M. Uyar, S. Yildirim, and M. T. Gencoglu, “An expert system based on S-transform and neural network for automatic classification of power quality disturbances,” *Expert Systems with Applications*, vol. 36, no. 3, Part 2, pp. 5962 – 5975, Apr 2009.
- [99] A. F. Abidin, A. Mohamed, and H. Shareef, “Intelligent detection of unstable power swing for correct distance relay operation using S-transform and neural networks,” *Expert Systems with Applications*, vol. 38, no. 12, pp. 14969 – 14975, 2011. [Online]. Available: <http://www.sciencedirect.com/science/article/pii/S0957417411008347>
- [100] M. E. Salem, A. Mohamed, and S. A. Samad, “Rule based system for power quality disturbance classification incorporating S-transform features,” *Expert Systems with Applications*, vol. 37, no. 4, pp. 3229 – 3235, Apr 2010.
- [101] P. Sánchez, F. G. Montoya, F. Manzano-Agugliaro, and C. Gil, “Genetic algorithm for S-transform optimisation in the analysis and classification of electrical signal perturbations,” *Expert Systems with Applications*, vol. 40, no. 17, pp. 6766 – 6777, Dec 2013.
- [102] S. Assous and B. Boashash, “Evaluation of the modified S-transform for time-frequency synchrony analysis and source localisation,” *EURASIP Journal on Advances in Signal Processing*, vol. 2012, no. 1, p. 49, Feb 2012.
- [103] T. Zhang, W. Chen, and M. Li, “Generalized Stockwell transform and SVD-based epileptic seizure detection in EEG using random forest,” *Biocybernetics and Biomedical Engineering*, vol. 38, no. 3, pp. 519–534, Jan 2018.
- [104] R. G. Stockwell, “Why use the S-transform?” in *Pseudo-Differential Operators: PDEs and Time-Frequency Analysis*, ser. Fields Institute Communications, Wong, Ed. AMS, 2007, pp. 279–309.
- [105] J. Ma and J. Jiang, “Analysis and design of modified window shapes for S-transform to improve time-frequency localization,” *Mechanical Systems and Signal Processing*, vol. 58-59, pp. 271 – 284, June 2015.

- [106] D. Li and J. Castagna, "Modified S-transform in time-frequency analysis of seismic data," *SEG Technical Program Expanded Abstracts*, pp. 4629–4634, Sep 2013.
- [107] Z. Cheng, W. Chen, Y. Chen, Y. Liu, W. Liu, H. Li, and R. Yang, "Application of bi-Gaussian S-transform in high-resolution seismic time-frequency analysis," *Interpretation*, vol. 5, no. 1, pp. SC1–SC7, Feb 2017.
- [108] L. Wei, R. A. Kennedy, and T. A. Lamaheva, "An optimal basis of band-limited functions for signal analysis and design," *IEEE Transactions on Signal Processing*, vol. 58, no. 11, pp. 5744–5755, Nov 2010.
- [109] H. J. Landau and H. O. Pollak, "Prolate spheroidal wave functions, Fourier analysis and uncertainty-II," *The Bell System Technical Journal*, vol. 40, no. 1, pp. 65–84, Jan 1961.
- [110] W. Y. Xu and C. Chamzas, "On the periodic discrete prolate spheroidal sequences," *SIAM Journal on Applied Mathematics*, vol. 44, no. 6, pp. 1210–1217, 1984.
- [111] S. Pei and J. Ding, "Discrete-to-discrete prolate spheroidal wave functions and finite duration discrete fractional Fourier transform," *15th European Signal Processing Conference, Poznan, Poland, Sep.*, pp. 2244–2248, Sep. 2007.
- [112] L. F. Chaparro, E. Sejdic, A. Can, O. A. Alkishriwo, S. Senay, and A. Akan, "Asynchronous representation and processing of nonstationary signals: A time-frequency framework," *IEEE Signal Processing Magazine*, vol. 30, no. 6, pp. 42–52, 2013.
- [113] Q. Li and J. Gao, "Application of seismic data stacking in time-frequency domain," *IEEE Geoscience and Remote Sensing Letters*, vol. 11, no. 9, pp. 1484–1488, Sep. 2014.
- [114] Y. Chen and S. Fomel, "Random noise attenuation using local signal-and-noise orthogonalization," *Geophysics*, vol. 80, no. 6, pp. WD1–WD9, Mar 2015.
- [115] S. Fomel, "Seismic data decomposition into spectral components using regularized nonstationary autoregression," *Geophysics*, vol. 78, no. 6, pp. O69–O76, Oct 2013.
- [116] G. Pfurtscheller and F. L. da Silva, "Event-related EEG/MEG synchronization and desynchronization: Basic principles," *Clinical Neurophysiology*, vol. 110, no. 11, pp. 1842 – 1857, Nov 1999.
- [117] C. Brunner, M. Naeem, R. Leeb, B. Graimann, and G. Pfurtscheller, "Spatial filtering and selection of optimized components in four class motor imagery EEG

- data using independent components analysis,” *Pattern Recognition Letters*, vol. 28, no. 8, pp. 957–964, Jun 2007.
- [118] R. Kumar, B. Singh, D. T. Shahani, A. Chandra, and K. Al-Haddad, “Recognition of power-quality disturbances using S-transform-based ANN classifier and rule-based decision tree,” *IEEE Transactions on Industry Applications*, vol. 51, no. 2, pp. 1249–1258, March 2015.
- [119] M. V. Reddy and R. Sodhi, “A rule-based S-transform and AdaBoost based approach for power quality assessment,” *Electric Power Systems Research*, vol. 134, pp. 66 – 79, May 2016.
- [120] J. C. Smith, G. Hensley, and L. Ray, “IEEE recommended practice for monitoring electric power quality,” *IEEE Std*, pp. 1159–1995, 1995.
- [121] D. Slepian, “On bandwidth,” *Proceedings of the IEEE*, vol. 64, no. 3, pp. 292–300, 1976.
- [122] A. Papoulis and M. Bertran, “Digital filtering and prolate functions,” *IEEE Transactions on Circuit Theory*, vol. 19, no. 6, pp. 674–681, November 1972.
- [123] T. Verma, S. Bilbao, and T. H. Y. Meng, “The digital prolate spheroidal window,” in *IEEE International Conference on Acoustics, Speech, and Signal Processing*, Atlanta, GA, USA, May 1996, May, pp. 1351–1354.
- [124] A. Papoulis, “Minimum-bias windows for high-resolution spectral estimates,” *IEEE Transactions on Information Theory*, vol. 19, no. 1, pp. 9–12, January 1973.
- [125] A. Jain and S. Ranganath, “Extrapolation algorithms for discrete signals with application in spectral estimation,” *IEEE Transactions on Acoustics, Speech, and Signal Processing*, vol. 29, no. 4, pp. 830–845, August 1981.
- [126] G. G. Walter and X. Shen, “Wavelets Based on Prolate Spheroidal Wave Functions,” *Journal of Fourier Analysis and Applications*, vol. 10, no. 1, pp. 1–26, 2004.
- [127] L. Faping, W. Hongxing, L. Xiao, L. Chuanhui, K. Jiafang, and M. Xingji, “Time-frequency characteristics of PSWF with Wigner-Ville distributions,” in *IEEE International Conference on Signal and Image Processing*, Beijing, China, Aug 2016, Aug, pp. 568–572.
- [128] S. Pei and P. Wang, “Energy concentration enhancement using window width optimization in S transform,” in *2010 IEEE International Conference on Acoustics, Speech and Signal Processing*, March 2010, pp. 4106–4109.

- [129] E. Guvenkaya, A. Sahin, E. Bala, R. Yang, and H. Arslan, "A windowing technique for optimal time-frequency concentration and ACI rejection in OFDM-based systems," *IEEE Transactions on Communications*, vol. 63, no. 12, pp. 4977–4989, Dec 2015.
- [130] R. M. Roark and M. A. Escabi, "B-spline design of maximally flat and prolate spheroidal-type FIR filters," *IEEE Transactions on Signal Processing*, vol. 47, no. 3, pp. 701–716, March 1999.
- [131] M. Radad, A. Gholami, and H. R. Siahkoohi, "S-transform with maximum energy concentration: Application to non-stationary seismic deconvolution," *Journal of Applied Geophysics*, vol. 118, pp. 155 – 166, 2015.
- [132] T. Przebinda, V. DeBrunner, and M. Ozaydin, "Using a new uncertainty measure to determine optimal bases for signal representations," in *IEEE International Conference on Acoustics, Speech, and Signal Processing*, Phoenix, AZ, USA, Mar 1999, pp. 1365–1368.
- [133] K. Ghuman and V. DeBrunner, "A proof of Hirschman uncertainty invariance to the order of Rényi entropy for picket fence signals, and its relevance in a simplistic recognition experiment," in *IEEE International Conference on Acoustics, Speech and Signal Processing*, Brisbane, QLD, Australia, April 2015, April, pp. 4005–4009.
- [134] V. DeBrunner, M. Ozaydin, and T. Przebinda, "Resolution in time-frequency," *IEEE Transactions on Signal Processing*, vol. 47, no. 3, pp. 783–788, March 1999.
- [135] S. A. Hosseini, N. Amjady, and M. H. Velayati, "A Fourier based wavelet approach using Heisenberg's uncertainty principle and Shannon's entropy criterion to monitor power system small signal oscillations," *IEEE Transactions on Power Systems*, vol. 30, no. 6, pp. 3314–3326, Nov 2015.
- [136] M. Tsitsvero, S. Barbarossa, and P. D. Lorenzo, "Signals on graphs: Uncertainty principle and sampling," *IEEE Transactions on Signal Processing*, vol. 64, no. 18, pp. 4845–4860, Sept 2016.
- [137] E. Schrodinger, "About Heisenberg uncertainty relation," *Bulg. J. Phys.*, vol. 19, no. quant-ph/9903100, pp. 296–303, 1930.
- [138] D. Gabor, "Theory of communication. part 1: The analysis of information," *Journal of the Institution of Electrical Engineers - Part III: Radio and Communication Engineering*, vol. 93, no. 26, pp. 429–441, November 1946.

- [139] —, “Theory of communication. part 2: The analysis of hearing,” *Journal of the Institution of Electrical Engineers - Part III: Radio and Communication Engineering*, vol. 93, no. 26, pp. 442–445, November 1946.
- [140] R. Parhizkar, Y. Barbotin, and M. Vetterli, “Sequences with minimal time-frequency spreads,” in *2013 IEEE International Conference on Acoustics, Speech and Signal Processing*, May 2013, pp. 5343–5347.
- [141] —, “Sequences with minimal time-frequency uncertainty,” *Applied and Computational Harmonic Analysis*, vol. 38, no. 3, pp. 452 – 468, 2015.
- [142] N. Kovvali, W. Lin, and L. Carin, “Pseudospectral method based on prolate spheroidal wave functions for frequency-domain electromagnetic simulations,” *IEEE Transactions on Antennas and Propagation*, vol. 53, no. 12, pp. 3990–4000, Dec 2005.
- [143] A. Osipov, V. Rokhlin, and H. Xiao, *Prolate spheroidal wave functions of order zero*. Springer, 2013, vol. 187.
- [144] I. C. Moore and M. Cada, “Prolate spheroidal wave functions, an introduction to the Slepian series and its properties,” *Applied and Computational Harmonic Analysis*, vol. 16, no. 3, pp. 208 – 230, 2004.
- [145] F. A. Grunbaum and L. Miranian, “Magic of the prolate spheroidal functions in various setups,” in *Wavelets: Applications in Signal and Image Processing IX, (International Society for Optics and Photonics)*, San Diego, CA, United States, Dec 2001, vol. 4478, pp. 151–163.
- [146] J. Hogan and J. Lakey, *Duration and Bandwidth Limiting: Prolate Functions, Sampling, and Applications*, *Applied and Numerical Harmonic Analysis Series*, Birkhäuser. Springer, New York, London, 2013.
- [147] Z. Khalid and R. A. Kennedy, “Maximal multiplicative spatial-spectral concentration on the sphere: Optimal basis,” in *IEEE International Conference on Acoustics, Speech and Signal Processing*, Brisbane, QLD, Australia, April 2015, April, pp. 4160–4164.
- [148] M. A. Davenport and M. B. Wakin, “Compressive sensing of analog signals using discrete prolate spheroidal sequences,” *Applied and Computational Harmonic Analysis*, vol. 33, no. 3, pp. 438 – 472, 2012.

- [149] Z. Zhu and M. B. Wakin, "Wall clutter mitigation and target detection using discrete prolate spheroidal sequences," in *3rd International Workshop on Compressed Sensing Theory and its Applications to Radar, Sonar and Remote Sensing (CoSeRa)*, Pisa, Italy, June 2015, June, pp. 41–45.
- [150] K. Q. Lepage and S. Ching, "On the output of nonlinear systems excited by discrete prolate spheroidal sequences," *IEEE Transactions on Automatic Control*, vol. 62, no. 11, pp. 5780–5787, Nov 2017.
- [151] F. A. Grünbaum, "Eigenvectors of a Toeplitz matrix: Discrete version of the prolate spheroidal wave functions," *SIAM Journal on Algebraic Discrete Methods*, vol. 2, no. 2, pp. 136–141, 1981.
- [152] S. Karnik, Z. Zhu, M. B. Wakin, J. Romberg, and M. A. Davenport, "The fast Slepian transform," *Applied and Computational Harmonic Analysis*, 2017.
- [153] Z. Zhu, S. Karnik, M. A. Davenport, J. Romberg, and M. B. Wakin, "The eigenvalue distribution of discrete periodic time-frequency limiting operators," *IEEE Signal Processing Letters*, vol. 25, no. 1, pp. 95–99, Jan 2018.
- [154] S. Boyd and L. Vandenberghe, *Convex optimization*. Cambridge university press, 2004.
- [155] U. Grenander and G. Szegö, *Toeplitz forms and their applications*. Univ of California Press, 2001, vol. 321.
- [156] J. Zhong and Y. Huang, "Time-frequency representation based on an adaptive short-time Fourier transform," *IEEE Transactions on Signal Processing*, vol. 58, no. 10, pp. 5118–5128, Oct 2010.
- [157] J. L. Tan and A. Z. bin Sha'ameri, "Adaptive optimal kernel smooth-windowed Wigner-Ville bispectrum for digital communication signals," *Signal Processing*, vol. 91, no. 4, pp. 931–937, 2011.
- [158] Y. Abdoush, G. Pojani, and G. E. Corazza, "Adaptive instantaneous frequency estimation of multicomponent signals based on linear time-frequency transforms," *IEEE Transactions on Signal Processing*, vol. 67, no. 12, pp. 3100–3112, June 2019.
- [159] E. Sejdic, I. Djurovic, and J. Jiang, "A window width optimized S-transform," *EURASIP Journal on Advances in Signal Processing*, vol. 2008, p. 59, 2008.

- [160] T. Diehl, N. Deichmann, E. Kissling, and S. Husen, "Automatic S-wave picker for local earthquake tomography," *Bulletin of the Seismological Society of America*, vol. 99, no. 3, pp. 1906–1920, Jun 2009.
- [161] Z. E. Ross, M.-A. Meier, E. Hauksson, and T. H. Heaton, "Generalized seismic phase detection with deep learning," *arXiv preprint arXiv:1805.01075*, 2018.
- [162] N. Liu, J. Gao, X. Jiang, Z. Zhang, and Q. Wang, "Seismic time–frequency analysis via STFT-based concentration of frequency and time," *IEEE Geoscience and Remote Sensing Letters*, vol. 14, no. 1, pp. 127–131, Jan 2017.
- [163] S. M. Mousavi, C. A. Langston, and S. P. Horton, "Automatic microseismic denoising and onset detection using the synchrosqueezed continuous wavelet transform," *Geophysics*, vol. 81, no. 4, pp. V341–V355, Jun 2016.
- [164] S. Gabarda and G. Cristóbal, "Detection of events in seismic time series by time–frequency methods," *IET Signal Processing*, vol. 4, no. 4, pp. 413–420, Aug 2010.
- [165] R. Kumar, P. Sumathi, and A. Kumar, "Analysis of frequency shifting in seismic signals using Gabor-Wigner transform," *Earthquake Engineering and Engineering Vibration*, vol. 14, no. 4, pp. 715–724, Dec 2015.
- [166] B. Wang, "An amplitude preserving S-transform for seismic data attenuation compensation," *IEEE Signal Processing Letters*, vol. 23, no. 9, pp. 1155–1159, Sept 2016.
- [167] B. Wang and W. Lu, "An efficient amplitude-preserving generalized S transform and its application in seismic data attenuation compensation," *IEEE Transactions on Geoscience and Remote Sensing*, vol. 56, no. 2, pp. 859–866, Feb 2018.
- [168] P. Mcfadden, J. Cook, and L. Forster, "Decomposition of gear vibration signals by the generalised S-transform," *Mechanical Systems and Signal Processing*, vol. 13, no. 5, pp. 691 – 707, Sep 1999.
- [169] S. Kodituwakku, R. A. Kennedy, and T. D. Abhayapala, "Kaiser window based kernel for time-frequency distributions," *Electronics Letters*, vol. 45, no. 4, pp. 235–236, Feb 2009.
- [170] E. Sejdic, I. Djurovic, and J. Jiang, "S-transform with frequency dependent Kaiser window," *IEEE International Conference on Acoustics, Speech and Signal Processing - ICASSP '07*, vol. 3, pp. 1165–1168, April 2007.
- [171] http://ds.iris.edu/wilber3/find_stations/462899.

- [172] X. Song, "Anisotropy of the earth's inner core," *Reviews of Geophysics*, vol. 35, no. 3, pp. 297–313, Aug 1997.
- [173] D. Pham and S. Meignen, "High-order synchrosqueezing transform for multicomponent signals analysis-with an application to gravitational-wave signal," *IEEE Transactions on Signal Processing*, vol. 65, no. 12, pp. 3168–3178, June 2017.
- [174] D. M. Gruenbacher and D. R. Hummels, "A simple algorithm for generating discrete prolate spheroidal sequences," *IEEE Transactions on Signal Processing*, vol. 42, no. 11, pp. 3276–3278, Nov 1994.



List of Publications

Journal publications

1. **N. Singh** and P. M. Pradhan, "Efficient discrete S-transform based on optimally concentrated window," *IEEE Signal Processing Letters*, vol. 26, no. 1, pp. 14-18, Jan 2019
2. **N. Singh** and P. M. Pradhan, "Sharp detection of event's onset in seismic signals with asymmetrical Kaiser window-based S-transform," *IEEE Geoscience and Remote Sensing Letters*, vol. 16, no. 10, pp. 1620-1624, Oct. 2019.
3. **N. Singh** and P. M. Pradhan, "Achievable simultaneous time and frequency domain energy concentration for finite length sequences," *IET Signal Processing*, vol. 13, no. 8, pp. 736-746, Oct. 2019.
4. **N. Singh** and P. M. Pradhan, "S-transform based on optimally concentrated time-limited and band-limited windows," *Journal of pseudo-differential operators and applications*, Accepted (In Press), Aug. 2019.
5. **N. Singh** and P. M. Pradhan, "Frequency shift detection in structures during earthquake based on reassigned product-ST," *IEEE Geoscience and Remote Sensing Letters* (Revision R2 Under Preparation)

Conference publications

1. **N. Singh** and P. M. Pradhan, "Improvement of energy concentration in S-transform using maximally concentrated window," in *14th IEEE India Council International Conference (INDICON), Roorkee*, pp. 1-6, Dec. 15-17, 2017
2. **N. Singh** and P. M. Pradhan, "A novel scaling criterion for optimal trade-off between time and frequency resolution in S-transform," in *International Conference on Signal Processing and Communications (SPCOM), Bangalore*, pp. 1-6, July 16-19, 2018
3. **N. Singh** and P. M. Pradhan, "Simultaneously concentrated PSWF based synchrosqueezing S-transform and its application to R peak detection in ECG signal," in *28th IEEE International Conference on Robot & Human Interactive Communication (IEEE RO-MAN), New Delhi*, Oct. 14-18, 2019.